



UNIVERSITÀ DI NAPOLI FEDERICO II
Dottorato di Ricerca in Ingegneria Industriale
34° Ciclo

Experiments and Simulations of Hybrid Rocket Engines Burning Paraffin Fuels



Coordinatore:
Prof. Michele Grassi
Tutor:
Prof. Raffaele Savino

Candidato:
Ing. Giuseppe Gallo

**UNIVERSITÀ DEGLI STUDI DI NAPOLI
FEDERICO II**



Dottorato di Ricerca in Ingegneria Industriale
XXXIV Ciclo

**Experiments and Simulations
of Hybrid Rocket Engines
Burning Paraffin Fuels**

Coordinatore:
Prof. Michele Grassi

Tutor:
Prof. Raffaele Savino

Candidato:
Ing. Giuseppe Gallo

TABLE OF CONTENTS

Table of Contents.....	I
List of Figures.....	IV
List of Tables.....	VII
Abstract.....	VIII
CHAPTER 1. Hybrid Rocket Propulsion: state of the art	11
1.1 Introduction to hybrid rocket engines.....	11
1.1.1 Advantages of hybrid rockets	12
1.1.2 Historical perspective and potential applications of hybrid rocket propulsion technology.....	14
1.2 Hybrid rocket combustion mechanism	17
1.2.1 The model of Marxman and Gilbert	18
1.2.2 Combustion of liquefying fuels.....	19
1.3 CFD modelling of hybrid rocket internal ballistics	21
1.4 Combustion instability.....	24
1.5 History and original contributions of the present dissertation.....	26
CHAPTER 2. Experimental setup and firing test cases.....	28
2.1 Experimental facility.....	28
2.1.1 The lab-scale motors	28
2.1.2 Feeding line.....	29
2.1.3 Signal measurements and data acquisition system	31
2.2 Firing data reduction technique	31
2.3 Experimental firing test	33

2.3.1	Experimental results 1kN campaign	34
2.3.2	Ballistic reconstruction	38
2.3.3	Combustion instability campaign.....	42
CHAPTER 3. Modelling of hybrid rockets internal ballistics.....		47
3.1	Introduction to the definition of the numerical model for hybrid rockets simulation.....	47
3.2	Physical and numerical models for gaseous flowfield simulation.....	48
3.2.1	Turbulence model	49
3.2.2	Combustion model	51
3.2.3	Thermodynamic and transport properties	53
3.3	Computational domain and boundary conditions	54
3.4	Gas/fuel surface interface modelling	56
3.4.1	The old GSI and entrainment model	56
3.4.2	The new GSI	59
3.4.3	The new entrainment law	66
3.4.4	Boundary Conditions at the Fuel Surface and Solution Strategy..	69
3.5	Port diameter update with time for the transient simulation of the fuel grain consumption.....	72
CHAPTER 4. Numerical results of hybrid rockets internal ballistics simulation		75
4.1	New GSI/old entrainment model	75
4.1.1	Effect of Oxygen Mass Flux	76
4.1.2	Computational Grid Sensitivity and Validation.....	84
4.2	New GSI/New entrainment model.....	88
4.2.1	Experimental tests for new model assessment.....	88
4.2.2	Numerical Model Validation	90
4.2.3	Comparison with the old model.....	95

4.2.4	Effect of the Engine Size	97
4.2.5	Models Uncertainty Discussion	101
CHAPTER 5. Numerical model for combustion instability and results		103
5.1	Longitudinal modes in variable cross section ducts and density	103
5.1.1	Simplification of the double duct	107
5.1.2	Analytical mode results	108
5.2	A comprehensive one-dimensional model for acoustic stability analysis	112
5.2.1	The mean flow	116
5.2.2	Acoustic field equations	118
5.2.3	Mean flow results	120
5.2.4	Stability results	122
Conclusions		125
Appendix A: Simplified solution of the liquid layer equations		127
Appendix B: Zero Dimensional Acoustic Model		131
Acknowledgments		134
Bibliography		136

LIST OF FIGURES

Figure 1.1. Schematic of classical hybrid rocket engine.	11
Figure 1.2 Vacuum Isp and O/F ratio for various concentrations of aluminum mixed with paraffin burning with N ₂ O ₄ [8].....	14
Figure 1.3. Boundary layer combustion mechanism for hybrid rockets.....	18
Figure 1.4. Liquid layer instability and droplet entrainment mechanism (Ref. [28]).	21
Figure 2.1. 200 N-class hybrid rocket engine schematic.....	28
Figure 2.2. Test feeding lines schematic.....	30
Figure 2.3. Tescom ER3000 pressure controller scheme.	30
Figure 2.4. Rocket plume during firing (a) and propellant grain after the test (b) for test 2L.	35
Figure 2.5. Average regression rate versus oxidizer mass flux obtained with both small- and large-scale engines.	35
Figure 2.6. A representation of the development of the oxygen jet core in the case of conical axial injector.....	37
Figure 2.7. Correlation of experimental data using Eq.(2.10).	38
Figure 2.8. Characteristic velocity, exit velocity and exit pressure for different OF at the operating pressure of 13 bar.....	40
Figure 2.9 A graphical representation of the functions g, f, f' [76].	41
Figure 2.10. Experimental results test S-P.....	44
Figure 2.11 Experimental results Test S-H.....	45
Figure 2.12 Experimental results Test L-P.	46
Figure 3.1 An example of the computational grid for the 200 N-class engine.....	55
Figure 3.2 Schematic of the typical fuel consumption mechanism and heat transfer across liquefying fuels.	57
Figure 3.3 Liquid paraffin thermophysical properties as a function of temperature.	64
Figure 3.4 a) Maximum liquid-layer thickness, heat flux and surface temperature vs. regression rate, b) heat flux, surface temperature and mass fraction vs. liquid layer thickness.....	65

Figure 3.5. Schematic representation of the i -th node displacement components..... 74

Figure 4.1 Comparison between the results obtained considering constant or variable surface temperature: a) regression rate, b) surface temperature and wall heat flux. . 77

Figure 4.2 Total temperature contours plot with overlapped streamlines (top half) and mixture-fraction isolines (bottom half)..... 79

Figure 4.3 Detail of the flowfield at the motor head end (Test 4). 80

Figure 4.4 Total temperature radial profiles in the grain inlet, middle and outlet section. 81

Figure 4.5 Axial distribution of fuel surface parameters: a) regression rate components, b) vaporization-to-total regression rate ratio and surface temperature. 83

Figure 4.6 Space-average regression rate error. 84

Figure 4.7 Numerical error versus grid size. 85

Figure 4.8 Average regression rates and surface temperature vs. oxygen mass flux. 87

Figure 4.9 Average regression rate estimated with Eq. (4.3). 88

Figure 4.10 Operating pressure and thrust vs time. 90

Figure 4.11 Comparison of the time-averaged regression rate profile obtained by both the models with the experimental data. 91

Figure 4.12 A comparison between the computed spatially averaged regression rate (black line) and the experimental one rebuilt by the complete (black dot) and the simplified (white dot) reconstruction technique. 94

Figure 4.13 Comparison between the reconstructed regression rate by assuming constant and a linear variation of η_{cth}^* 95

Figure 4.11 A representation of the results of the new (black line) and old (grey line) gas/surface model coupled with the corresponding entrainment model..... 97

Figure 4.14 A representation of the grain consumption profile during the burning time. 98

Figure 4.15 Comparison of the wall heat flux and the cross section-averaged temperature profile along the motor axis of the tests 2S (black line) and 2L (grey line) at the initial time-step. 98

Figure 4.16 Temperature contour plot with overlapped streamlines (top half) and mixture fraction iso-lines (bottom half) of the test 2S and 2L at the initial and final time-step.....	100
Figure 4.17 A representation of the regression rate as function of the oxidizer mass flux computed at each time-step in tests S and a comparison of the obtained trendline (black line) with that derived experimentally in Ref. [73] (grey line).....	100
Figure 4.18 A representation of the regression rate as function of the oxidizer mass flux computed at each time-step in tests L.	101
Figure 5.1 Schematic of the 100N and 1kN motors.	103
Figure 5.2 Cross sectional jumps with variations of the gas properties [99].....	104
Figure 5.3 Double duct problem schematic.	108
Figure 5.4 Coupling parameter vs prechamber mixture ratio.	108
Figure 5.5 Spatial pressure fluctuations along the axial coordinate.	110
Figure 5.6 First mode vs. R1.....	111
Figure 5.7 First mode vs. mixture ratio.	112
Figure 5.8 Flow schematic and control volume.....	113
Figure 5.9 Sketch of a control volume inside the grain port.....	115
Figure 5.10 Mean flow results along axial coordinate.....	122
Figure 5.11 Stability results vs adimensionalized mass flow rate delay (Test S-P black line, test L-P grey line).	123
Figure 5.12 1L 100N chamber mode stability results.....	124
Figure 5.13 Grain length parametric study.	124

LIST OF TABLES

Table 2.1 Operating conditions of the 1000-N class engine.....	35
Table 2.2. Expected regression rate and deviations with respect experimental data.	36
Table 2.3 Firing test operating conditions.	42
Table 2.4 Experimental frequencies.	46
Table 3.1 Values of SST model constants [81].	51
Table 3.2 Computational domain dimensions.	55
Table 3.3. Paraffin wax properties.....	64
Table 4.1 Average operating parameters measured in the firing tests.....	75
Table 4.2. Average surface parameters calculated with variable and constant surface temperature models.....	78
Table 4.3. Grid sensitivity analysis results (Test 4).....	85
Table 4.4 Computed regression rate deviations from experimental data.	86
Table 4.5 Experimental data of firing test cases with paraffin-based fuel grains performed with the 200 N-class hybrid rocket.	89
Table 4.6 Time-space-averaged regression rate computed by both the models and the experimental value with the corresponding deviations.....	92
Table 5.1 Gas properties 100N and 1kN motor.	109
Table 5.2 Experimental vs numerical frequencies.....	109
Table 5.3 Acoustic frequencies of the feed pipe, 100N and 1kN motors.	110

ABSTRACT

In the last decade a significant and ever growing interest has been addressed towards hybrid rocket propulsion, which offers the best-of-both-worlds by leveraging the favourable aspect of both traditional solid and liquid systems. Among the numerous advantages which characterize hybrid rockets, the most attractive ones are the re-ignition and throttling capabilities combined with the possibility of embedding environmentally sustainable propellants and, of the utmost importance, their intrinsic safety and lower operational costs. Moreover, hybrid rockets yield a better specific impulse than solid propellant rockets and a higher density impulse than liquids, which make them a promising technology in a number of space missions.

The widely recognized potentialities of the hybrid rocket warrant the renewed research efforts that are being devoted to its development, but the state-of-the-art of this technology still presents a number of challenging issues to be solved.

A first fundamental task is the definition of suitable models for the prediction of the motor internal ballistics and performance. In particular, rocket performance is governed by the rate at which the fuel is gasified, i.e. by the fuel regression rate, as this latter determines the total mass flow rate and the overall oxidizer-to-fuel mixture ratio, which, for a given chamber pressure, control the motor thrust and the ideal specific impulse. For a given fuel, regression rate is basically limited by the heat flux input to the solid grain, which mainly depends on the thermo-fluid-dynamics in the combustion chamber. This latter is significantly influenced by several geometrical parameters, such as, for example, the oxidizer injection configuration or the grain port shape. Furthermore, the recent efforts aimed at overcoming the main drawback of the hybrid rockets, which is the low regression rate of conventional polymeric fuels, have been focused on the development of new paraffin-based fuels, characterized by a consumption mechanism presenting additional complex phenomena compared to that of conventional polymers. Their intrinsic characteristic is the onset of a thin liquid layer on the fuel grain surface, which may become unstable, leading to the lift-off and entrainment of fuel liquid droplets into the main gas stream, increasing the fuel mass

transfer rate. This phenomenon is strongly susceptible to the fuel composition, its manufacturing process and the obtained thermo-mechanical properties as well as to the engine operating conditions, which makes the prediction of the regression rate and combustion chamber internal ballistics even harder than in the case of a pure polymer. In this framework, computational fluid dynamics of hybrid rocket internal ballistics is becoming a key tool for reducing the engine operation uncertainties and development cost, but its application still presents numerous challenges due to the complexity of modelling the phenomena involved in the fuel consumption mechanism and the interaction with the reacting flowfield. A research effort is therefore of major importance in order to cover the lacking aspects and obtain quantitatively accurate results.

In addition, the hybrid combustion process tends to produce somewhat rougher pressure versus time characteristics than either liquid or solid rocket engines. However, a well-designed hybrid will typically limit combustion roughness to approximately 2 to 3% of mean chamber pressure. In any combustion device, pressure fluctuations will tend to organize themselves around the natural acoustic frequencies of the combustion chamber or oxidizer feed system. While significant combustion pressure oscillations at chamber natural-mode acoustic frequencies have been observed in numerous hybrid motor tests, such oscillations have not proved to be an insurmountable design problem. When pressure oscillations have occurred in hybrid motors, they have been observed to grow to a limiting amplitude. Unbounded growth of pressure oscillations, such as may occur in solid and liquid rocket motors, has not been observed in hybrid motors. Hybrid motors burning classic fuels have exhibited two basic types of instabilities in static test environments: acoustic and non-acoustic instabilities. Additional triggering mechanisms can arise when involving liquefying fuels. The large amount of fuel entrained in the chamber introduces an additional time-lag required to “vaporize” the liquid droplets. This delay can excite acoustic modes and start the characteristic feed-back loop occurring during combustion instability. Despite recent advances in understanding causes and solutions for combustion instability in hybrid motors, development of a comprehensive, predictive theory of

combustion stability remains one of the major challenges in hybrid technology development.

Therefore, the first main objective of the present work is the definition of proper computational thermo-fluid-dynamic models of the hybrid rocket internal ballistics, including a dedicated gas/surface interface treatment based on local mass, energy and mean mixture fraction balances as well as proper turbulence boundary conditions, which can properly model the physical fuel consumption mechanism. For the validation of the computational models, a number of experimental test cases obtained from static firing of laboratory scale rockets, have been performed at the Aerospace Propulsion Laboratory of University of Naples “Federico II” and successively numerically reconstructed. The comparison between the numerical results and the corresponding experimental data allowed validating the adopted model.

Then, a comparative experimental study on combustion instability for liquefying fuels is presented. The campaign is aimed to a better understanding of triggering mechanisms. An analytical model for the evaluation of the acoustic modes in a system with different cross sectional area and gas properties is described to investigate the exhibited experimental frequencies. Then, a suitable one-dimensional acoustic model for reacting flows with distributed mass flow rate addition in the chamber is presented for the prediction and the analysis of combustion instability.

CHAPTER 1. HYBRID ROCKET PROPULSION: STATE OF THE ART

1.1 Introduction to hybrid rocket engines

Hybrid rockets are chemical propulsion engines whose concept has been known since the early 20th century [1], in which fuel and oxidizer are separated in different physical states. In the classical system configuration (see Figure 1.1), hybrid rockets usually accommodate a prechamber ahead of the fuel grain, and an aft-mixing chamber, downstream of it; fuel is stored in the combustion chamber in the solid state, and a liquid or gaseous oxidizer is injected into one or multiple ports obtained in the solid fuel grain. The latter is usually made by simple classical polymers, such as high density polyethylene (HDPE), hydroxyl-terminated polybutadiene (HTPB), and polymethylmethacrylate (PMMA), polymers with metal additives to improve the density impulse, or, more recently, paraffin waxes.

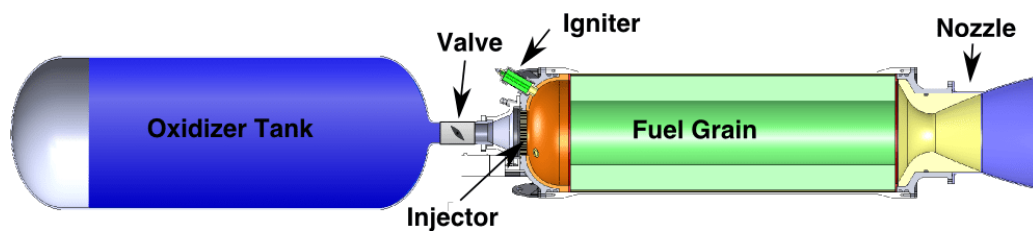


Figure 1.1. Schematic of classical hybrid rocket engine.

When the two propellants are ignited, a diffusive flame is formed in the boundary layer developing in the grain port, relatively far from the fuel surface, and it is fed, from the outer side, by the oxidizer, which is transported from the free stream by turbulent diffusion mechanisms, and, from the inner side, by the products of fuel pyrolysis that is sustained by the flame itself; the combusted mixture then expands through an exhaust nozzle generating the required thrust.

Performance of these engines is governed by the rate at which the fuel is gasified, i.e. by the fuel regression rate \dot{r} , as this latter determines the total mass flow rate and overall oxidizer-to-fuel mixture ratio OF , which, for a given chamber pressure, control the motor thrust and the ideal specific impulse I_{sp} .

1.1.1 Advantages of hybrid rockets

In the last decade a significant and ever growing interest has been addressed towards hybrid rocket propulsion thanks to its numerous advantages [2] compared to traditional solid and liquid systems.

1.1.1.1 Safety

The primary reason for interest in hybrid is the non-explosive nature of the design, which lead to safety in both operation and manufacture [3, 4]. In fact, in liquid bipropellant rockets, a pump leak or tank rupture can bring the oxidizer and the fuel together in an uncontrolled way resulting in a large explosion, while, in solid propellant rockets, the fuel and oxidizer are already mixed and held together in a polymer binder, so that cracks or imperfections can cause uncontrolled combustion and explosion. In hybrid propellant rockets the fuel and oxidizer are intimately separated and the design is less susceptible to chemical explosion. The fuel can be fabricated at any conventional commercial site, realizing a large cost saving.

1.1.1.2 Re-ignition and throttling capability

One of the critical issues of solid fuel rockets is the impossibility of shut down and re-ignition, i.e. once the engine is ignited there is no possibility to control or to stop the ignition, until the fuel grain is completely burned. On the contrary hybrid rocket engines can be throttled by modulating the oxidizer flow rate, to optimize the trajectory during atmospheric launch and orbit injection, and thrust termination/restart is simply accomplished by turning off and on the oxidizer flow rate.

With respect to liquid bipropellant rockets, hybrid rockets require one rather than two liquid containment and delivery systems, reducing the complexity and improving the reliability of the system. Throttling control is simpler because it alleviates the

requirement to match the momenta of the dual propellant streams during the throttling operation.

1.1.1.3 Environmental sustainability

Oxidizers and fuels used in hybrid rocket engines produce usually less threat to health and environmental safety. For example Hydrazine and its derivatives, which are widely used as propellants in liquid rockets, are highly corrosive, toxic and carcinogens.

The products of combustion in hybrid rockets are environmentally benign compared with conventional solids that generally use perchlorate-based oxidizers. In fact, solid rocket combustion products contain acid-forming gases such as hydrogen chloride (HCl). In addition, there are concerns about the effects of low levels of environmental perchlorate.

1.1.1.4 Theoretical specific and density impulse

Hybrid rockets yield a higher specific impulse than solid propellant rockets. In fact, the theoretical specific impulse of a hybrid rocket is more appropriately compared to a bipropellant liquid than a solid. This is because the oxidizers are the same and the solid fuels are hydrocarbons with energy content similar to kerosene.

However, hybrid solid fuel density are typically 15-20% greater than the density of liquid kerosene, so hybrid rockets yields higher density impulse than liquids. Furthermore, the fact that the fuel is in the solid phase makes it very easy to add performance-modifying materials. For example, the addition of aluminium powder produces a substantial increase in fuel density, increases the theoretical I_{sp} and shifts the peak I_{sp} to lower values of the oxidizer-to-fuel ratio, as for instance shown in Figure 1.2.

In conclusion, the above discussed features make hybrid engines a promising technology in a number of space missions, opening to safer and more flexible space vehicle launching and manoeuvring [5, 6, 7].

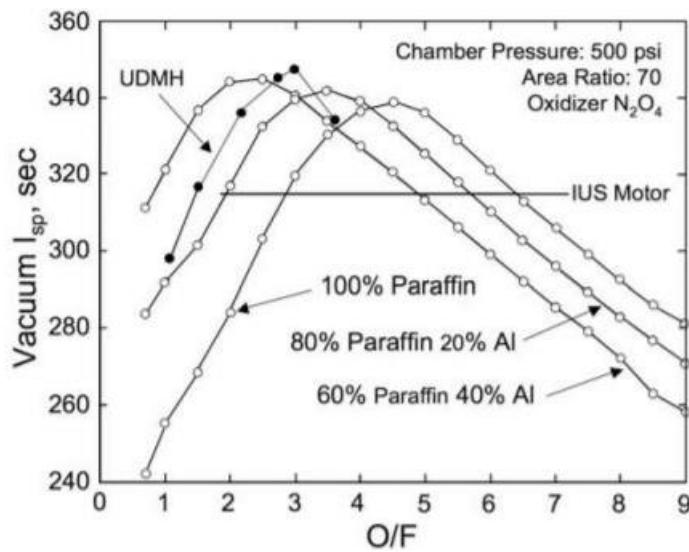


Figure 1.2 Vacuum Isp and O/F ratio for various concentrations of aluminum mixed with paraffin burning with N₂O₄ [8].

1.1.2 Historical perspective and potential applications of hybrid rocket propulsion technology

The hybrid rocket concept has been around for more than eighty years. The first liquid propellant rocket launched by the Soviet Union was actually a hybrid that used liquid oxygen (LOX) and gelled gasoline. The rocket was designed by Mikhail Tikhonravov in 1933 and built by a team from the Group for the Study of Reaction Motors (GRID) that was headed by the famous Sergei Korolev. The first flight reached an altitude of 1500 m using a 500 N class motor that burned for 15 s.

The earliest effort in the U.S. occurred at the Pacific Rocket Society and at General Electric, beginning in the late 1940s and continuing up to 1956. But early hybrid rocket development began in earnest when flight test programs were initiated both in Europe and in the U.S. in the 1960s. European programs in France and in Sweden involved small sounding rockets, whereas the American flight programs, largely sponsored by the U.S. Military Force, were target drones that required supersonic flight in the upper atmosphere for up to 5 minutes. Furthermore, in the late 1960s the small size hybrid rockets started to be scaled to large size motors by the Chemical Systems Division of United Technologies, which investigated motor designs that could produce the high

thrust required for space launch vehicles. Anyway, although several successful firings were performed during those years, it was recognized that the volumetric fuel loading efficiency was too low mainly because of the low regression rate.

Interest in the hybrid was revived again in the late 1970s, when concerns aroused about safety storage and handling of the large solid propellant segments of the Shuttle booster. Then, beginning in the late 1980s, two significant hybrid efforts occurred. One was the formation of the American Rocket Company (AMROC), an entrepreneurial industrial company entirely devoted to the development of large hybrid boosters based on LOX and HTPB. The second, with encouragement from NASA, was the formation of the Hybrid Propulsion Industry Action Group (HPIAG), composed of both system and propulsion companies devoted to exploring the possible use of hybrids for launch booster applications. Again, both efforts ran into technical stumbling blocks, caused by the low regression rate of HTPB fuel.

Several hybrid propulsion programs were initiated also in the late 1980s and in the 1990s. The most remarkable one was the Hybrid Propulsion Demonstration Program (HPDP), whose main objective was the design and fabrication of a 250000 lb thrust test bed.

The most successful flight of a hybrid rocket occurred in 2004 when the reusable manned spaceplane SpaceShipOne reached an altitude of 100 km for the second time in a 1-week period, using a four-port HTPB fuelled motor and nitrous oxide (N₂O) oxidizer.

Throughout this history, the fundamental issue of low regression rate inherent in polymeric fuels was the main drawback for the hybrid rocket development, but it was clear that if a significantly higher burning rate could be realized for the hybrid motor, the difficulties mentioned above could be greatly reduced and a smaller, more efficient motor could be designed. This deficiency was recognized early on, and many attempts were made to increase the regression rate.

In particular, the research activities carried out at Stanford University, beginning in 1997, led in the mid-2000s to the development of a class of liquefying fuels, including paraffin-based fuels, characterized by very high regression rate, ensuring good performance at low cost, availability, low environmental impact. These results

renewed the interest in hybrid rocket technology as a promising propulsive solution for important innovative missions.

Several market studies, starting from early 2000 allowed performing trade-off analyses for the identification of the most suitable space/aerospace application for hybrid rockets, with a particular interest in the framework of mass access to space. Four main markets can be identified for such technology, each one with different requirements in terms of performance and cost, which are listed in the following.

- *Sub-orbital flight vehicles* can be seen as the first enabling building block. In particular, large growth potential for *space tourism* as a business concept (Ref. [9, 10]) suggests the need for improvement in propulsion technologies, which would reduce the service price. Therefore, strategies for space propulsion cost reduction rely essentially on two approaches. The first approach is based on the use of lower cost and higher performance rocket engines, like hybrid rocket engines. The second approach involves the use of innovative high performance fuels, such as paraffin-based fuels. The interest of hybrid rocket applications in sub-orbital systems is increasing in both commercial and public funded projects. Commercial vehicles include Virgin Galactic SpaceShipTwo, Copenhagen Suborbitals Tycho Brahe and Whittinghill Aerospace mCLS: these are or will be powered by hybrid rocket motors [11].
- *Launch vehicles upper stages* could represent an effective market entrance of hybrid propulsion system, since this application is characterized by relatively low barrier and several potential advantages would derive from hybrid technology. An example of public effort in this direction involves the HYPROGEO EU-Funded project in the Horizon 2020 framework, related to the development of an hybrid rocket for launch vehicles upper stages, under the leadership of Airbus Defence and Space SAS.
- *Nano/microsatellite launch vehicles*. Considering the 2013 nano/ microsatellite launch services report [12], it is possible to assume that nano/microsatellites launch is a growing market. Furthermore, the historical analysis suggests that the current launch vehicle capacity will not be able to satisfy the future demand, in particular considering the increasing number of requests for

micro/nanosatellites. In order to exploit the increase in market demand, it will be of great importance to put in place specific strategies. In this scenario, hybrid launch vehicles for small payloads can be effectively developed using the knowledge established with sub-orbital applications. This is an important step in the direction of overcoming the historical perspective of nano/microsatellites as secondary payload only. The advantages of such dedicated launch systems are: low cost, flexibility, low environmental impact and orbit/time specificity.

- *Launch vehicles lower stages/boosters.* The application of hybrid rocket motors to launch vehicles lower stages and boosters is the most challenging scenario. Lower launch vehicles stages are characterized by very high thrust (magnitude order of several MN), required to reach escape velocity and lift-off of the launch vehicle. This extreme performance level requires a very large system. In such geometries, scale-up combustion phenomena can occur, which can significantly affect the engine behaviour. Low-scale to large-scale effects involve combustion stability, fuel grain mechanical resistance and non-homogeneous fuel consumption issues.

1.2 Hybrid rocket combustion mechanism

One of the fundamental problem in the design of a hybrid rocket is to accurately predict the fuel regression-rate, as a function of time and position along the surface of grain, since, as mentioned before, this is the main parameter governing the engine performance. Of course, this problem can be addressed only by a proper modelling of the hybrid rocket internal ballistics, which depend on different complex and interacting physical phenomena, on the engine configuration and on the fuel and oxidizer physical nature.

Many theories have been developed over the years in order to describe the hybrid combustion mechanism, but often they lack some important aspects or failed in the prediction of experimental results [13, 14, 15].

1.2.1 The model of Marxman and Gilbert

The most reliable hybrid combustion model for classical polymeric fuels was developed in 1963 by Marxman and Gilbert [16, 17] and it is still the starting point of design calculations and experimental comparisons. This model is based on the concept of diffusion flame, anticipated before, according to which the combustion reaction occurs in a thin region inside the developing boundary layer through diffusive mixing between vaporized oxidizer flowing through the port and fuel evaporating from the solid surface. Thus, the flame zone can be considered as temperature and mixture composition discontinuity (see Figure 1.3). Typically the chemical kinetics in the reaction zone are much faster than the relatively slow diffusion processes which provide the fuel and the oxidizer to the flame, thus the flame is said to be diffusion-limited.

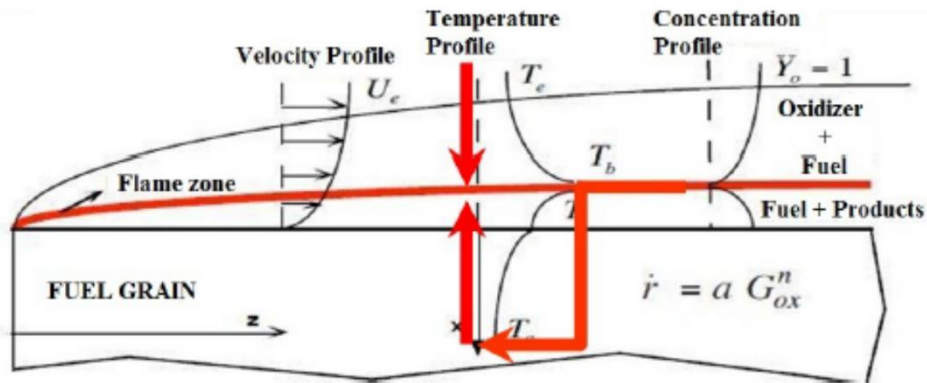


Figure 1.3. Boundary layer combustion mechanism for hybrid rockets.

According to this model, the fuel regression rate is proportional to the wall heat flux as

$$\rho_f \dot{r} = (\rho v)_w = \frac{\dot{q}_w}{h_v} \quad (1.1)$$

where ρ_f is the solid fuel density, $(\rho v)_w$ is the gaseous mass flux at the fuel wall, \dot{q}_w is the heat flux to the wall and h_v is the effective fuel vaporization heat, i.e. the energy per unit mass needed to evaporate fuel from the initial solid fuel temperature.

Considering the simpler configuration of a uniform oxidizer flow on a solid fuel slab, assuming unit Lewis and Prandtl numbers and applying the Reynolds analogy, the previous equation can be manipulated obtaining the following relationship between the fuel regression rate and the total axial mass flux G

$$\rho_f \dot{r} = 0.036 G Re_x^{-0.2} B^{0.23} \quad (1.2)$$

where $Re_x = Gx/\mu$ is the local Reynolds number and B is the so called blowing factor.

More generally, in order to overcome the slab fuel configuration hypothesis and the further complexity due to the total mass flux dependence on the regression rate itself, the regression rate law is simply expressed in the form

$$\dot{r} = aG_{ox}^n \quad (1.3)$$

where G_{ox} is the oxidizer mass flux in the fuel grain port and a and n are constant mainly depending on the propellants and on the system configuration and are usually determined experimentally. Eq. (1.3) represents the fact that, in marked contrast to solid rockets, the regression rate of a hybrid is insensitive to the chamber pressure, while, because of the diffusion-limited nature of the combustion process, it is primarily governed by turbulent mixing and heat transfer in the boundary layer, which in turn depend on the mass flux.

1.2.2 Combustion of liquefying fuels

As described in the previous section, fuel regression of classical polymers is determined by the ratio between the heat flux to the surface and the heat of phase change, thus it is limited by the heat and mass transfer mechanisms occurring from the flame to the fuel wall; blowing of fuel from the surface decreases the velocity gradient at the wall and the convective heat transfer for the so-called blocking effect [16]. Owing to this “counter-balance” between heat flux and blowing, hybrid rocket motors operating with polymeric fuels usually suffer from the problems associated with low regression rate, which hinder the widespread application of such propulsion systems.

Several strategies have been suggested to mitigate this shortcoming, such as, among the most common ones, the design of multi-port grains for which, despite the slow regression, a high thrust level can be obtained; the design of injection systems inducing recirculating [18, 19] or swirling oxidizer flows [20, 21]; and the addition of metal additives or solid particles, which mostly raise the density impulse with a minor effectiveness on the regression rate [22]. Yet, all of these methods lead to an increase of the system complexity and associated cost without producing major improvements of the engine overall performance [23].

Researchers at Stanford University [24] have demonstrated that a much more effective method for enhancing regression rate is to use propellants that form a melt layer at the combustion surface. These are usually non-polymerized substances that liquefy on heating. An obvious class includes liquids or gases at standard conditions, which are frozen to form solids (that is, solid cryogenic hybrids). However it is clear that the same internal ballistic behaviour can be experienced by materials that are solids at standard conditions if they form a melt layer at the combustion surface. Paraffin-based fuels belong to the latter class [25].

Compared to conventional polymers, the consumption mechanism of this class of fuels, known as liquefying fuels, is basically different and allows for significantly larger regression rate. Karabeyoglu et al. [24] have shown that these fuels display, indeed, regression rates up to 3-4 times higher than those achieved with traditional hybrid fuels. Referring to Figure 1.4, their intrinsic characteristic is the onset of a thin liquid layer on the fuel grain surface, which may become unstable. In fact, due to the low viscosity and surface tension, it is affected by a hydrodynamic instability of the Kelvin-Helmholtz type [26, 27] driven by the oxidizer flow injection, which leads to the lift-off and entrainment of fuel liquid droplets into the main gas stream, increasing the fuel mass transfer rate. This characteristic behaviour has been experimentally investigated showing the formation of roll waves and droplets in the tests carried out at atmospheric pressure, and filament-like structures along the fuel grain in the tests run at elevated pressures [28].

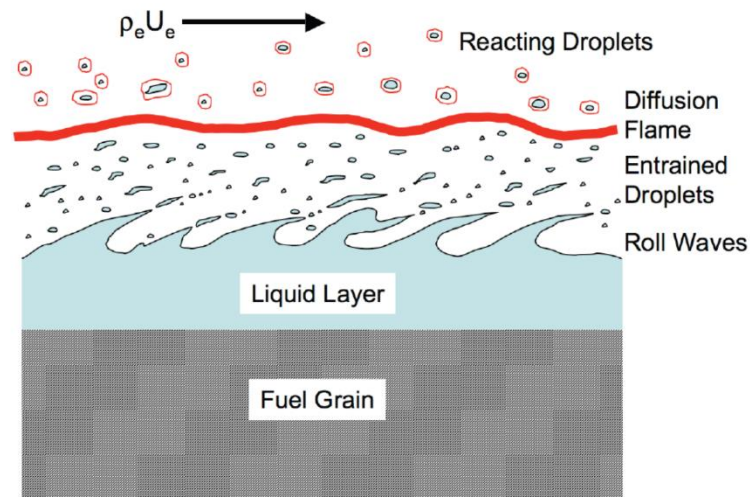


Figure 1.4. Liquid layer instability and droplet entrainment mechanism (Ref. [29]).

This mass transfer mechanism does not depend on heat transfer and raises the fuel mass flow without entailing the blocking effect determined by gaseous fuel blowing. As a result, the overall regression rate can be considered composed by two fractions, one determined by classical fuel vaporization, and the other by the liquid entrainment. The entrainment phenomenon is strongly susceptible to the fuel composition, its manufacturing process and the obtained thermo-mechanical properties as well as to the engine operating conditions [30], which makes the prediction of the combustion chamber internal ballistics even harder. Hence, on the one hand, designers need to characterize the fuel with extended experimental campaigns and, on the other, carry out rocket static firings to measure the achieved engine performance.

1.3 CFD modelling of hybrid rocket internal ballistics

Affordable and reliable computational models, capable to simulate the thermo-fluid-dynamic field in the rocket combustion chamber, are the subject of considerable interest recently, as they are aimed to become an efficient tool both in the system

design process and in the performance analysis stage for reducing the engine operation uncertainties and development cost.

In fact, the classical theories, starting from Marxman's work described in Section 1.2.1, elaborated to predict the regression rate of pyrolyzing fuels, are all based on the assumption of a turbulent boundary layer with chemical reactions occurring in the burning of a fuel slab in an oxidant gas flow and, therefore, are unable to reproduce the oxidizer injection effects, which may have a non-negligible impact even in standard motors [18]. The analytical models subsequently developed for liquefying fuels, such as the one in Ref. [24], are essentially modifications of the classical hybrid boundary-layer combustion theory for the entrainment mass transfer from the fuel grain, and consequently present the same limits as the original theory.

In this context, computational fluid dynamic (CFD) approaches to the solution of flowfield in the hybrid propellant rocket chamber have been considerably developed recently [31, 32, 33]; most of the effort has been addressed to classical non-liquefying fuels, which, however, involve numerous complexities due, for example, to the interactions among fluid dynamics, oxidizer atomization and vaporization, mixing and combustion in the gas phase [20], nozzle thermochemical erosion [34], particulate formation, and radiative characteristics of the flame [35].

A common strategy is solving the Reynolds Averaged Navier-Stokes (RANS) equations, with suitable turbulence closure and combustion models. In particular, justified by the fact that chemical and fluid dynamic characteristic times are much shorter than the regression rate time scale, steady-state solution of RANS equations is generally sought [36]. An acceptable method to study the hybrid rocket internal ballistics can be, therefore, simulating the flowfield at different times in the motor firing by considering the fuel port geometry evolution [37]. Nevertheless, a single numerical simulation is often performed on the chamber geometry drawn at the time-space averaged port diameter [37, 38]. To the authors' knowledge, in the competent literature, even when analyses have been performed at several stages of the motor firing, the grain inner diameter has been always considered uniform down the port; in other words, the axial non-uniformity of the regression rate has been usually neglected and the port diameter has been updated with a spatially-averaged regression rate value.

Moreover, the definition of a suitable and computational cost-effective strategy for liquefying fuels poses further complications related to the modeling of the melting layer dynamics and of the liquid entrainment phenomenon. In principle, to successfully simulate the paraffin-fuel consumption, two non-trivial tasks have to be accomplished, that are modeling, first, the melted fuel entrainment from the grain surface, and, second, the transformation of the melted fuel into gaseous species participating in the combustion process. These demanding efforts have probably discouraged researchers, so that usually drastic simplifications are introduced, such as giving the regression rate calculation away by assuming it from experiments [39, 40], or limiting the analysis to one-dimensional integro-differential models [41]. In other cases, observing that under the hybrid rocket chamber characteristic conditions the melted paraffin wax is in the supercritical state (thus surface tension vanishes and the sharp distinction at droplets surface between gas and liquid phases disappear), the melted layer brake up and subsequent liquid paraffin injection in the flowfield is disregarded, supposing that the entrainment is part of the turbulent mixing process [42]. However, in general, all the existing models are not successfully validated displaying still significant deviations from experimental data, which in some cases are around 25%. Hence, a research effort is definitely of major importance in order to obtain quantitatively accurate results.

A previous numerical model developed at the University of Naples was also devoted to the simulation of the internal ballistics of rockets burning liquefying fuels [43]. The numerical apparatus consisted of 3 tools aimed to: 1. rebuild the gaseous flow field by CFD simulations and the estimation of the wall heat flux at the grain surface; 2. estimate the entrained fraction; 3. couple the gaseous phase with the liquid and the solid ones by a suitable gas-surface interface (GSI) model.

The first GSI was just an adaptation of that designed for classical fuels [44]. The major weakness was the evaluation of the liquid-gas interface temperature, or “vaporization temperature”, which was assumed constant along the grain surface and determined with a fine tuning on experimental data. The model was dramatically sensitive to the set wall temperature for two reasons: it was imposed as temperature boundary condition at the grain wall in CFD simulations and it determined the enthalpy required for the paraffin phase change from liquid to vapour.

On the other hand, the first entrainment model referred to work shown in Ref. [24], which mainly related the entrained liquid mass flow rate to the total mass flux through an entrainment parameter. After performing a tuning procedure for the determination of the entrainment parameter, the model demonstrated a good capability to predict the time-space averaged regression rate in a range of oxidizer mass flux on a single motor configuration. Therefore, both the old entrainment model and interface model were, indeed, far to be considered part of a comprehensive design tool, because of their strong dependence on experimental tests.

Therefore, the first purpose of this thesis is to address the issues concerning the GSI and the entrainment correlation by developing a more sophisticated GSI, which univocally allows the computation of the interface temperature. Then, a more general correlation law was introduced, which took into account the key parameters in the evaluation of the fuel entrained fraction.

1.4 Combustion instability

When combustion occurs in a closed system, large pressure oscillations can be exhibited with a particular frequency, which mainly depends on the phenomena that promotes the feedback loop between the acoustic field and unsteady heat release [45]. Thermo-acoustic instabilities affect liquid, solid and hybrid rocket engines (HRE). The most notable example of combustion instability in liquid rocket engines occurred during the design of the F-1 engine for the Saturn V in the 1950's and 1960's, which was solved by a 17 month testing campaign consisting of 44 full-scale tests [46]. On the other hand, combustion instability dramatically increases thrust oscillations in solid rocket motors, because the mass flow rate is directly dependent on the chamber pressure, leading to unstable dynamic environments for the rest of the launcher up to the payload [47].

In this scenario, hybrid rocket motors usually yield a more stable operation. However, the strict requirements related to mission execution limit the allowable motor thrust oscillations. Most of the past studies are related to the employment of classic fuels as high-density polyethylene (HDPE) or hydroxyl-terminated

polybutadiene (HTPB). Combustion instability in hybrid rocket engines results from the coupling between hydrodynamics, acoustics and combustion, yielding to high amplitude pressure oscillations. The feedback path can involve several mechanisms, each one characterized by a specific time scale. In fact, the overall dynamic behavior of a hybrid rocket engine is the result of the dynamic of many processes: 1. the transition of the oxidizer from the tank to the injector; 2. the oxidizer evaporation in the case the oxidizer is stored in liquid phase; 3. mixing and combustion with fuel; 4. the thermal response in the solid grain; 5. the system gasdynamics. In the present study, the gas is injected in the gaseous phase and the feed-line is taken into account.

The coupling between the thermal response of the solid grain and combustion (TC coupling) can trigger a typical low-frequency instability characterized by pressure oscillations with frequencies in the range of tens Hertz and frequencies associated with the acoustic modes [48, 49]. An additional pathway driving low frequency combustion instability can occur, when liquid oxidizer is injected in the chamber. The instability can be aroused by the characteristic time, or delay, required to atomize and to vaporize the liquid droplets [50]. It is usually easy to model and control; the results of many studies present in literature suggest to increase the pressure drop at the injection plate in order to isolate the chamber from the feed line [51].

Combustion instability can be also triggered by vortices produced in the chamber near sudden area enlargement. When the shedding frequency approaches the acoustic one, a feedback loop between heat release and acoustic oscillations can be closed [52, 53, 54]. In particular, Carmicino performed a comparative study showing that radial injectors promote more combustion instability than the axial ones [55].

Many efforts have been spent in the last two decades in developing zero and one dimensional models to study the dynamics of pressure and velocity fluctuations [56, 57]. The first approach is usually involved, when the combustion chamber behaviour is simplified to a filling/emptying dynamics; the second is employed for the prediction of longitudinal acoustic modes of hybrid rocket combustion chambers, which, for instance, allows the prevention of the frequency matching with the vortex shedding [58, 59].

Although many studies have been performed with the regression rate of paraffin fuels, few efforts have been dedicated to the study of unstable motors. The reason is also due to the lack of experimental data available in literature, which makes hard the assessment of novel numerical models [60]. Paraffin fuels differ from classical fuels, because the grain consumption is far from a pure pyrolysis process. When a liquefying fuel is exposed to high temperatures, a low-viscosity unstable melt layer is formed on the burning surface; then, a small amount of fuel gasifies near the wall grain, while the largest part is entrained in the chamber in form of fuel liquid droplets and/or filament-like structures [61, 62, 63]. Differently from classical fuel, an additional time is required for the pyrolysis of fuel liquid droplets. In analogy with the case by which liquid oxidizer is injected in the chamber, this delay could increase the probability of working in unstable operating conditions. In the experimental tests presented in this work, combustion instability was experienced in tests employing gaseous oxidizer and paraffin fuels. The aim of the work is on the one hand to provide new experimental data to the scientific literature and, on the other hand, develop a numerical model able to predict combustion instability suggesting design requirements.

1.5 History and original contributions of the present dissertation

The need of a further development of the old numerical model was highlighted by an experimental campaign carried out on a 1kN motor at the Federico II propulsion laboratory [64]. The past numerical model was found to be inadequate in predicting the regression rate for this thrust class suggesting that the model assessment was restricted to a limited number of firing tests. Therefore, the main objective of the thesis is to address all the issues concerning the GSI and the entrainment correlation with the aim of removing numerical parameters tuned on experimental data.

In particular, the work proceeded by two steps. Firstly, the GSI was improved including a more detailed thermal analysis along the liquid melt layer developed on the fuel grain surface. A novel methodology for the calculation of the surface

temperature of liquefying fuels typically burned in hybrid rockets is proposed. This procedure stems from the formulation of a fuel in-depth pyrolysis model coupled with the resolution of the thermo-fluid-dynamic field in the rocket combustion chamber, which allows for the characterization of the unstable liquid layer formed on top of the fuel surface. The aim is the simulation of the internal ballistics of hybrid rocket engines fed by paraffin-based fuels without the need for parametrically assigning the surface temperature to match the experimental data as, indeed, required in the previous GSI model. With the presented technique, surface temperature and fuel vaporization rate are calculated locally along the wall. Secondly, the old entrainment model was replaced by a more general correlation law dependent on adimensional number. The new entrainment law is scalable and a full assessment of the overall numerical model was obtained on different motor thrust classes. This activity led to the following journal [65, 66] and conference papers [64, 67].

Furthermore, the phenomenon of combustion instability was encountered during the experimental activities. Three dedicated experimental tests have been performed to drive numerical activities and recognize possible triggering mechanisms. Two tests have been performed at the same operating condition but with different fuels (paraffin and HDPE). Only test burning paraffin fuel exhibited combustion instability. For this reason, the cause was addressed to a “vaporization” delay of the liquid fuel entrained into the combustion chamber. This assumption was supported by a suitable acoustic model able to predict combustion instability. The novelty concerns the exhibited phenomena and the adopted numerical method to study it. A paper has been recently submitted to an international journal.

CHAPTER 2. EXPERIMENTAL SETUP AND FIRING TEST CASES

2.1 Experimental facility

The experimental activities described in this work have been carried out at the Aerospace Propulsion Laboratory of University of Naples “Federico II”, located in the Military Airport “F. Baracca” of Grazzanise (CE, Italy).

The test rig is a versatile set up primarily designed for testing hybrid rocket engines of several sizes [68]. It is equipped with a test bench and a general-purpose acquisition system, which allow evaluating propellant performance and combustion stability [55], testing of sub-components and/or complete power systems, nozzles [69], air intakes, catalytic devices [70, 71], burners, ignition and cooling systems [72, 73].

2.1.1 The lab-scale motors

Several rocket demonstrators of different scales are available for testing at the Laboratory. The experimental firings that will be presented in this work have been performed with a 200 N-class hybrid rocket whose schematic is depicted in Figure 2.1.

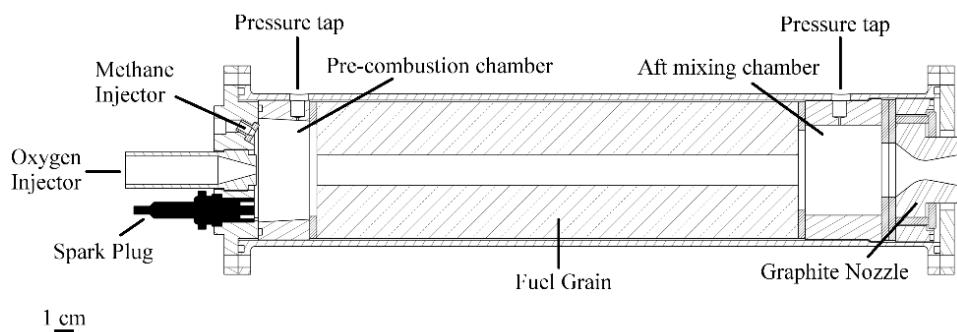


Figure 2.1. 200 N-class hybrid rocket engine schematic.

The lab rocket engine has an axisymmetric combustion chamber, with 350 mm length and 69 mm case inner diameter.

The motor forward closure can accommodate different injectors; the tests presented in the following sections have been performed with a converging nozzle injector, whose exit section diameter is 6 mm, which delivered oxygen in single-port cylindrical fuel grains.

Upstream and downstream of the solid grain a dump plenum and an aft-mixing chamber are set up. The pre-chamber, which is 25 mm long with a 50 mm inner diameter, shifts the broad oxidizer recirculation towards the fore end of the grain, in order to increase the overall regression rate. The post-chamber is usually required in hybrids to promote gas mixing at the exit of the fuel port, thereby improving combustion efficiency. Aft-mixing chamber with either 38 mm or 58 mm length can be employed with the aim of testing fuel grains of 220 mm length. The engine has two pressure taps for static pressure measurements in the pre- and in the post-chamber. A graphite converging-diverging exhaust nozzle is usually employed. The modular design of the engine allows the use of nozzles with different throat diameter and area ratio.

A spark plug powered by a Honeywell solid-state igniter spark generator is arranged in the pre-chamber where methane gas is injected for 3 seconds simultaneously with the oxygen to ignite the motor. This system ensures repeatable ignition conditions as well as motor re-ignition.

In addition to the firings performed with the subscale engine presented above, some firing tests have been performed on a larger scale, 1 kN-class hybrid rocket available at the lab. The engine design is conceptually similar to the design of the subscale engine. The injection system in this case is based on a showerhead architecture composed of seven holes, one concentric with the motor axis and the other 6 periodically distributed on a circumference.

2.1.2 Feeding line

A schematic of the oxidizer feeding line is depicted in Figure 2.2. Gaseous oxygen is supplied by a reservoir of 10 pressurized tanks connected to the motor feed line. The feeding pressure is then set by means of the TESCOM ER3000 electronically controlled pressure valve (see Figure 2.3), which regulates an electro-pneumatic valve

in order to reduce the pressure to the desired set point. The control is performed on the basis of the pressure signal measured by a transducer located downstream the regulator. The presence of a choked Venturi tube before the injector ensures that the set feeding pressure is directly proportional to the desired oxygen mass flow rate. The same device allows the evaluation of the latter parameter through gas temperature and pressure measurements upstream of the throat section.

An additional line is present for nitrogen purging into the chamber for the burn out and in case of an accident

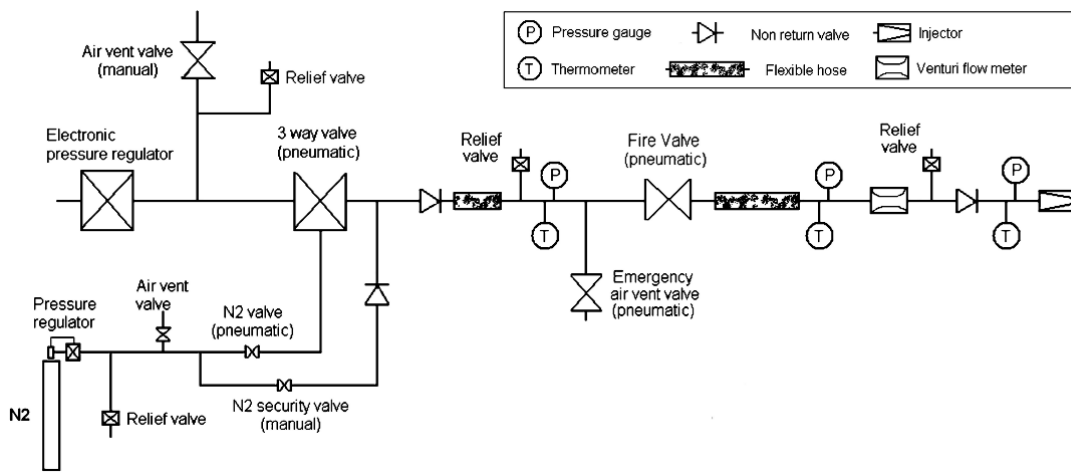


Figure 2.2. Test feeding lines schematic.

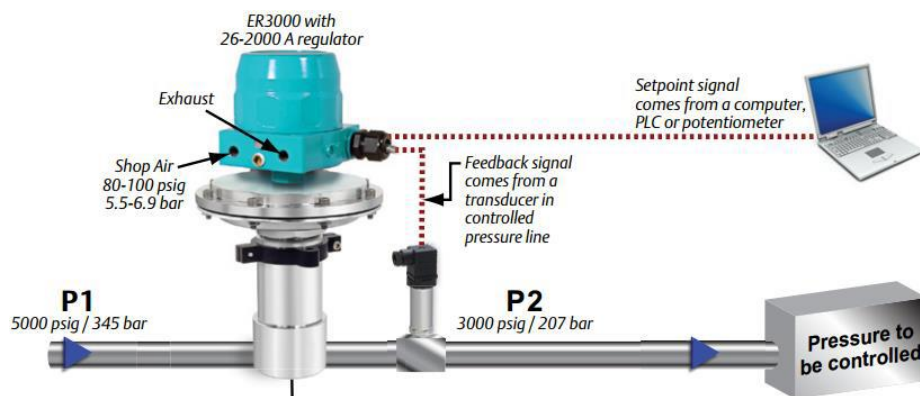


Figure 2.3. Tescom ER3000 pressure controller scheme.

2.1.3 Signal measurements and data acquisition system

Several sensors are present for the measurement of significant quantities during experimental test, which are listed in the following.

- Three capacitive pressure transducers and three thermocouples are located along the feeding line and at the section upstream of the oxidizer injector for the measurement (and monitoring for safety reasons) of the feeding pressure and of the temperature.
- As above mentioned, a choked Venturi tube is located upstream the oxidizer injector; a pressure transducer and a thermocouple allow the measurement of the pressure and the temperature upstream its throat section for the evaluation of the oxidizer mass flow rate.
- Two pressure transducers are assembled on proper pressure taps present on the rocket for the measurement of the pressure in the pre-chamber and in the aft-mixing chamber during engine operation.
- Four load cells assembled on the test bench allow evaluating the motor thrust by computing the sum of the loads measured with each cell.

The analogue signals generated by thermocouples, pressure transducers and load cells are sampled at 5 kHz, digitally converted, processed and recorded on the hard disk by a National Instruments (NI) PXI Express standard system interconnected with the computer by means of optic fiber connections. With this equipment and using a software developed in LabView, the motor is ignited and the firing test is completely automated. All the signals are stored in a binary format and, after downsampling the data to 100 Hz with a boxcar average, in text format for post-processing.

2.2 Firing data reduction technique

The main parameters directly measured in the firing tests are the oxidizer mass flow rate \dot{m}_{ox} , the chamber pressure p_c , the motor thrust Th , the fuel grain mass consumption ΔM and the burning time t_b . The remaining quantities of interest can be

derived from the measured ones. From the fuel grain mass loss and the operation time, the average fuel mass flow rate can be calculated as

$$\bar{\dot{m}}_f = \frac{\Delta M}{t_b} \quad (2.1)$$

and consequently the average oxidizer-to-fuel ratio can be evaluated as

$$\overline{O/F} = \frac{\overline{\dot{m}_{ox}}}{\bar{\dot{m}}_f} \quad (2.2)$$

Where $\overline{\dot{m}_{ox}}$ is the time averaged oxidizer mass flow rate, which is measured and controlled by the employment of a choked Venturi.

The space-averaged final port diameter can be calculated from the fuel mass loss as

$$\tilde{D}_2 = \sqrt{D_1^2 + \frac{4 \Delta M}{\pi \rho_f L}} \quad (2.3)$$

where D_1 and L are the grain initial diameter and length, respectively. The time-space-averaged port diameter can be then evaluated as

$$\bar{D} = \frac{D_1 + \tilde{D}_2}{2} \quad (2.4)$$

and the average oxidizer mass flux can be calculated as

$$\bar{G}_{ox} = \frac{4\overline{\dot{m}_{ox}}}{\pi \bar{D}^2} \quad (2.5)$$

The time-space-averaged fuel regression rate can be evaluated as

$$\bar{r} = \frac{\tilde{D}_2 - D_1}{2t_b} \quad (2.6)$$

The main factors of uncertainty involving the measured quantities are the determination of the burning duration (i.e. the time interval between the inflection point on the pressure rise branch at the motor start up and the one on the pressure drop at the burnout); the dispersion of the grain port initial diameter measurements, and, of course, on a lesser degree, the scale sensitivity for the measurement of the initial and final grain masses, and the signals oscillation during the test in the measurement of the oxidizer mass flow rate. For the details of the uncertainty assessment procedure refer to [22].

Besides the average quantities evaluated as described before, also the axial profiles of the fuel grain consumption and the corresponding time-averaged local regression rate profiles have been measured. In particular, experimental data are obtained by sectioning the fuel grain transversally in a number of slices, and measuring the port diameter by means of a caliper; in each transversal section, the minimum, maximum and the average of eight diameter measurements have been recorded. The corresponding local regression rate has been then obtained with Eq. (2.6).

2.3 Experimental firing test

In this section, the results of several firing tests carried out at the Aerospace Propulsion Laboratory described in the previous sections are presented. The purpose is the collection of significant experimental data representative of the regression behaviour at different operating conditions aimed of assessing the numerical models described in CHAPTER 3. In addition, further tests have been performed to investigate the exhibited combustion instability encountered during the experimental activities and drive the development of a suitable numerical model described in CHAPTER 5.

2.3.1 Experimental results 1kN campaign

Five tests on the 1000 N class engine were carried out using the same paraffin formulation of the previous campaign. All the performed firing tests were successful, no damage in any parts of the engine was observed. Figure 2.4a shows a picture of the exhaust plume during test 3L, and Figure 2.4b shows the propellant grain at the end of the same firing. A quite uniform consumption was observed.

The average measured quantities, for the different firing tests, are summarized in Table 2.1. The throttling test 5L showed a stable behavior, both thrust and pressure levels were steady for both the operating conditions and the transition appeared stable without oscillations. The experimental data points in terms of fuel regression rate as function of the oxidizer mass flux are reported in Figure 2.5 along with the data points measured on a previous campaign performed on a subscale 200-N class engine [74]. It is quite evident that, the regression rates obtained with the 1000 N engine, which are in the range of about 1.91 mm/s (Test 4L) and 3 mm/s (Test 2L), are significantly higher than the values obtained with the subscale rocket at equal oxidizer mass flux. The following correlation was obtained in the 200N motor:

$$\dot{r} = aG_{ox}^n \quad a = 0.071; \quad n = 0.795 \quad (2.7)$$

Applying Eq.(2.7) to the 1kN tests, the expected regression rate are affected by a non-negligible error compared to the experimental one. The relative errors are listed in Table 2.2.



(a) (b)
Figure 2.4. Rocket plume during firing (a) and propellant grain after the test (b) for test 2L.

Table 2.1 Operating conditions of the 1000-N class engine.

Parameter	Test 1L	Test 2L	Test 3L	Test 4L	Test 5L
Effective firing time (s)	7.5	9.0	11.4	5.6	9.7 (5.3+4.4)
Effective oxidizer mass-flow rate (kg/s)	0.195	0.243	0.192	0.110	0.142 – 0.215
Time-averaged fuel mass-flow rate (kg/s)	0.152	0.2039	0.172	0.984	0.177
Time-averaged mixture ratio (-)	1.29	1.20	1.11	1.12	-
Time-space-averaged ox mass-flux (kg/m ² s)	72.35	69.94	52.37	55.35	53.3
Time-space averaged fuel regression rate (mm/s)	2.53	2.99	2.49	1.91	2.6

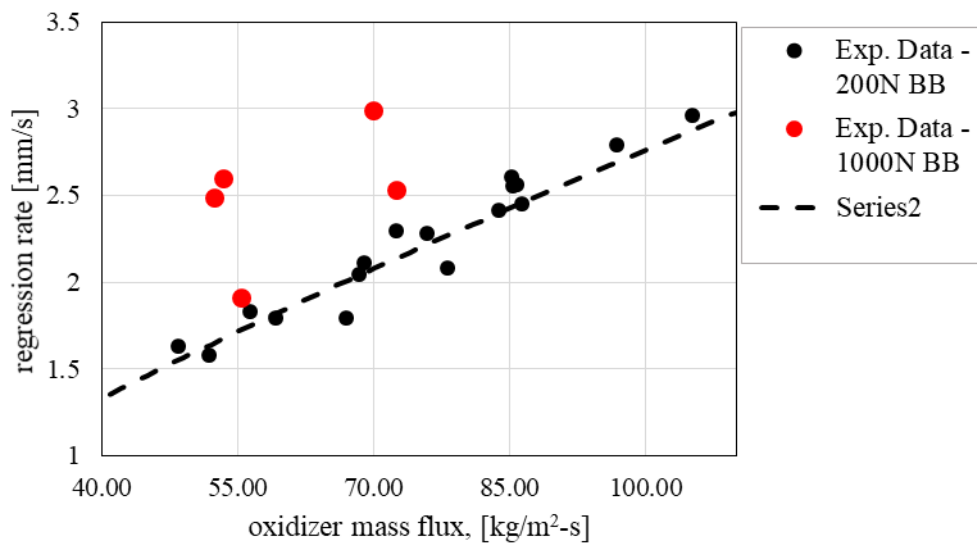


Figure 2.5. Average regression rate versus oxidizer mass flux obtained with both small- and large-scale engines.

Table 2.2. Expected regression rate and deviations with respect experimental data.

Parameter	Test 1L	Test 2L	Test 3L	Test 4L	Test 5L
Expected regression rate with Eq. (2.7), mm/s	2.14	1.67	1.65	1.73	2.08
Relative deviation w.r.t. experimental data, %	15.6%	38.0%	33.7%	9.6%	30.5%

The results suggest that the oxidizer mass flux is not the unique key quantity affecting the regression rate, but the regression rate could be affected by the size of the average port diameter. For axial injections, larger diameters host larger recirculating regions, which provide an augmentation of the wall heat flux [19].

The impact of this effect on the overall fuel regression rate depends also on the oxidizer injector arrangement (i.e. in the case of conical axial injector on the injector diameter D_{inj}) and the pre-chamber length L_{pre} . In particular, observing Figure 2.6 , the part of the grain touched by the recirculation region, i.e. the axial distance between the impingement point and the grain port inlet section, Δx , can be expressed as:

$$\Delta x = \frac{(\bar{D} - D_{inj})}{2 \tan \alpha} - L_{pre} \quad (2.8)$$

where \bar{D} is the average port diameter and α is the spreading angle, which for a free jet pattern can be realistically assumed to be equal to 8° independently from the mass flow rate [75].

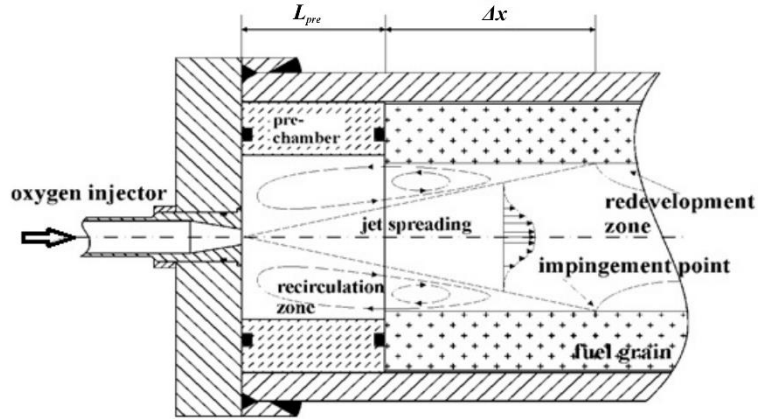


Figure 2.6. A representation of the development of the oxygen jet core in the case of conical axial injector.

Differently from past studies in which the regression rate was basically correlated to the grain diameter and the oxidizer mass flux [18], a new correlation for the average regression rate is found as function of the oxidizer mass flux and the aspect ratio, A_r , defined as:

$$A_r = \frac{\Delta x}{L} \quad (2.9)$$

The aspect ratio represents the percentage of grain interested by the presence of the recirculating zone. Therefore, assuming two tests performed at the same average oxidizer mass flux, the higher regression rate is exhibited by the test with the largest grain length exposed to the recirculating zone. The new correlation is given by:

$$\dot{r} = a G_{Ox}^n A_r^m \quad a = 0.277; \quad n = 0.593; \quad m = 0.317 \quad (2.10)$$

where the regression rate is expressed in mm/s and the mass flux in kg/m²s. Figure 2.7 shows the improvement of the new correlation law. Note that the oxidizer mass flux dependency exponent, n , is decreased from 0.795 in previous law to 0.593, while aspect ratio dependency exponent, m , is increased from 0 to 0.317 suggesting that the regression rate dependency on the aspect ratio cannot be neglected. Clearly, Eq. (2.10) is valid only for tests in which Δx is greater than 0 (i.e. tests featuring recirculating zone in the port). However, all tests shown in Figure 2.5 fall in this case, therefore Eq. (2.10) remains valid.

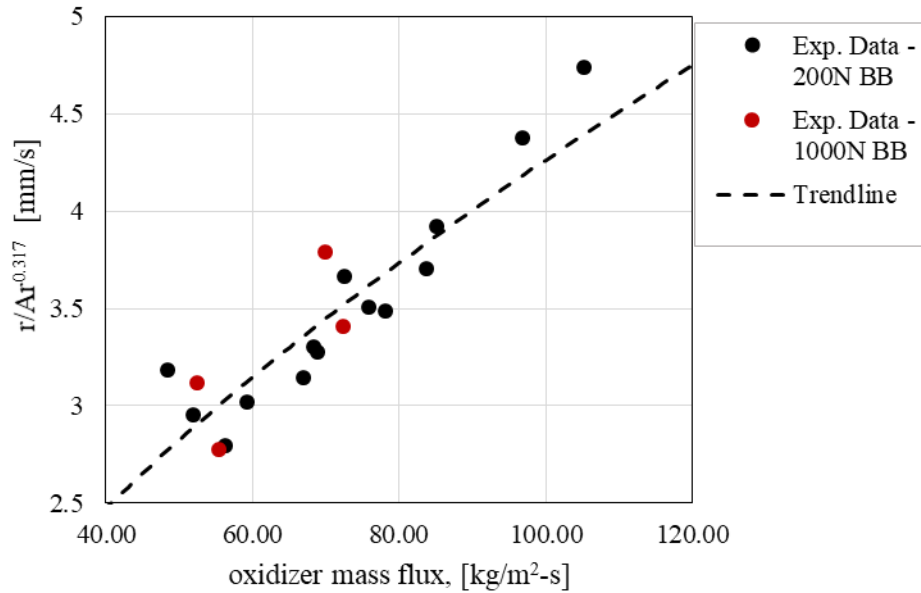


Figure 2.7. Correlation of experimental data using Eq.(2.10).

2.3.2 Ballistic reconstruction

Ballistic reconstruction techniques are helpful methods, which allow the temporal rebuilding of the regression rate during the burning time. The regression rate reconstruction of the experimental tests was performed to further validate the numerical model described in CHAPTER 3. The employed reconstruction method is taken from Ref. [19] and it is presented in brief in this section. Assuming quasi-steady operation, the motor thrust can be expressed as:

$$F = \dot{m}' v_e' c_d \lambda + (p_e - p_a) A_e \quad (2.11)$$

where \dot{m}' is the isentropic one-dimensional mass flow rate flowing through the nozzle computed at the chamber conditions, v_e' is the isentropic one-dimensional exit velocity, $\lambda \approx 0.997$ is the momentum-thrust factor [76], which takes into account the divergence of the rocket nozzle, c_d is the discharge coefficient which accounts for both non-one-dimensionality and non-isentropicity of the flow, p_a is the ambient pressure, p_e is the exit pressure and A_e is the nozzle exit area section.

Dividing both the sides of Eq. (2.11) by the chamber pressure and the throat area, one can obtain:

$$\frac{F}{p_c A_t} = \frac{v_e'}{c_{th}^*} \frac{c_d \lambda}{\eta} + \left(\frac{p_e}{p_c} - \frac{p_a}{p_c} \right) \frac{A_e}{A_t} \quad (2.12)$$

Whereby $\eta = \frac{c_{exp}^*}{c_{th}^*}$ is an efficiency coefficient which corrects the theoretical characteristic velocity to obtain the experimental one. The thrust and the pressure in Eq. (2.12) are known quantities from the experimental tests and they are function of the time, while the exit velocity, the exit pressure and the theoretical characteristic velocity are computed by the software CEA [77] considering at all times the experimental chamber pressure and the oxidizer to fuel ratio OF . This is calculated from the steady state expression of the mass balance equation:

$$c_{th}^* [(1 + OF)/OF] - \frac{p_c A_t}{\dot{m}_{ox} \eta} = 0 \quad (2.13)$$

Once computed the spatially averaged OF_i at the i -th timestep, the space-averaged regression rate and the updated grain diameter can be obtained as:

$$\dot{r}_i = \frac{\dot{m}_{ox_i}}{OF_i} \frac{1}{\rho_s \pi D_i L} \quad (2.14)$$

$$D_{i+1} = D_i + 2\dot{r}_i \Delta t \quad (2.15)$$

where the time-step considered is equal to the sample rate of 10 ms. An additional equation is needed for the computation of the discharge coefficient. This quantity is calculated imposing that the computed total fuel mass, $\Delta M'_f$, consumed during the burning time is equal to the experimental one, ΔM_f :

$$\Delta M'_f(c_d) - \Delta M_f = 0 \quad (2.16)$$

Figure 2.8 shows the typical behaviour of the characteristic velocity, exhaust velocity and exit pressure at a chamber pressure of 13 bar with a nozzle area ratio of 2.5. The curves have been obtained giving in input to CEA software the fuel paraffin with the chemical formula $C_{32}H_{66}$ at the temperature of 293 K with a formation enthalpy of -967.8 kJ/mol.

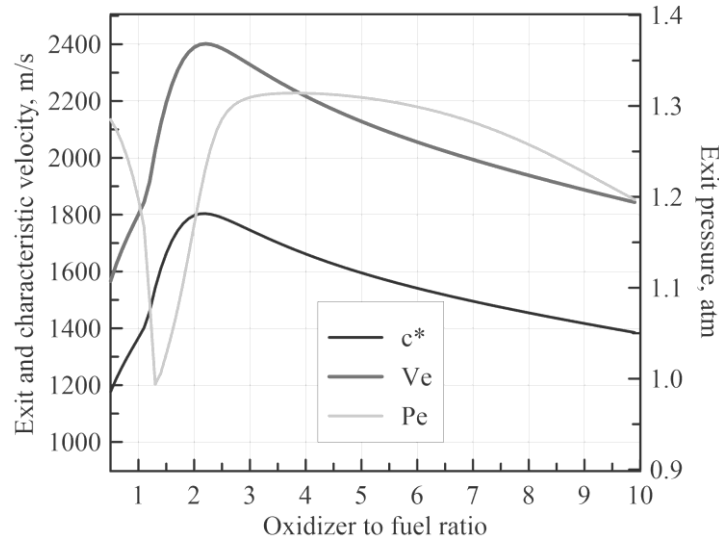


Figure 2.8. Characteristic velocity, exit velocity and exit pressure for different OF at the operating pressure of 13 bar.

The calculation procedure adopted is the following:

- 1) an arbitrary discharge coefficient is imposed;
- 2) η and OF are calculated by Eqs. (2.12) and (2.13), respectively, by an iterative process (since c_{th}^* is function of OF and evaluated by CEA);

- 3) the instantaneous regression rate is computed and the grain diameter is updated.

Points 2) and 3) are repeated each time-step until the extinguishment of the test. After, Eq. (2.16) is checked and if a suitable convergence criterion is not satisfied, the discharge coefficient is recomputed according to the bisection method.

It is worth to notice that the following procedure can fail in a specific range of OF, when the pressure trace changes during the burning time. Figure 2.9 represents the behavior of the quantity f , which is defined as $f = c_{th}^*[(1 + OF)/OF]$ and is only function of OF, and g , defined as $g(t) = \frac{p_c A_t}{\eta m_{ox}}$, which is only dependent on the chamber pressure (and therefore of burning time).

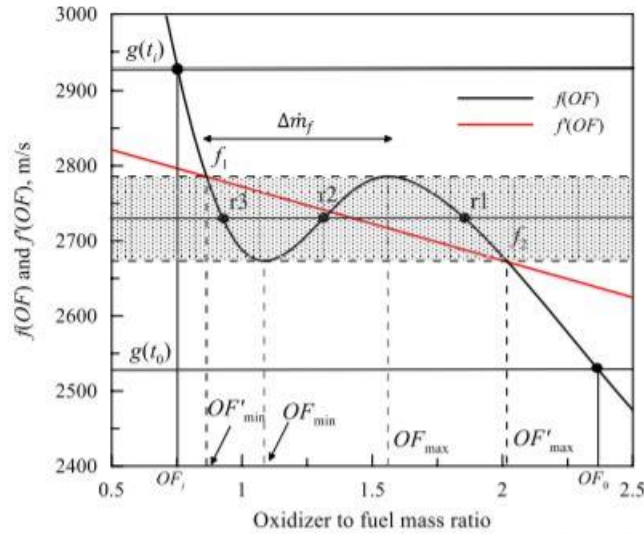


Figure 2.9 A graphical representation of the functions g, f, f' [78].

Since hybrid rockets are usually designed to operate around the point maximizing the specific impulse, the OF shift during the burning time falls in the range between OF'_{min} and OF'_{max} , which identify two limit values of f (f_1 and f_2 , respectively). These define upper and lower bounds of the dark box in the figure, where three solutions are possible with three different OF . This feature was already observed in Ref. [79, 80] and, actually, it might not be a problem. Although function f is not invertible in general in this OF range, it can be made invertible if it is segmented into three sub-functions with the domain limited to $[-\infty, OF_{min}]$, $[OF_{min}, OF_{max}]$ and $[OF_{max}, +\infty]$, respectively. If the $g(t)$ function falls into the black box and it is constant during the burning time, three roots are possible, which are the corresponding solution of the three sub-functions. The working sub-function is selected by the choice of initial condition, OF_0 . For instance, referring to Figure 2.9, an OF_0 included between $[-\infty, OF_{min}]$ will select the root r_3 . However, just one of the roots can satisfy Eq.(2.16), hence the overall procedure can quickly converge by correctly choosing the initial condition. The problem actually arises when the pressure trace (hence $g(t)$) increases during the burning time as in the tests L. In fact, assuming that $g(t_0)$ is lower than f_2 at the initial timestep t_0 , and it increases during the burning time, an unphysical jump of the mixture ratio must occur from OF_{max} (corresponding to the maximum value of f in the dark box) to OF'_{min} , skipping all the solutions included in this range [78]. In this case, function f needs to be relaxed with a monotone decreasing function in the mentioned

OF range as f' (see Figure 2.9). However, the procedure is simplified in this thesis work: Eq. (2.12) is removed, Eq. (2.13) is solved imposing ηc_{th}^* constant during the burning time, and iteratively changing its value until matching the calculated and measured mass losses as per Eq.(2.16). Therefore, $\Delta M'_f$ becomes function of the quantity ηc_{th}^* . When the convergence is obtained, ηc_{th}^* must coincide with the experimental characteristic velocity, c_{exp}^* . While the combustion efficiency η can be retained constant during the test, c_{th}^* can shift if the fuel mass flow rate increases during the burning time. Although in the next sections it will be shown that tests L are characterized by an increasing fuel mass flow rate, the error computed by the simplified procedure is estimated and considered acceptably low.

2.3.3 Combustion instability campaign

Three tests are presented in this section:

1. Test S-P is performed with the 100N motor class thrust burning GOX and paraffin.
2. Test S-H is performed with the 100N motor class thrust burning GOX and HDPE.
3. Test L-P is performed with the 1kN motor class thrust burning GOX and paraffin. Note that Test L-P coincides with test 2L.

S and L indicate the motor size (small and large), while P and H indicate the fuel kind (paraffin and HDPE). The operating conditions are resumed in Table 2.3. Note that test L-P coincides with test 2L of Table 2.1. However, for the sake of the reader, it is reported below, again.

Table 2.3 Firing test operating conditions.

Parameter	Test S-P	Test S-H	Test L-P
Fuel	Paraffin	HDPE	Paraffin
Time-averaged oxygen mass flow rate, g/s	25.0	25.0	243.0
Time burning, s	5.6	10.7	9
Time-space averaged regression rate, mm/s	2.44	0.476	2.96

Time-space averaged oxidizer mass flux, kg/m ² s	38.81	80.74	69.94
Time-averaged overall mixture ratio	1.6	13.04	1.20
Time-averaged chamber pressure, atm	8.5	3.8	20.9
Time-averaged feed pressure, atm	8.93	4.5	27.2
Initial port diameter, mm	15	15	40
Grain length, mm	70	70	350
Time-space-averaged port diameter, mm	28.75	20.09	66.51
Postburn space-averaged port diameter, mm	42.46	25.19	93.42
Feed-line tube length, mm	420.0	420.0	420.0
Feed-line tube diameter, mm	15.0	15.0	15.0
Prechamber length, mm	25.0	25.0	55.0
Prechamber inner diameter, mm	50.0	50.0	110.0
Postchamber length, mm	37.9	37.9	100.0
Postchamber inner diameter, mm	50.0	50.0	108.0
Nozzle throat diameter, mm	9.6	9.6	21.2

Figure 2.10 shows the chamber pressure signal and the corresponding spectrogram of test S-P. The motor is ignited at around 1s and the chamber pressure reaches the expected quasi steady-state value of 6 bar at 1.2s. Limit cycle is clearly reached at 2s with pressure oscillations included between 5 and 11 bar. The spectrogram of the chamber displays frequencies at 280 and 560 Hz. It is excluded that the exhibited frequencies are the first and second mode of the combustion chamber for two reasons: firstly, because the simplified formula for the estimation of the first and the second mode:

$$f_{nL} = \frac{n\bar{c}}{2L} \quad (2.17)$$

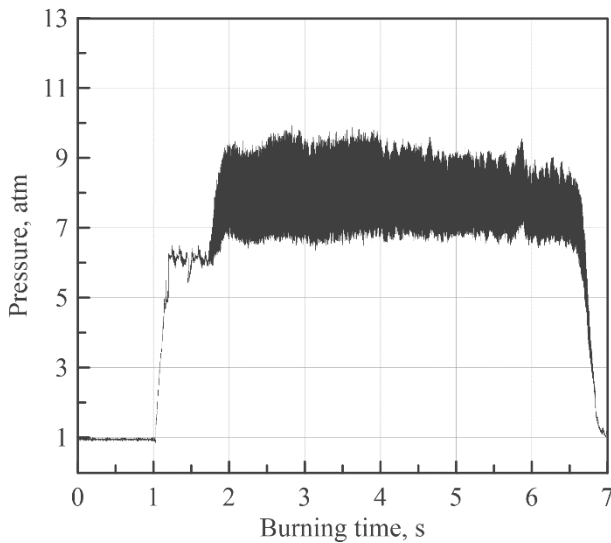
leads to a 1L and 2L frequency of 4515 Hz and 9029 Hz with a speed of sound of 1200m/s (corresponding to the experimental mixture ratio), respectively, which are far from that shown in Figure 2.10b; secondly, the frequencies do not evolve during the burning time, which is typical of the chamber acoustic frequencies because of the rapid

enlargement of the grain diameter as seen in [55]. In addition, the frequencies are also different from the Helmholtz mode given by:

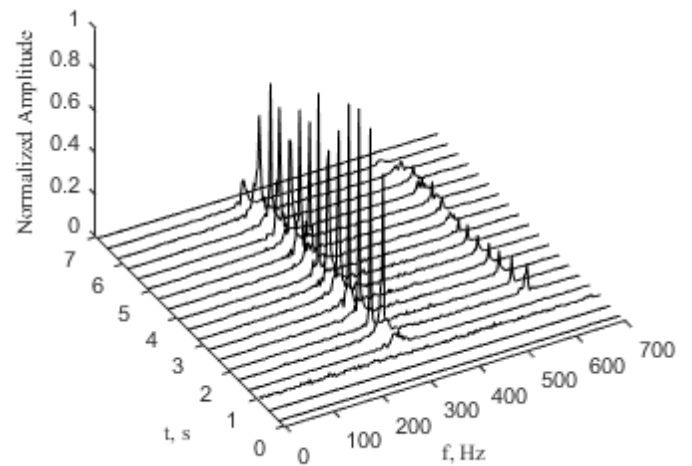
$$f_H = \frac{\bar{c}}{2\pi} \sqrt{\frac{\pi D_t^2}{4V(l + 0.8D_t)}} \quad (2.18)$$

where D_t is nozzle diameter, l is the nozzle length and V is the combustion port total volume, that is, the sum of the prechamber, fuel port, and aft chamber volumes.

These observations indicate that the feed pipe upstream the injector plays an important role in the acoustic system. Indeed, using Eq. (2.17) assuming the oxygen speed of sound at room temperature and L equal to the sum of the motor and feed pipe lengths, we obtain a 1L and 2L frequency of 298 Hz and 596 Hz similar to the experimental one. This is therefore not surprising, because the motor length is only 24% of the overall system. However, in the next section an analytical model to compute the acoustic frequencies in a series of ducts with different cross sectional area and density is presented.



(a) Chamber pressure



(b) Chamber pressure spectrogram

Figure 2.10. Experimental results test S-P.

Test S-H was performed burning HDPE by employing the same motor configuration and mass flow rate of Test S-P. Figure 2.11 shows a stable combustion and no pressure oscillations took place during the burning time. This suggests that the combustion instability exhibited in the previous test is related to the kind of fuel and

the characteristic mass transfer mechanism involved by liquefying fuels. Indeed, the pyrolysis of the liquid droplets entrained from the grain surface into the combustion zone could introduce a time-lag to the release of fuel mass flow rate, which could trigger combustion instability. On the other hand, for polymeric fuels the delay can be recognized negligible because the fuel immediately gasifies near the wall grain. Anyway, a dedicated 1D acoustic model is presented in section 5.2 to study the system stability for different mass flow rate delays, since the characteristic time of droplet pyrolysis is not known a priori.

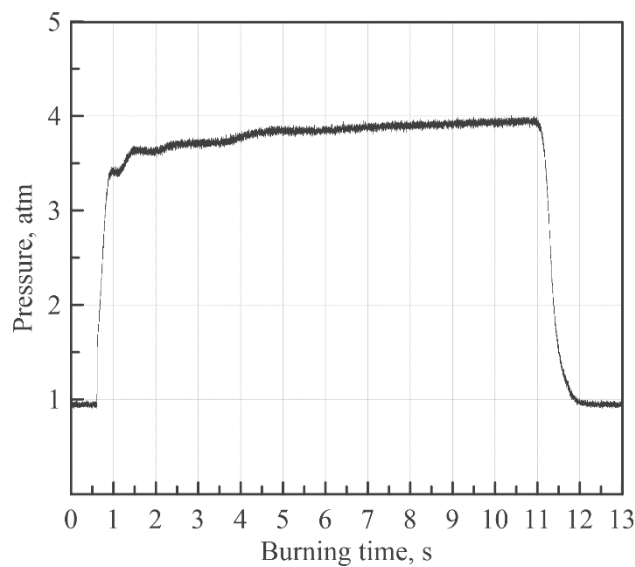


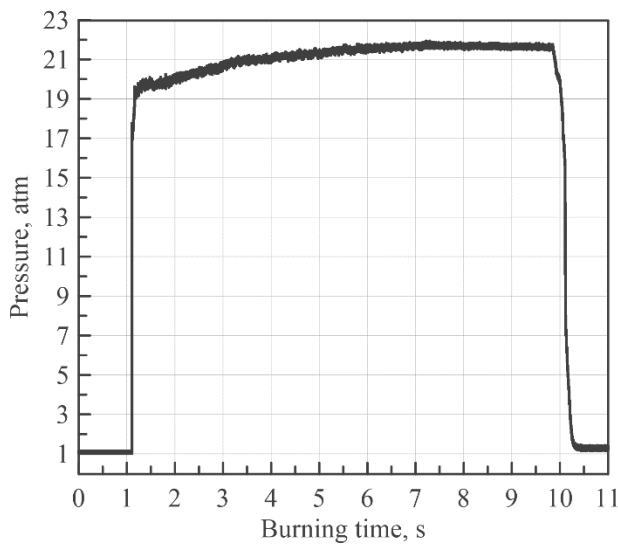
Figure 2.11 Experimental results Test S-H.

Finally, an additional test (Test L-P) was performed employing the 1kN motor. The experimental results are displayed in Figure 2.12. Although a stable combustion is displayed in the chamber pressure signal, many frequencies are shown in the corresponding spectrogram. In particular, a dirty signal with a peak around 755 Hz is identified at the beginning of the test and damped in the next seconds, while a peak similar to that shown in Figure 2.10 is detected at 1377 Hz. All the experimental frequencies are resumed in Table 2.4.

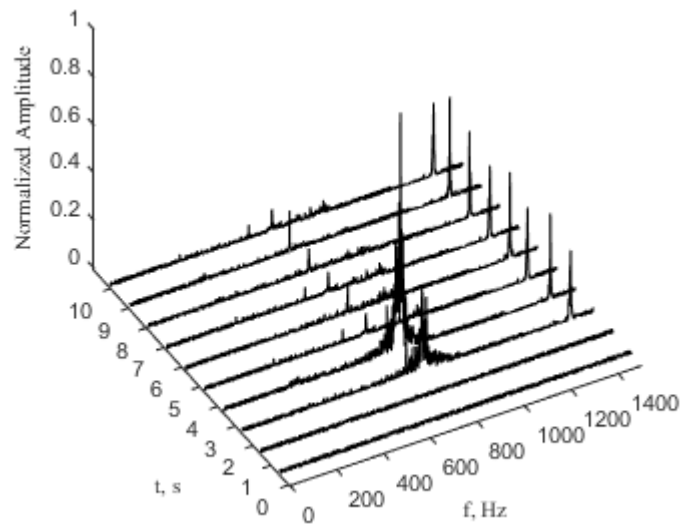
In summary, we can recap the principal experimental observations in the following points:

1. Frequencies shown in test S-P cannot be motor acoustic frequencies. The feed pipe has to be considered in the analysis.

2. The instability is exhibited only by test S-P burning paraffin-fuel suggesting that liquefying fuels introduce a delay in the motor dynamics. The delay is addressed to the time required liquid droplet pyrolysis.
3. The motor configuration of test L-P prevented the instability.



(a) Chamber pressure



(b) Chamber pressure spectrogram

Figure 2.12 Experimental results Test L-P.

Table 2.4 Experimental frequencies.

ID-test	Frequency, Hz	
Test S-P	280	560
Test L-P	755	1377

CHAPTER 3. MODELLING OF HYBRID ROCKETS INTERNAL BALLISTICS

3.1 Introduction to the definition of the numerical model for hybrid rockets simulation

As mentioned before, one of the fundamental goals of the present dissertation is the definition of a suitable numerical model for the simulation of the thermo-fluid dynamic flowfield in the combustion chamber and through the nozzle of hybrid rockets, which will be presented in this chapter.

As it will be described in detail in the following, the definition of such a model followed several steps with an increasing degree of sophistication and accuracy as well as of the predictive capabilities on the fluid dynamics and the fuel.

The first step consisted in identifying the equations governing the complex physical phenomena involved in hybrid rockets internal ballistics, including the proper turbulence closure for the RANS equations and a suitable chemical model for the combustion.

Then, a dedicated treatment for predicting the interaction between the gaseous flowfield and the solid grain surface has been defined and implemented in order to estimate the local fuel regression rate for a fixed condition in terms of oxidizer mass flow rate and grain geometry. This treatment is based on a system of equations based on local mass, energy and species balances and on physical considerations about the consumption mechanism involved depending on the class of fuel. An iterative strategy for the resolution of this system of equations has been adopted, since the solution itself is affected by the thermo-fluid dynamic conditions in the combustion chamber.

Finally, a specific procedure has been implemented for the transient simulation of the grain geometry evolution due to the fuel consumption during the engine operation, consisting in solving at each time-step the flowfield, calculating the regression rate distribution along the grain surface as described before, and then numerically integrate

the regression rate in time in order to calculate the grid nodes displacements. The fluid domain geometry is then modified, the computational mesh is adjusted to the new geometry and the numerical simulation at the new time-step is performed.

3.2 Physical and numerical models for gaseous flowfield simulation

Fuel grain material is here assumed to be composed 100% by paraffin wax with carbon number equal to 32 (i.e. with chemical formula: $C_{32}H_{66}$). The critical pressure of such a paraffin wax is 6.5 bar [81], thus, in the usual hybrid rocket chamber operating conditions the melted paraffin wax is in the supercritical pressure regime, for which surface tension disappears and the gas and liquid phases at the droplets surface tend to be undistinguishable; furthermore, viscosity and diffusivity are comparable to those typical of a gas, thereby the diffusion processes are significantly faster than in the liquid phase, which in a first approximation allows neglecting the two-phase flow effects. Accordingly, the RANS equations for a single-phase multicomponent turbulent reacting flow are solved in a two-dimensional axisymmetric domain by means of a finite volume technique and a pressure-based algorithm [82].

For the sake of reader's convenience, the set of equations solved is presented in the following. The Favre-averaged (i.e. density-weighted) equations of continuity and momentum can be expressed in Cartesian tensor form, with the understanding that repeated indices mean summation, as [83]:

$$\frac{\partial \bar{\rho}}{\partial t} + \frac{\partial}{\partial x_j} (\bar{\rho} \tilde{u}_j) = S_m \quad (3.1)$$

$$\frac{\partial}{\partial t} (\bar{\rho} \tilde{u}_i) + \frac{\partial}{\partial x_j} (\bar{\rho} \tilde{u}_i \tilde{u}_j) = - \frac{\partial \bar{p}}{\partial x_i} + \frac{\partial \bar{\tau}_{ij}}{\partial x_j} + \frac{\partial}{\partial x_j} (-\overline{\rho u'_i u'_j}) \quad (3.2)$$

where S_m is the mass source term eventually needed for representing the fuel mass addition.

Here the bar denotes conventional time averaging, while the tilde denotes density-weighted averaging; τ_{ij} is the stress tensor that is defined as

$$\tau_{ij} = \mu \left[\left(\frac{\partial u_i}{\partial x_j} + \frac{\partial u_j}{\partial x_i} \right) - \frac{2}{3} \delta_{ij} \frac{\partial u_k}{\partial x_k} \right] \quad (3.3)$$

where δ_{ij} is the Kronecker delta. Symbols with prime indicate the corresponding quantity fluctuation. The term $\mathcal{R}_{ij} = -\overline{\rho u_i' u_j'}$, originating from the averaging operation, is known as the Reynolds stress tensor, and it needs to be modeled.

3.2.1 Turbulence model

The Shear Stress Transport (SST) turbulence model [84] has been employed for its improved capability of predicting flows with separated regions. This latter is a combination of the robust and accurate k - ω model, developed by Wilcox [85], in the near-wall region, with the standard k - ε model implemented away from the wall using a blending function. With the SST model the transport equations of the turbulence kinetic energy, k , and the specific dissipation rate, ω , are formulated as

$$\frac{\partial}{\partial t} (\bar{\rho} k) + \frac{\partial}{\partial x_i} (\bar{\rho} \tilde{u}_i k) = \frac{\partial}{\partial x_j} \left[(\mu + \mu_t \sigma_k) \frac{\partial k}{\partial x_j} \right] + \mathcal{R}_{ij} \frac{\partial \tilde{u}_i}{\partial x_j} - \beta^* \bar{\rho} \omega k \quad (3.4)$$

$$\begin{aligned} \frac{\partial}{\partial t} (\bar{\rho} \omega) + \frac{\partial}{\partial x_i} (\bar{\rho} \tilde{u}_i \omega) &= \frac{\partial}{\partial x_j} \left[(\mu + \mu_t \sigma_\omega) \frac{\partial \omega}{\partial x_j} \right] + \bar{\rho} \frac{\alpha}{\mu_t} \mathcal{R}_{ij} \frac{\partial \tilde{u}_i}{\partial x_j} - \beta \bar{\rho} \omega^2 + \\ &2(1 - F_1) \bar{\rho} \sigma_{\omega_2} \frac{1}{\omega} \frac{\partial k}{\partial x_j} \frac{\partial \omega}{\partial x_j} \end{aligned} \quad (3.5)$$

in which the Reynolds stress is modelled using the Boussinesq approximation

$$\mathcal{R}_{ij} = \mu_t \left[\left(\frac{\partial \tilde{u}_i}{\partial x_j} + \frac{\partial \tilde{u}_j}{\partial x_i} \right) - \frac{2}{3} \delta_{ij} \frac{\partial \tilde{u}_l}{\partial x_l} \right] - \frac{2}{3} \bar{\rho} k \delta_{ij} \quad (3.6)$$

The turbulent viscosity, μ_t , is expressed as follows

$$\mu_t = \frac{\bar{\rho}k}{\omega} \frac{1}{\max\left(1; \frac{\Omega F_2}{0.31\omega}\right)} \quad (3.7)$$

where the function F_2 is defined, depending on the distance from the wall y , as

$$F_2 = \tanh(\Phi_2^2) \quad (3.8)$$

with

$$\Phi_2 = \max\left(\frac{2\sqrt{k}}{0.09\omega y}; \frac{500\mu}{\bar{\rho}\omega y^2}\right) \quad (3.9)$$

The coefficient α is given by

$$\alpha = \gamma \frac{1/9 + Re_t/2.95}{1 + Re_t/2.95} \quad (3.10)$$

where $Re_t = \bar{\rho}k/\mu\omega$ is the turbulent Reynolds number.

The blending function F_1 takes the value of 1 on the wall and tends to zero at the boundary layer edge, being defined as

$$F_1 = \tanh(\Phi_1^4) \quad (3.11)$$

With

$$\Phi_1 = \min\left[\max\left(\frac{\sqrt{k}}{0.09\omega y}; \frac{500\mu}{\bar{\rho}\omega y^2}\right); \frac{4\bar{\rho}\sigma_{\omega_2}k}{CD_{k\omega}y^2}\right] \quad (3.12)$$

where $CD_{k\omega}$ is the positive part of the last term in Eq. (3.5) (cross-diffusion term):

$$CD_{k\omega} = \max \left(2\bar{\rho}\sigma_{\omega_2} \frac{1}{\omega} \frac{\partial k}{\partial x_j} \frac{\partial \omega}{\partial x_j}; 10^{-20} \right) \quad (3.13)$$

The model coefficients σ_k , σ_ω , β , γ are defined by blending the corresponding coefficients of the original k - ω model, denoted with the subscript 1, with those of the transformed k - ε model that are denoted with the subscript 2, as

$$\begin{bmatrix} \sigma_k \\ \sigma_\omega \\ \beta \\ \gamma \end{bmatrix} = F_1 \begin{bmatrix} \sigma_{k_1} \\ \sigma_{\omega_1} \\ \beta_1 \\ \gamma_1 \end{bmatrix} + (1 - F_1) \begin{bmatrix} \sigma_{k_2} \\ \sigma_{\omega_2} \\ \beta_2 \\ \gamma_2 \end{bmatrix} \quad (3.14)$$

All the model constants are listed in Table 3.1.

Table 3.1 Values of SST model constants [83].

Constant	Value	Constant	Value
σ_{k_1}	0.850	σ_{k_2}	1.00
σ_{ω_1}	0.500	σ_{ω_2}	0.856
β_1	0.075	β_2	0.0828
γ_1	0.553	γ_2	0.440
β^*	0.090		

3.2.2 Combustion model

Assuming that the chemical kinetics is fast compared to the diffusion processes occurring in the motor for the typical mass fluxes and chamber pressures considered here [86], the non-premixed combustion of oxygen and gaseous fuel injected from the grain wall is modelled by means of the Probability Density Function (PDF) approach coupled to chemical equilibrium [87]. Accordingly, combustion is simplified to a mixing problem (mixed is burnt), and the difficulties associated with closing non-linear reaction rates are avoided. In fact, under the hypothesis of equal diffusivities for all chemical species and assuming that the Lewis number is equal to 1, the species equations can be reduced to a single equation for the transport of the mixture fraction, which, thus, represents the elemental mass fraction originated from the fuel stream,

$f = 1/(1 + OF)$, where OF is the local oxidizer-to-fuel mass ratio for the equivalent non-burning field. The density-averaged mixture fraction equation is

$$\frac{\partial}{\partial t}(\bar{\rho}\tilde{f}) + \frac{\partial}{\partial x_j}(\bar{\rho}\tilde{u}_j\tilde{f}) = \frac{\partial}{\partial x_j}\left(\frac{\mu_t}{Pr_t}\frac{\partial\tilde{f}}{\partial x_j}\right) + S_m \quad (3.15)$$

For the closure model describing turbulence-chemistry interaction, the variance of the mean mixture fraction \tilde{f}'^2 is introduced and an additional equation for this quantity is needed, which, according to [88], and making use of the relation between ω , k , and ε , is written as

$$\frac{\partial}{\partial t}(\bar{\rho}\tilde{f}'^2) + \frac{\partial}{\partial x_j}(\bar{\rho}\tilde{u}_j\tilde{f}'^2) = \frac{\partial}{\partial x_j}\left(\frac{\mu_t}{Pr_t}\frac{\partial\tilde{f}'^2}{\partial x_j}\right) + 2\frac{\mu_t}{Pr_t}\left(\frac{\partial\tilde{f}}{\partial x_j}\right)^2 - 2\beta^*\bar{\rho}\omega\tilde{f}'^2 \quad (3.16)$$

The shape of the assumed PDF is described by the β -function of the mean mixture fraction and its variance [89].

Finally, in non-adiabatic systems, changes in the total enthalpy H due to heat loss or gain impacts the chemical equilibrium calculation and the temperature and species of the reacting flows. Consequently, neglecting the contribution from viscous dissipation, the conduction and species diffusion terms combine to give the following total enthalpy form of the energy equation

$$\frac{\partial}{\partial t}(\bar{\rho}\tilde{H}) + \frac{\partial}{\partial x_j}(\bar{\rho}\tilde{u}_j\tilde{H}) = \frac{\partial}{\partial x_j}\left(\frac{\mu_t}{Pr_t}\frac{\partial\tilde{H}}{\partial x_j}\right) + S_h \quad (3.17)$$

where Pr_t is the turbulent Prandtl number, which is assumed equal to 0.85, and the source term S_h includes the volumetric heat of phase change (see Section 3.4.1).

Once \tilde{f} and \tilde{f}'^2 and H are calculated at each point in the flowfield, the known PDF is used to compute the time-averaged values of individual species mole fractions, density and temperature with simple thermochemistry calculations based on the minimization of Gibbs free energy [77].

3.2.3 Thermodynamic and transport properties

Heat capacities, molecular weights, and enthalpies of formation for each species considered are extracted from the solver chemical database. In particular, the specific heat of the single species is determined as a piecewise polynomial function of the local temperature, while the mixture's specific heat, C_p , is then determined as a mass fraction average of the pure species heat capacities, i.e. with the following mixing law

$$C_p = \sum_i Y_i C_{p,i} \quad (3.18)$$

where Y_i is the mass fraction of the i -th species and $C_{p,i}$ is the corresponding specific heat capacity.

Molecular dynamic viscosities and thermal conductivities of the i -th species are calculated as functions of local temperature, as

$$\ln \mu_i = A_{\mu,i} \ln T + \frac{B_{\mu,i}}{T} + \frac{C_{\mu,i}}{T^2} + D_{\mu,i} \quad (3.19)$$

$$\ln \lambda_i = A_{\lambda,i} \ln T + \frac{B_{\lambda,i}}{T} + \frac{C_{\lambda,i}}{T^2} + D_{\lambda,i} \quad (3.20)$$

where the fitting coefficient $A_{\mu,i}$, $B_{\mu,i}$, $C_{\mu,i}$, $D_{\mu,i}$, $A_{\lambda,i}$, $B_{\lambda,i}$, $C_{\lambda,i}$, $D_{\lambda,i}$, are taken from Ref. [77]. The mixture's dynamic viscosity, μ , and thermal conductivity, λ , are then calculated by means of the following mixture formula:

$$\mu = \sum_i \frac{X_i \mu_i}{X_i + \sum_{j \neq i} X_j \phi_{ij}} \quad (3.21)$$

$$\lambda = \sum_i \frac{X_i \lambda_i}{X_i + \sum_{j \neq i} X_j \psi_{ij}} \quad (3.22)$$

where X_i is the mole fraction of the i -th species, ϕ_{ij} is the viscosity interaction coefficient between species i and j in eq. (3.21) and ψ_{ij} is the interaction coefficient between species i and j in eq. (3.22). For the interaction coefficient the following form is used

$$\phi_{ij} = \frac{1}{4} \left[1 + \left(\frac{\mu_i}{\mu_j} \right)^{\frac{1}{2}} \left(\frac{M_j}{M_i} \right)^{\frac{1}{4}} \right]^2 \left(\frac{2M_j}{M_i + M_j} \right)^{\frac{1}{2}} \quad (3.23)$$

$$\psi_{ij} = \phi_{ij} \left[1 + \frac{2.41(M_i - M_j)(M_i - 0.142M_j)}{(M_i + M_j)^2} \right] \quad (3.24)$$

where M_i is the molecular weight of the species i .

3.3 Computational domain and boundary conditions

The simulations presented in CHAPTER 4 have been performed by considering an axially-symmetric flowfield for both the motor configurations. This is not exactly true for the larger motor, in which a showerhead injector is employed. In this case, the showerhead injector was modelled as a coaxial injector, whose external surface has an area equivalent to the sum of the areas of the six holes placed around the axial hole. Consequently, the numerical computations are performed with two-dimensional structured grids representing the internal volume of the pre-chamber, the fuel grain port, the post-chamber and the nozzle of the two hybrid rockets presented in Section 2.1.1.

A typical computational grid employed for the 200 N-class rocket is shown in Figure 3.1. Note that it is only an example, inasmuch as the grain length and the port diameter change for the different considered cases. As it can be observed from Figure 3.1, the cells are clustered towards the grain wall in such a way to ensure that the maximum value of y^+ is around 2÷3 at the wall-adjacent cell all along the grain length for all the considered test cases. Additional axial clustering of cells is placed in the

regions near the grain inlet and outlet edges, and near the pre-chamber, post-chamber and nozzle inner surfaces. In order to assess the convergence of the numerical results with the mesh size, grid sensitivity analyses have been performed considering three mesh refinement levels and applying the methods reported in [90] to have an estimation of the numerical errors in terms of the average computed regression rate and its components. The grid convergence analyses are described in detail in CHAPTER 4. A similar computational grid is defined for the test cases performed with the 1 kN-class hybrid rocket. The main dimensions are listed in Table 3.2.

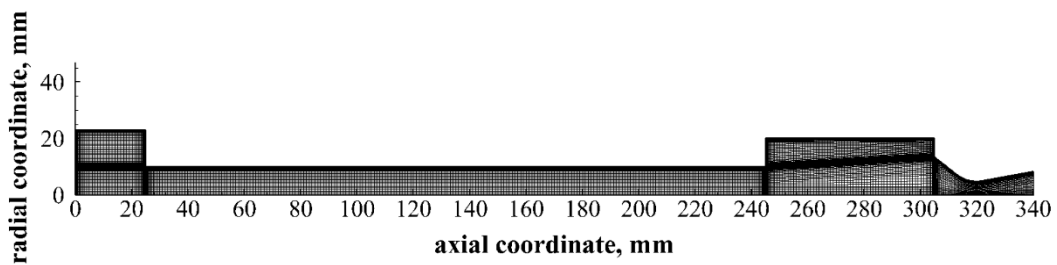


Figure 3.1 An example of the computational grid for the 200 N-class engine

Table 3.2 Computational domain dimensions.

Engine	Pre-chamber diameter	Pre-chamber length	Fuel grain length	Post-chamber diameter	Post-chamber length
200 N-class	50 mm	25 mm	220 mm	40 mm	60 mm
1 kN-class	110 mm	55 mm	350 mm	108 mm	100 mm

For what concern the boundary conditions, on the inner surface of both the pre-chamber and post-chamber as well as on the nozzle wall no-slip and adiabatic boundary conditions are imposed. At the injector exit section, a mass flow boundary condition is prescribed along with the temperature (equal to 300 K), the oxygen mass fraction and the turbulent quantities, while a pressure outlet condition is set at the nozzle exit section.

3.4 Gas/fuel surface interface modelling

The theoretical model formulation has to be completed by assigning the boundary conditions at the interface between the gaseous flow region and the solid fuel wall, which can properly describe the fuel consumption mechanism. Differently from the previous model, the liquid/gas interface temperature is an additional unknown with the regression rate to be determined. The old and new models are described below highlighting the introduced novelties.

3.4.1 The old GSI and entrainment model

A scheme of the liquefying-fuels typical consumption mechanism is shown in Figure 3.2. In the supercritical regime, part of the molten fuel on the solid surface is subjected to thermal decomposition and vaporization (i.e. pyrolysis), and part is lifted off from the surface in the form of a supercritical fluid (which, for the sake of simplicity, here is called “liquid”) that is entrained in the gas stream and burns farther from the wall. In a certain sense, pyrolysis acts in the supercritical regime similarly to vaporization in the subcritical one, except for the surface temperature which is dictated by the pyrolysis process. Based on this observation, according to Ref. [24], the fuel regression rate, \dot{r} , is assumed equal to the sum of two terms, i.e. the vaporization fraction, \dot{r}_v , determined by pyrolysis, and the entrainment fraction, \dot{r}_{ent} , related to the mechanical transfer of the liquid from the surface:

$$\dot{r} = \dot{r}_v + \dot{r}_{ent} \quad (3.25)$$

Note that this simple superposition of the two separate effects of liquid entrainment and vaporization can be derived from simplifying the mass balance at the wall for which:

$$\rho_s \dot{r} = \dot{m}_v + \dot{m}_{ent} + \frac{d\dot{m}_l}{dx} \quad (3.26)$$

where $d\dot{m}_l/dx$ is the axial variation of the melted fuel mass flow rate per unit perimeter of the port in the direction parallel to the fuel grain surface (which is

neglected), g_v and g_{ent} are the mass fluxes of the vaporized and entrained liquid, respectively. Eq. (3.25) can be, then, derived from Eq. (3.26) neglecting the change of fuel density with respect to the one in the solid state.

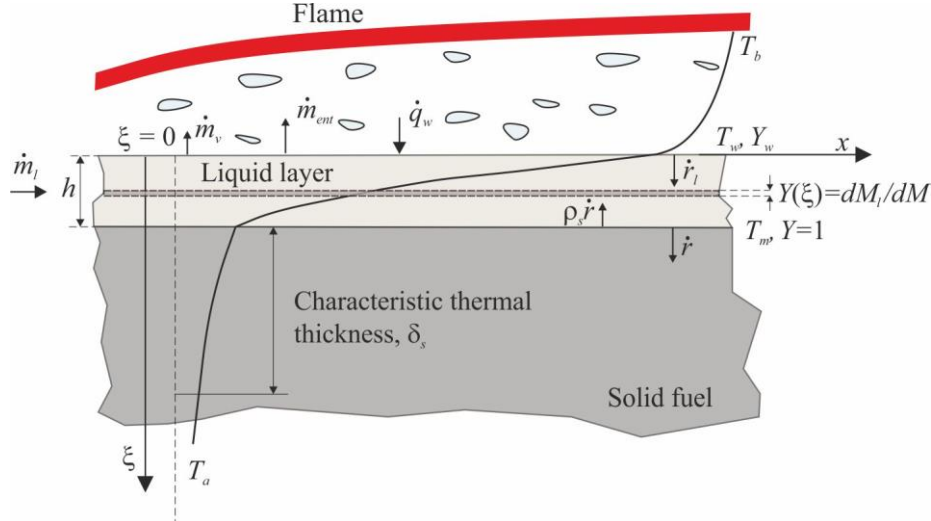


Figure 3.2 Schematic of the typical fuel consumption mechanism and heat transfer across liquefying fuels.

For the calculation of the regression rate and its two components, along with the resulting fuel mass fluxes, a set of equations needs to be formulated, whose solution is incorporated in the overall fluid dynamic computation. The required equations are derived essentially from stating the energy balance at the wall and a model for the liquid entrainment.

In the previous model [43], assuming that the pyrolysis process was concentrated in a thin layer overlaying the liquid sheet and having thickness much smaller than the latter, the heat balance was formulated as follows:

$$\dot{q}_w = - \left(k_g \frac{\partial T}{\partial \xi} \right)_w = \rho_s \dot{r} [c_s(T_m - T_a) + L_m + c_l(T_w - T_m)] + \rho_s \dot{r}_v \Delta h_p \quad (3.27)$$

where \dot{q}_w is the convective heat flux to the wall (here the radiation contribution to the heat exchanged at the wall is ignored), k_g the gas thermal conductivity, ρ_s is the solid fuel density, c_s and c_l are the specific heats of the solid and liquid fuel, respectively, T_m is the fuel melting temperature, and L_m and Δh_p are the fuel heat of fusion and heat of pyrolysis, respectively; ξ is a coordinate normal to surface oriented from the gas to solid. Eq. (3.27) expresses that the total heat flux transferred from the combusting

gases to the fuel surface must be equal to the sum of the heat conducted into the liquid layer (overall term in the square brackets on the right-hand-side) plus the energy required by the fuel vaporized fraction for pyrolysis (last term on the right-hand-side). Wall temperature, T_w , has a significant influence on the fuel regression rate, as it affects both the heat flux to the surface and the term $c_l(T_w - T_m)$ appearing in the wall energy balance in Eq. (3.27); as mentioned above, in the subcritical regime it is determined by the evaporation phenomenon and is sensitive to the chamber pressure (note that, in the latter case, the heat of pyrolysis Δh_p is replaced by the heat of vaporization), whereas in the supercritical case it depends on the pyrolysis chemical reactions for which chamber pressure above the critical value does not play a role. It has to be remarked that, compared to purely pyrolyzing polymers, due to the effect of the liquid entrainment, which is the dominant fuel consumption mechanism, with hypothetically equal regression rate, the liquefying material shows lower surface temperature than a standard polymer. However, from Eq. (3.27) only, there is no means to determine the surface temperature, because of the lack of a relationship between pyrolysis data and fuel temperature. In fact, in Ref. [43], this parameter was calculated through a sensitivity analysis to match the experimental results, for which the value of 675 K was determined. By varying the surface temperature, it was observed that larger temperature yields both lower fuel vaporization and total regression rates, whereas the entrainment component is almost unchanged; this result was qualitatively confirmed later in Ref. [91].

According to the approach described in [24] and [23], in this work, the following semi-empirical relationship has been considered for modelling the entrainment component of the fuel regression rate

$$\dot{r}_{ent} = a_{ent} \frac{1}{\mu_l \rho_g^\zeta} \frac{G^{2\zeta}}{\dot{r}^\xi} \quad (3.28)$$

where $G = 4\dot{m}/\pi D^2$ is the total mass flux in the local section of the grain port, μ_l is the fuel liquid viscosity, ρ_g is the average gas density in the chamber, ζ and ξ are correlation constants (here $\zeta = \xi = 1.5$) and a_{ent} is a constant.

Eq. (3.28) is based on theoretical considerations about the fluid dynamic stability of the surface liquid layer for which the susceptibility of a given fuel to this instability increases with decreasing viscosity and surface tension of the melt layer; the entrainment component of fuel regression rate is, therefore, roughly inversely proportional to viscosity and surface tension (to a lesser degree) evaluated at the characteristic temperature of the layer, while it depends directly on dynamic pressure, and layer thickness, which, properly rearranged, yield Eq. (3.28).

A parametric analysis has been carried out also to assess the effect of the coefficient a_{ent} . The considered values are of the same order of magnitude of the one employed in the calculation reported in Ref. [24].

Once computed the vaporization and the entrainment components, they are included in the CFD simulations as described in Section 3.4.4.

3.4.2 The new GSI

A thermal analysis, which takes into account the chemical reactions occurring in the fuel bulk, is conducted to determine the surface temperature and the thickness of the melt layer. For the pyrolysis process, the mass fraction of the liquid fuel reduces from 1 to a lower value via thermal cracking of the original alkane molecules forming the fuel core. With the assumption that the fuel port radius is much larger than the overall thermal thickness across the fuel (their ratio is usually on the order of 10 or more), a semi-infinite slab of fuel is considered divided into the two zones shown in Figure 3.2: the outer one is a thin layer of a supercritical fluid (supposed to have the same properties as paraffin in the liquid state) next to the solid surface in which the pyrolysis reactions take place; in this zone the temperature varies from the wall temperature, T_w , to the melting temperature, T_m , and a fraction of the molten fuel undergoes pyrolysis while part is mechanically removed from the surface. The inner zone is the solid fuel, whose thermo-physical properties are supposed constant, where the temperature decreases from T_m to the ambient, T_a , at infinite distance from the surface. A finite-rate kinetics approach is employed rather than the critical-temperature concept of most ablation models [92], which implies that material may volatilize in the interior of the liquid layer, rather than just at the exposed surface. The axial

temperature gradients are supposed negligible, and the effect of the radial convection in the liquid layer is ignored because of both the small melt layer thicknesses and low liquid vertical velocity, for which the Peclet number is on the order of 1; hence, the one-dimensional heat conduction equation through the pyrolysing liquid layer expressed in a reference frame moving with the regressing surface, in the steady state hypothesis (the liquid layer thickness is assumed constant) is

$$\frac{d}{d\xi} \left(\lambda_l \frac{dT}{d\xi} \right) + \rho_l c_l \dot{r}_l \frac{dT}{d\xi} + \dot{Q}_p = 0 \quad (3.29)$$

where λ_l denotes the thermal conductivity, ρ_l the density, c_l the specific heat (all assumed temperature dependent), and \dot{Q}_p is a volumetric source term to account for the heat of pyrolysis. \dot{r}_l is the liquid velocity relative to the regressing surface, which can be calculated with a simple mass balance across the liquid-solid interface whereby $\rho_l(v_l + \dot{r}) = \rho_s \dot{r}$, v_l being the liquid particle absolute velocity. The relative velocity is, therefore, $\dot{r}_l = v_l + \dot{r} = \rho_s / \rho_l \dot{r}$.

The overall gasification occurring in depth of the reaction layer is a temperature-sensitive process modelled with a kinetic rate law following an n th order Arrhenius reaction for which the energy required by the unit mass of fuel is Δh_p . The latter has been estimated by simplifying the real pyrolysis process assuming paraffin wax to decompose/gasify into ethylene and hydrogen (which are, thus, the gases injected in the computational domain from the wall) through the following reaction:



If Y represents the liquid paraffin mass fraction, i.e. the ratio of the local liquid paraffin to the total (liquid plus gasified) paraffin mass, the steady-state degradation process will evolve according to the equation:

$$\rho_l \dot{r}_l \frac{dY}{d\xi} = \dot{\omega}_p \quad (3.31)$$

in which $\dot{\omega}_p$ is the rate of production of the gas-phase per unit volume, that is, assuming a first-order reaction:

$$\dot{\omega}_p = \rho_l B_p e^{-E_a/RT} Y \quad (3.32)$$

where B_p is usually referred to as frequency factor or pyrolysis reaction rate coefficient, and has the dimension of 1/s, E_a is an activation energy, and R is the universal gas constant. Thus, the volumetric energy source in Eq. (3.29) is of the form:

$$\dot{Q}_p = -\dot{\omega}_p \Delta h_p = -\rho_l \Delta h_p B_p e^{-E_a/RT} Y \quad (3.33)$$

the negative sign is present because energy is absorbed by the degradation process.

The total mass of gas evolved per unit time and surface area in the reaction zone is found by integrating Eq. (3.32) through the liquid layer:

$$\begin{aligned} \rho_l \dot{r}_v &= \int_0^h \dot{\omega}_p d\xi = \int_0^h \rho_l B_p e^{-E_a/RT} Y d\xi = \int_0^h \rho_l \frac{\rho_s}{\rho_l} \dot{r} \frac{dY}{d\xi} d\xi \\ &= \rho_s \dot{r} (1 - Y_w) \end{aligned} \quad (3.34)$$

from which the ratio of the vaporization component to the total regression rate is readily correlated to the paraffin mass fraction at the wall:

$$\frac{\rho_l \dot{r}_v}{\rho_s \dot{r}} = 1 - Y_w \quad (3.35)$$

Eq. (3.35), indeed, represents the fact that in case the paraffin mass fraction at the wall is null ($Y_w = 0$), regression rate is entirely due to vaporization, whereas, in case all the paraffin is liquid ($Y_w = 1$), the vaporization component is zero, and the whole fuel regression occurs by liquid entrainment.

Eq. (3.29) applies also to the solid zone upon substitution of the relative material properties and on the condition that the source term is null:

$$\frac{d^2 T}{d\xi^2} + \frac{1}{\delta_s} \frac{dT}{d\xi} = 0 \quad (3.36)$$

where $\delta_s = \alpha_s/\dot{r}$ is the characteristic thermal thickness in the solid, and $\alpha_s = \lambda_s/\rho_s c_s$ is the solid thermal diffusivity. This equation can be immediately integrated with the following boundary conditions:

$$\begin{aligned} \xi = h & & T = T_m \\ \xi \rightarrow \infty & & T = T_a \end{aligned} \quad (3.37)$$

whereby the thermal profile in the solid is obtained as follows:

$$T(\xi) = T_a + (T_m - T_a)e^{-\frac{\xi}{\delta_s}} \quad (3.38)$$

and, accordingly, the thermal gradient at the interface between the solid fuel and the liquid layer, from which the heat flux into the solid is calculated:

$$-\lambda_s \left(\frac{dT}{d\xi} \right)_{\xi=h} = \frac{\lambda_s}{\delta_s} (T_m - T_a) \quad (3.39)$$

By combining the equations discussed above, a system of two ordinary differential equations is yielded in the unknown field temperature and liquid paraffin mass fraction:

$$\begin{aligned} \frac{d}{d\xi} \left(\lambda_l \frac{dT}{d\xi} \right) + \rho_s \dot{r} c_l \frac{dT}{d\xi} &= \rho_l \Delta h_p B_p e^{-E_a/RT} Y \\ \frac{dY}{d\xi} &= \frac{\rho_l B_p}{\rho_s \dot{r}} e^{-E_a/RT} Y \end{aligned} \quad (3.40)$$

with the boundary conditions:

$$\xi = 0 \quad \dot{q}_w = -\lambda_l \frac{\partial T}{\partial \xi} \quad (3.41)$$

$$\xi = h \quad \begin{cases} T = T_m \\ -\lambda_l \frac{dT}{d\xi} = \frac{\lambda_s}{\delta_s} (T_m - T_a) + \rho_s L_m \dot{r} \\ Y = 1 \end{cases} \quad (3.42)$$

Namely, at the liquid-gas interface ($\xi = 0$) the heat exchanged to the wall, \dot{q}_w , must be equal to the heat absorbed by conduction into the fuel, and the energy transfer from the liquid to the solid ($\xi = h$) must be equal to the heat conducted into the solid from the interface plus the energy required for the phase transformation. Note that the former condition is not in contrast with Eq. (3.27) that is equivalent to Eq. (3.41) in the limit of infinite activation energy (see Appendix A).

Only three boundary conditions are needed for the integration of Eqs. (3.40): given the regression rate, \dot{r} , through Eq. (3.42) they can be integrated, with an assigned value of the liquid layer thickness, from $\xi = h$ backward to $\xi = 0$, henceforth temperature and mass fraction at the wall as well as the heat flux can be calculated. From the second of Eqs. (3.40), it is clear that Y is a positive function that monotonically increases from $\xi = 0$ to $\xi = h$; thus, on the one hand, there is a maximum possible value for h , which corresponds to $Y_w = 0$ (i.e. no entrainment occurs, overall regression rate is due to vaporization), and to the maximum heat flux \dot{q}_w and surface temperature T_w achievable with the assigned regression rate (temperature and the absolute value of its gradient are monotonically decreasing from $\xi = 0$ to $\xi = h$). On the other hand, with a given regression rate, in the limit of the liquid layer thickness $h = 0$, there is no pyrolysis, i.e. $Y_w = 1$, and the required heat flux is minimum, which is:

$$\dot{q}_w = \rho_s \dot{r} [c_s (T_m - T_a) + L_m] \quad (3.43)$$

Eq. (3.43) can be readily derived from Eq. (3.27) considering that the surface temperature is equal to the melting temperature, and the vaporization fraction of the regression rate is null; it, hence, expresses that the heat flux to the wall is equal to the heat conducted into the solid (first term in the square brackets) plus the heat of melting.

However, in general h is not known, whereas the heat flux is assigned, thus an iterative procedure is required to determine the liquid layer thickness and the resulting surface mass fraction and temperature.

Paraffin-wax thermal properties as a function of temperature in the melt-layer have been estimated using the asymptotic behaviour correlations (ABCs method) reported in Ref. [81, 93] with carbon number equal to 32. In Figure 3.3 trends of the quantities, each normalized with respect to the corresponding value assumed at the melting

temperature, are plotted in the range between melting and critical temperature; also, the dynamic viscosity is depicted because, as discussed in the next section, it appears in the liquid entrainment modelling.

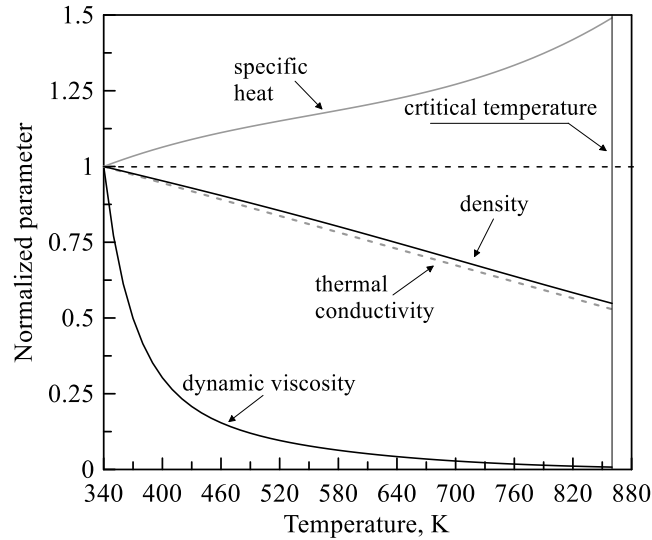


Figure 3.3 Liquid paraffin thermophysical properties as a function of temperature.

The pyrolysis reaction rate constants in Eq. (3.32), i.e. the frequency factor B_p and the activation energy E_a , have been determined according to Ref. [94]; in particular, the former has been estimated at the average pressure in the chamber, whereas the value of the activation energy for polyethylene already used in previous simulations [44] has been selected. All the material properties are listed in Table 3.3.

Table 3.3. Paraffin wax properties.

Solid phase			Liquid phase (at melting temperature)				Characteristic parameters					
ρ_s , kg/m ³	c_s , J/kg K	λ_s , W/m K	ρ_l , kg/m ³	c_l , J/kg K	λ_l , W/m K	μ_l , Pa s,	T_m , K	T_c , K	L_m , MJ/kg	Δh_p , MJ/kg	B_p , 1/s	E_a , kJ/mol
920	2030	0.325	780	2370	0.16	$7.8 \cdot 10^{-3}$	340	380	0.17	2.4	$7.6 \cdot 10^{14}$	190

With a given regression rate, the system of Eqs.(3.40) has been integrated backward with the boundary conditions in Eq.(3.42) by assigning the liquid layer thickness, h , with a fourth-order Runge-Kutta method using an adaptive step-size. The maximum value of h has been determined iteratively by imposing that the mass fraction at $\xi = 0$ was $Y_w = 0.01$ (i.e. 99% of the fuel regression is due to vaporization). The results are shown in Figure 3.4.

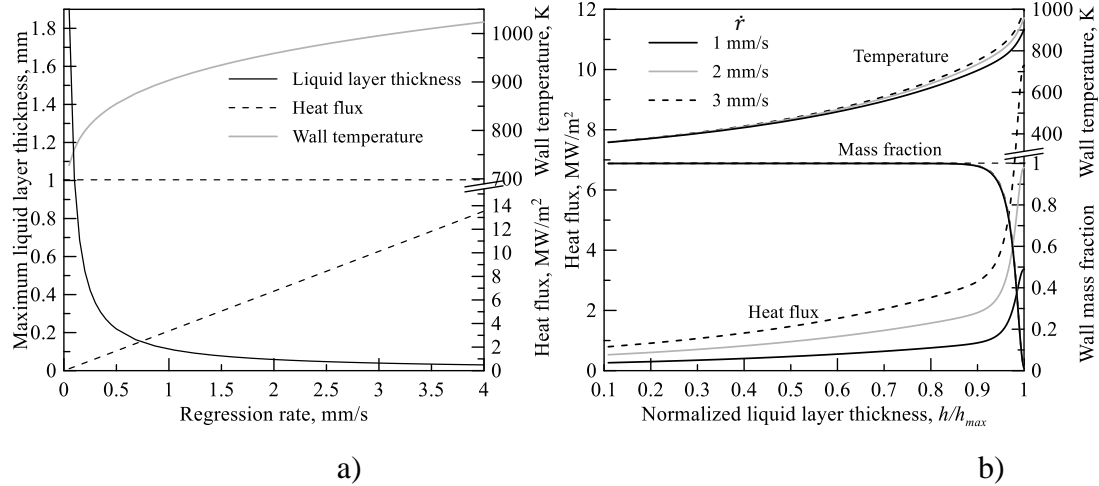


Figure 3.4 a) Maximum liquid-layer thickness, heat flux and surface temperature vs. regression rate, b) heat flux, surface temperature and mass fraction vs. liquid layer thickness.

Recall that the maximum liquid-layer thickness is achieved in the absence of liquid entrainment at the surface, that is, fuel is consumed by gasification only, $\dot{r}_v/\dot{r} = 1$; with the given regression rate, in this condition the heat flux is maximum. As the regression rate increases, both the required heat flux and the surface temperature have to increase to accelerate the fuel degradation process to allow for the complete decomposition of the material into gases (Figure 3.4a). The maximum liquid-layer thickness hyperbolically decreases with regression rate, as can be immediately derived considering that, as the regression rate tends to zero, approximately holds the relation (see Appendix A): $e^{-h/\delta_l} \rightarrow \text{constant}$, in which $\delta_l = \lambda_l/\rho_s c_l \dot{r}$ is the liquid-layer characteristic thermal thickness; thus, as $\dot{r} \rightarrow 0$, both δ_l and h must tend to infinity.

In Figure 3.4b, heat flux, wall temperature and liquid mass fraction are reported as a function of the liquid layer thickness for three values of the total regression rate; heat flux and surface temperature both increase with the thickness and the increase is

larger with larger regression rate; the three liquid layer mass fraction profiles are practically undistinguishable and show that the pyrolysis (also recall Eq. (3.35)) occurs in a portion of the layer close to the surface which is about 10% of the total thickness.

The solution of the problem in Eq. (3.40) and Eq. (3.42) has been implemented into the thermo-fluid-dynamic computations by means of a lookup table construction in order to speed up the calculations: the table has been generated in a number of total regression-rate points equally spaced of 0.1 mm/s at which Eq. (3.40) and Eq. (3.42) have been solved in 150 grid nodes in the range $h \in [0, h_{max}]$; to improve the solution accuracy close to the maximum thickness where the largest gradients are expected (see Figure 3.4b, grid nodes have been spaced non-uniformly: the first node has been placed at $2 \cdot 10^{-5}$ mm far from the maximum liquid-layer thickness, and the distance between the following adjacent points increases by 5% up to $h = 0$). Given the total regression rate, each row of the table contains the following set of values: $h, T_w, \dot{q}_w, \dot{r}_v/\dot{r}$. The access mode to the parameters in the table is described in Section 3.4.4.

3.4.3 The new entrainment law

The entrainment model considered in this work refers to the correlation methodology developed by Sawant et al. [95, 96] and the corrections proposed by Al-Sarkhi et al. [97]. This kind of methodology consists in determining the liquid entrained fraction as function of the modified gas Weber number and the maximum entrained fraction, which depends on the liquid Reynolds number.

A general model of the entrained fraction can be expressed as:

$$E = E_{max} \left(1 - \exp \left(- \frac{We_g}{We_g^*} \right) \right) \quad (3.44)$$

$$E_{max} = 1 - \exp \left(- \frac{Re_l}{Re_l^*} \right)^{0.6} \quad (3.45)$$

where We_g^* and Re_l^* are constants obtained from experiments.

The gas Weber number and the Reynolds number are defined as:

$$We_g = \frac{\rho_g u_g^2 D}{\sigma} \left(\frac{\rho_l - \rho_g}{\rho_g} \right)^{0.25} \quad (3.46)$$

$$Re_l = \frac{\dot{m}_l D}{h \mu_l} \quad (3.47)$$

where D , u_g , ρ_l , ρ_g and σ are the grain diameter, the area-averaged gas velocity on the port area, the liquid phase density, the gas phase density and the surface tension, respectively. The liquid mass flow rate was expressed as $\dot{m}_l = \rho_l u_l h$.

This definition of the liquid Reynolds number is extremely convenient for hybrid rocket applications, especially if the aim of the numerical model is to predict the behavior of the regression rate during the burn time. Indeed, high variations of the total mass flux (and consequently of liquid mass flow rate) and the grain diameter are featured during the engine operation, which are two key quantities for the correct modelling of the entrained fraction [98]. An increase in the mass flux triggers an increase in the kinetic energy of the core flow, which provides the energy that drives the liquid film atomization process and thus yields an increase in the entrained liquid fraction. A tube diameter reduction yields an increase in the stability of the liquid film.

For what concerns the Weber number, many experiments shown in Ref. [96] have displayed that when the gas Weber number exceeds a specific threshold ranging between 10^3 - 10^4 , the entrainment fraction is dependent only on the liquid Reynolds number and it coincides with the limiting entrained fraction. In the considered test cases the order of magnitude of the modified gas Weber number has been estimated to be higher than 10^4 , if the surface tension is not neglected. For this reason, one can assume that the entrained fraction coincides with the maximum entrained fraction.

The correlation for the estimation of the maximum entrained fraction has been extracted by the same work and reformulated in terms of regression rate:

$$E_{max} = \frac{\rho_l \dot{r}_{ent}}{\rho_s \dot{r}} = 1 - \exp\left(-\frac{Re_l}{1400}\right)^{0.6} \quad (3.48)$$

$$\rho_l \dot{r}_{ent} = \rho_s \dot{r} \left(1 - \exp \left(- \frac{Re_l}{1400} \right)^{0.6} \right) \quad (3.49)$$

Experiments in Ref. [97] have shown that the entrainment fraction is characterized by an upper limit above which the fuel cannot be released further in the combustion chamber in form of droplets. A full characterization of this constant is still lacking in the entrainment literature. In this work, it has been assumed equal to the highest value of the experimental campaigns shown in the work.

The derivation of the liquid mass flow rate equation was derived following the analysis proposed in Ref. [26]. Starting from the incompressible Navier–Stokes equations formulated in a moving reference frame with constant velocity, \dot{r} , normal to the liquid–solid interface, two steady components of the liquid flowfield can be recognized, which are the mean velocity of the liquid in the direction normal to the undisturbed liquid surface, \dot{r}_l , and the parallel velocity, U_0 , which is dependent on the radial coordinate y . Assuming that the pressure is only function of the time and the liquid properties are constant along the film thickness, the substitution of these quantities in the Navier–Stokes equations yields:

$$\dot{r}_l \frac{\partial U_0}{\partial y} = \frac{\mu_l}{\rho_l} \frac{\partial^2 U_0}{\partial^2 y} \quad (3.50)$$

Once imposed no-slip condition at the solid wall and the shear force balance at the gas–liquid interface:

$$U_0|_{y=0} = 0, \quad \tau_g = \mu_l \frac{\partial U_0}{\partial y} |_{y=h} \quad (3.51)$$

Eq.(3.50) can be integrated to give:

$$U_0(y) = \left(\frac{\tau_g}{\rho_l \dot{r}_l} \right) \exp \left(\frac{-\rho_l \dot{r}_l}{\mu_l} h \right) \left\{ \exp \left(\frac{\rho_l \dot{r}_l}{\mu_l} y \right) - 1 \right\} \quad (3.52)$$

Besides, it is convenient to define the liquid phase blowing parameter:

$$b = \frac{\dot{r}_l h \rho_l}{\mu_l} \quad (3.53)$$

Hence, the liquid mass flow rate can be expressed as:

$$\dot{m}_l = \int_0^h \rho_l U_0(y) dy = \left(\frac{h \rho_l}{\dot{r}_l \rho_s} \right) \left\{ \tau_g e^{-b} \left[\left(\frac{e^{-b} - 1}{b} \right) - 1 \right] \right\} \quad (3.54)$$

where the liquid layer viscosity is evaluated at the effective temperature of the melt layer, which is somewhere between the melting temperature and the surface temperature; it was evaluated as a weighted average of the melting and surface temperatures as $(T_w + 2T_m)/3$.

Noting that the interaction of the gas on the liquid surface, which experiences a Kelvin-Helmholtz instability, is much different than the shear stress exerted by a gas flow on a solid surface, it was expressed by the following correlation:

$$\tau_g = \frac{1}{2} f_{gi} \rho_g (u_g - u_l)^2 \quad (3.55)$$

$$f_{gi} = \frac{0.079}{Re_g^{-0.25}} \left(1 + 300 \frac{h}{D} \right) \quad (3.56)$$

3.4.4 Boundary Conditions at the Fuel Surface and Solution Strategy

The variables needed at the fuel surface are the velocity components, temperature, mixture fraction, turbulent kinetic energy and dissipation rate. In the following, the procedure used for the relative assignment is addressed. The fuel mass fluxes

associated to the vaporization and entrainment components, respectively, are obtained as follows

$$g_v = \rho_s \dot{r}_v \quad (3.57)$$

$$g_{ent} = \rho_s \dot{r}_{ent} \quad (3.58)$$

The vaporization and entrainment components of regression rate are handled differently for a correct evaluation of the blocking effect of the heat transfer to the surface. The vaporization component is treated in the same means as in the case of a classical pyrolyzing fuel, considering the mass and mixture-fraction balance equations at the grain wall, given by, respectively:

$$(\rho v)_w = g_v \quad (3.59)$$

$$(\rho v)_w f_w + \left(\frac{\mu_t}{Sc_t} \frac{\partial f}{\partial \xi} \right)_w = g_v \quad (3.60)$$

where f is the mixture fraction, ρ is the gas density, and v is the normal-to-wall velocity component due to the gaseous products injection, both of them evaluated at the wall; μ_t and Sc_t are the turbulent viscosity and turbulent Schmidt number, respectively (for the hypothesis of unity Lewis number, the turbulent Schmidt number is equal to the turbulent Prandtl number and they are fixed to 0.85). Eq. (3.60) simply states that the mass flux of gasified fuel entering the computational domain as a consequence of the relative regression rate fraction (which appears on the right-hand side of the equation and represents a production term) is partially balanced by convection and partially by diffusion of the fuel mass fraction f . Although the actual products of fuel pyrolysis are numerous and their composition depends on both the wall temperature and heating rate, here gaseous ethylene and hydrogen as in Eq. (3.30) are injected from the surface. The entrained liquid fuel does not contribute to the heat transfer blocking, then the resulting mass flux is not introduced into the combustion chamber from the grain wall. In fact, as a single-phase approach is used in this study on the simplifying assumption that, being the entrained paraffin in the supercritical

state, it is immediately gasified for the rapid turbulent mixing and large combustion heat release, the local entrainment contribution is uniformly assigned, as a mass production term of both the mass and mean mixture fraction balance equations, in the local volume of the grain port corresponding to the surface cell through which the fuel mass enters the fluid domain. The energy required by the pyrolysis of the liquid fuel mass flow rate is taken into account by assigning in the same volume a corresponding negative energy source term.

Balance of the mixture-fraction variance at the wall is ignored, and it is imposed to be zero. The no-slip boundary condition is enforced for the parallel-to-wall velocity component. The required level of mesh refinement near the grain surface allows for the resolution of the viscous sub-layer, so that the boundary condition for the turbulent kinetic energy is assigned enforcing null normal gradient at the surface, whereas the specific dissipation rate is imposed as suggested in the Menter's standard model for smooth walls [84].

The overall solution procedure is approached through the following steps.

- 1) Input the boundary conditions and a combustion pressure reference value; at the grain surface trial values of the unknown required temperature, regression-rate vaporization component and mixture fraction are used. Furthermore, a total regression rate is also assigned.

- 2) Computation of the thermodynamic lookup table containing the time-averaged values of species mass fractions, density, and temperature as a function of mean mixture fraction, mixture fraction variance, and enthalpy.

- 3) Solution of the mass, momentum, turbulence and mixture fraction equations.

- 4) Calculation of the spatial distribution of temperature, density and individual chemical species mass fractions by interpolating the values in the thermodynamic lookup table.

- 5) From the results of the simulation, the convective heat flux to the wall is evaluated, thereby, from the lookup table (with the wall heat flux and total regression rate) the new wall temperature, vaporization regression rate is extracted through a bilinear interpolation, and Eqs. (3.59) and (3.60) are solved simultaneously with the entrainment equation to compute the new distribution of the variables along the grain

surface and, accordingly, the mass flux distribution along with the volume source terms. Steps from 3) through 5) are, then, iterated by adjusting the local values of the mentioned quantities until convergence is reached.

3.5 Port diameter update with time for the transient simulation of the fuel grain consumption

As anticipated before, a common practice for the hybrid rocket internal ballistics numerical simulation is performing a single numerical simulation for the entire firing test considering the time-space averaged port diameter [37]. In fact, results obtained in Ref. [38] have shown that the time-and-spatially averaged regression rate obtained through simulations conducted at different grain geometries (each corresponding to a specific stage in the burn), thanks to the employed mass flux averaging definition [99], is only deviating by a few percent from the spatially averaged regression rate calculated with a single simulation at the average port diameter. However, in the competent literature, even when analyses have been performed at several stages of the motor firing, the grain inner diameter has been always considered uniform down the port; in other words, the axial non-uniformity of the regression rate has been usually neglected and the port diameter has been updated with a spatially-averaged regression rate value. In the present work, this limitation has been superseded, and in addition to the steady simulation at time-space averaged port diameter, the considered firing test cases with polymeric fuels have been also simulated updating the local port diameter at a given instant on the basis of the local regression rate calculated at the instant before.

In particular, for the surface regression the fluid-solid interface boundary changes in time; the displacements of the computational grid nodes are not uniform throughout the grain length but, rather, vary because at each point the regression rate has a different value. Furthermore, since the regression rate is defined in the direction normal to the fuel surface, due to the local surface inclination the displacement of a

generic point occurs not only along the radial direction, but also along the axial direction.

In the present work, a forward numerical integration of the local fuel regression rate has been implemented in order to calculate the grid nodes displacement. Starting from a certain grain port profile at the n -th time-step, defined by the vectors of the axial and radial coordinates x_i^n , y_i^n of the grid nodes (where the subscript i indicates the i -th node), CFD simulation is carried out with the iterative numerical procedure described before in order to compute the fuel regression rate distribution $\dot{r}^n(x_i)$ at the same time step. This regression rate is then integrated forward in order to calculate the displacement after a fixed time-step $\Delta t = t^{n+1} - t^n$, which for the i -th node can be expressed as

$$\Delta_i^n = \dot{r}^n(x_i)\Delta t \quad (3.61)$$

If we indicate with ϑ_i the local inclination of the fuel surface with respect to the axial direction in the i -th node (see Figure 3.5), the coordinates of the same node at the time t^{n+1} can be calculated as

$$x_i^{n+1} = x_i^n - \Delta_i \cos \vartheta_i \quad (3.62)$$

$$y_i^{n+1} = y_i^n + \Delta_i \sin \vartheta_i \quad (3.63)$$

allowing reconstructing the new grain port profile.

Once the new distribution is calculated, the fluid domain geometry is consequently modified, the computational mesh is adjusted to the new geometry and the numerical simulation at the new time-step is performed.

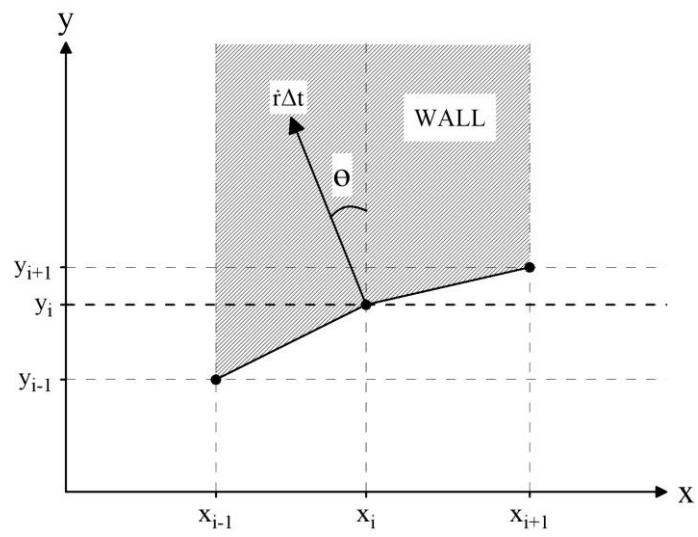


Figure 3.5. Schematic representation of the i-th node displacement components.

CHAPTER 4. NUMERICAL RESULTS OF HYBRID ROCKETS INTERNAL BALLISTICS SIMULATION

The results are divided into two sections following the chronological excursus of the achievements obtained during the PhD. Firstly, the results of the new GSI with an adapted version old entrainment model are presented; then, the new complete model is validated and compared with the old one showing all the improvements introduced in the last years.

4.1 New GSI/old entrainment model

Results obtained with the computational model combined with the novel wall treatment described above are shown in this section. A number of experimental test cases taken from Ref. [74] and resumed in Table 4.1 are used in the following section to validate the model on a single motor configuration (200N class thrust) for increasing mass flow rates keeping the burning time fixed at around 4-5s. Note that tests performed at subcritical operating conditions have been excluded for the reasons expressed above.

Table 4.1 Average operating parameters measured in the firing tests.

Test ID	Initial port diameter , mm	Oxidizer mass flow rate, g/s	Grain port diameter, mm	Oxidizer mass flux, kg/m ² s	Regression rate, mm/s
3	15	38.0 ± 0.85	26.6 ± 0.16	67.83 ± 2.30	2.04 ± 0.13
4(*)	15	42.0 ± 1.35	27.1 ± 0.1	72.58 ± 2.83	2.29 ± 0.15
5	20	55.5 ± 1.36	29.0 ± 0.04	83.75 ± 2.26	2.41 ± 0.17
6	15	59.5 ± 1.66	28.0 ± 0.12	96.76 ± 3.48	2.73 ± 0.20

7	15	60.5 ± 1.56	27.1 ± 0.1	105.22 ± 3.50	2.96 ± 0.23
---	----	-------------	------------	------------------	-------------

(*) Reference test.

4.1.1 Effect of Oxygen Mass Flux

The influence of the oxygen mass flux on the flowfield and the parameters derived at the fuel surface is analysed by taking Test 4 as a reference, maintaining the port diameter constant to the average value of 27 mm measured in the experimental test, and varying the oxygen mass flow rate. The entrainment law described in Section 3.4.1 was tuned according to the new GSI model: the entrainment parameter has been newly estimated and modified proportionally to the liquid viscosity computed at the effective temperature of the melt layer, which is somewhere between the melting temperature and the surface temperature; it was evaluated as a weighted average of the melting and surface temperatures as suggested in Ref. [94]: $(T_w + 2T_m)/3$. As a first trial, the entrainment parameter, a_{ent} , has been calculated, by scaling the value of $2.1 \times 10^{-13} \text{ m}^{8.5} \text{ s}^{0.5} / \text{kg}^3$, which was identified in Ref. [43] for the best fit with the measured average regression rate of Test 4. Note, that value lumped the constant entrainment factor with the average gas density calculated in Test 4 ($\rho_g = 1.58 \text{ kg/m}^3$) and the constant liquid viscosity; thus, with multiplying by the proper density and viscosity (evaluated at the surface temperature equal to 675 K), the first-guess scaled parameter was $a_{ent} = 5.44 \times 10^{-16} \text{ m}^3 / \text{s}^{0.5} \text{ kg}^{0.5}$, which resulted in a regression rate too large compared to the experimentally measured one. Finally, with decreasing the factor by 25% (i.e. by the ratio of the liquid viscosity at the calculated average surface temperature to that at 675 K) allowed matching the measured total regression rate with tolerance less than 1%; in conclusion, the derived constant in Eq. (3.28) is $a_{ent} = 4.0 \times 10^{-16} \text{ m}^3 / \text{s}^{0.5} \text{ kg}^{0.5}$. The variation of the gas density in the combustion port from one test case to another, as predicted by Eq. (3.28), has non-negligible effect, accordingly the entrainment regression rate is adjusted by scaling with the ratio $(\rho_g^* / \rho_g)^{1.5}$, where ρ_g^* is the average gas density calculated in Test 4.

First, a comparison with the results obtained with the constant surface-temperature model [43] is drawn for Test 4. In Figure 4.1 the axial profiles of regression rates as well as of wall heat fluxes are contrasted with each other, and in Table 4.2 the corresponding average values are listed. The average total regression rates calculated with the two models are practically equal and in excellent agreement with that measured, yielding a deviation of around 1%. The constant surface temperature estimated with the previous model is much lower than that calculated with the current one, which predicts an average value about 100 K larger; whereas, the relative vaporization fraction of regression rate is larger except in the port outlet region where it is null (Figure 4.1a).

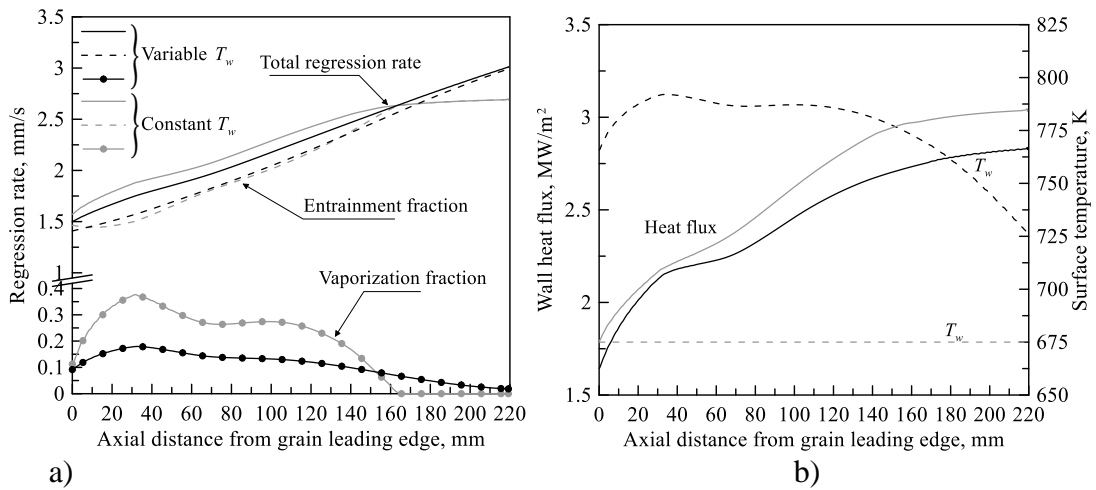


Figure 4.1 Comparison between the results obtained considering constant or variable surface temperature: a) regression rate, b) surface temperature and wall heat flux.

In fact, in the previous model, the vaporization regression rate was imposed equal to zero when the entrainment component computed with the counterpart of Eq. (3.28) exceeded the total regression rate resulting from the energy balance in Eq. (3.27), so that the total regression rate was entirely due to entrainment. Note that in the current model this unphysical behaviour is overcome as the vaporization component is associated with variable surface temperature. The regression rate entrainment component continuously increases along the grain port because of the dependence on the total mass flux and the values calculated with both models are nearly equal as expected from the mild variation of the liquid layer viscosity with temperature. As a

result, the total regression rate curves are approximately overlapped except in the outlet region where the two vaporization fractions are significantly different.

Figure 4.1b shows the computed wall heat fluxes; both are monotonically increasing down the port and tend to flatten in the zone around 30-60 mm, which, as discussed in the forthcoming paragraphs, is due to the gas recirculation in the port entrance. The heat flux, indeed, would tend to achieve a maximum point in the neighbourhood of the oxygen jet impingement point on the fuel surface (as shown in Ref. [44] dealing with classical non-liquefying fuel with slower regression), but, for the intense mass addition from the wall and the resulting growth of mass flux, it continuously increases. Overall the previous model predicts larger heat flux for the lower surface temperature; the difference increases in the outlet region where the vaporization is null for the consequent disappearance of the blowing effect.

Table 4.2. Average surface parameters calculated with variable and constant surface temperature models.

	Model	
	Variable surface temperature	Constant surface temperature
Surface temperature, K	778	675
Wall heat flux, MW/m ²	2.45	2.61
Total regression rate, mm/s	2.27	2.27
Vaporization component, mm/s	0.10	0.19
Entrainment component, mm/s	2.16	2.08

The results obtained with four different values of the oxygen mass flow rate (three more than that relative to Test 4 itself) are shown in Figure 4.2 in terms of total temperature contours, streamlines (depicted on the top half of the pictures) and fuel mass fraction isolines (on the bottom half).

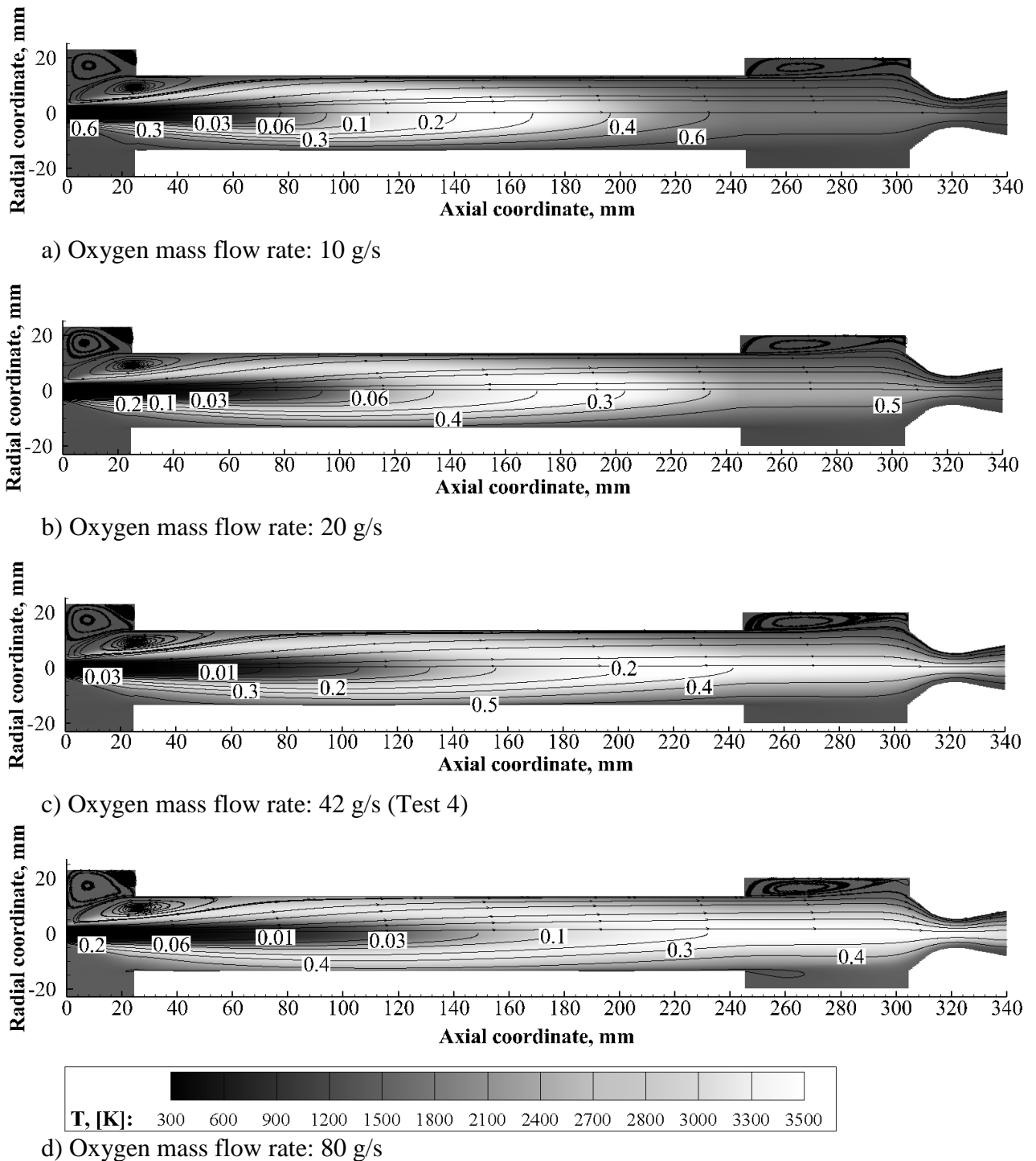


Figure 4.2 Total temperature contours plot with overlapped streamlines (top half) and mixture-fraction isolines (bottom half).

At the motor head end the typical recirculation region induced by the interaction of the oxygen discharged from the converging nozzle injector and the solid grain wall can be clearly seen. The details of the flowfield in the prechamber and fuel grain

entrance region are shown in Figure 4.3, where the oxidizer mass fraction ($1-f$) and turbulence intensity contour maps are depicted on the top half and on the bottom half of the picture, respectively. Values of the turbulence intensity map are normalized with respect to the local maximum intensity in the depicted region.

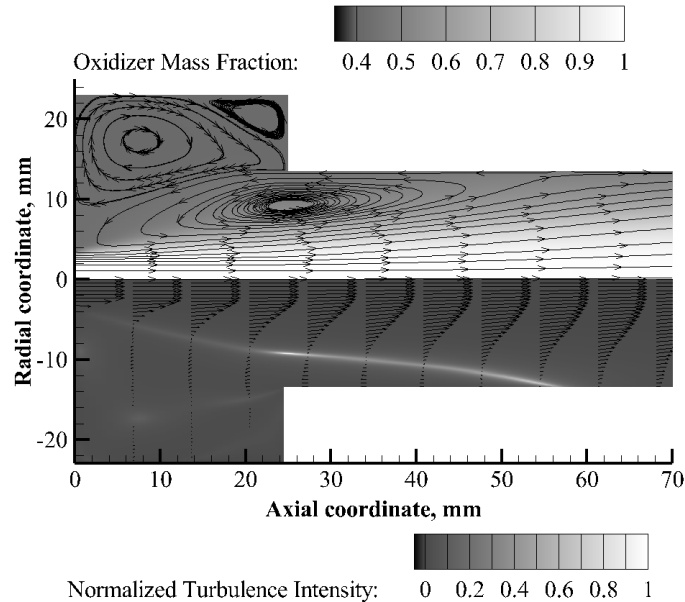


Figure 4.3 Detail of the flowfield at the motor head end (Test 4).

The core of the oxygen jet issued by the nozzle injector is visible from both the velocity vectors and the nearly unity oxygen mass-fraction area; as expected, the velocity radial profiles lose the flat shape yielded immediately downstream of the injector exit section and show the characteristic Gaussian-type shape. The edge of the jet can be recognised from the largest turbulence level achieved in the field, which occurs at the position of maximum shear, whereas at the centreline, where the shear tends to zero, turbulence strength is much less. The calculated jet spreading angle is around 10 deg, which is close to the one characteristic of a free jet [100]. The extension of the flow recirculation (which is decided by the oxygen jet spreading) is practically independent from the mass flux in the port, it being confined up to around 60 mm downstream of the injection flange in all the four test cases analysed. With given prechamber length, the main parameter affecting the extension of the recirculation in the port is, indeed, the grain port diameter, which determines the oxygen jet impingement point on the fuel surface [37]. Note that, thanks to the main vortex ring at the entrance of the fuel port, fuel is transported back to the periphery of the

prechamber where two other vortex structures contribute to mixing with the oxidizer from the jet core; the resulting local mixture ratio is equal to about 1 entailing high temperature in the prechamber also.

Whereas, by increasing the oxygen mass flow rate, the momentum of the oxygen jet increases and the cold-flow core on the port centreline tends to penetrate farther downstream along the grain. This aspect can be clearly seen from the temperature radial profiles drawn at the grain inlet ($x = 25$ mm), middle ($x = 135$ mm) and outlet ($x = 245$ mm) sections in Figure 4.4. In the inlet section, the average temperature reached with the four mass fluxes does not show significant changes, yielding a maximum at about half of the port radius. In the same section, the size of the jet core is practically unaltered, there is no mixing with the fuel, and the temperature is equal to the one at the injector outlet all over its exit section radius ($6/27 = 0.22$). In the middle section, temperature is on average larger owing to more efficient mixing of propellants, and the maximum point shifts closer to the fuel surface; interestingly, with the lowest mass flux (oxygen mass flow rate equal to 10 g/s), in the grain middle section, the oxygen-to-fuel mixture ratio is close to the stoichiometric one (the stoichiometric mass fraction value is around 0.23, see Figure 4.2a) from the port centre to about half of the section. In the outlet section, the case yielding the largest temperature is that with the largest mass flux, whereas the lowest mass flux case shows the lowest temperature.

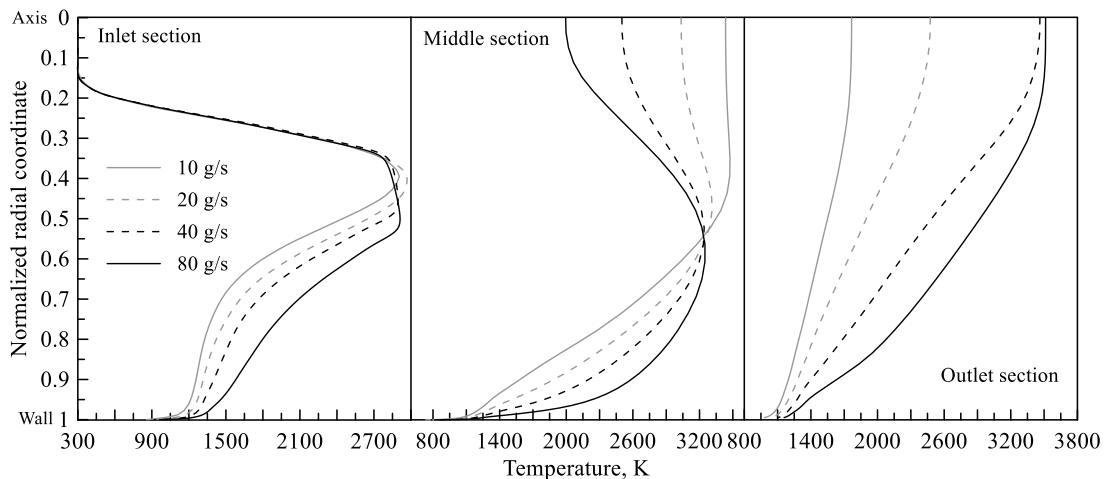


Figure 4.4 Total temperature radial profiles in the grain inlet, middle and outlet section.

In all the four cases the total regression rate increases down the port almost linearly (see Figure 4.5a), and higher is the oxygen mass flux, larger is the growth. In fact, as the vaporization fraction is less than 10% (Figure 4.1b), it can be neglected in Eq.(3.25), and from Eq. (3.28) it can be readily derived that the regression rate roughly depends on the total mass flux raised to the power of 1.2. Hence, by means of integration of the mass balance equation in the port, $dG = 4\rho_s \dot{r} dx/D$, the local total mass flux is determined, hence one obtains [99]:

$$\dot{r} = aG_{ox}^{1.2} \left(1 - 0.8 \frac{a\rho_s}{D} G_{ox}^{0.2} x\right)^{-6} \quad (4.1)$$

in which the coefficient $a = (a_{ent}/\rho_g^{1.5} \bar{\mu}_l)^{0.4}$, and $\bar{\mu}_l$ is the average value of the liquid viscosity on the fuel surface; by expanding Eq. (4.1) in series up to the first order, the following regression-rate approximate expression is immediately derived:

$$\dot{r} \cong aG_{ox}^{1.2} \left(1 + 4.8 \frac{a\rho_s}{D} G_{ox}^{0.2} x\right) \quad (4.2)$$

which, being the term $0.8a\rho_s L/D G_{ox}^{0.2}$ close to 0.5, explains the axial trends in Figure 4.5a.

The vaporization regression rate, as expected, grows with the oxygen mass flux, and the axial trends show maximum points about 35 mm downstream of the inlet (which is more evident from Figure 4.5b where the vaporization-to-total regression rate ratio is depicted), i.e. where the oxygen jet impinges on the fuel wall and, as remarked above, the heat flux tends to flatten (Figure 4.1b); the surface temperature displays similar axial profiles.

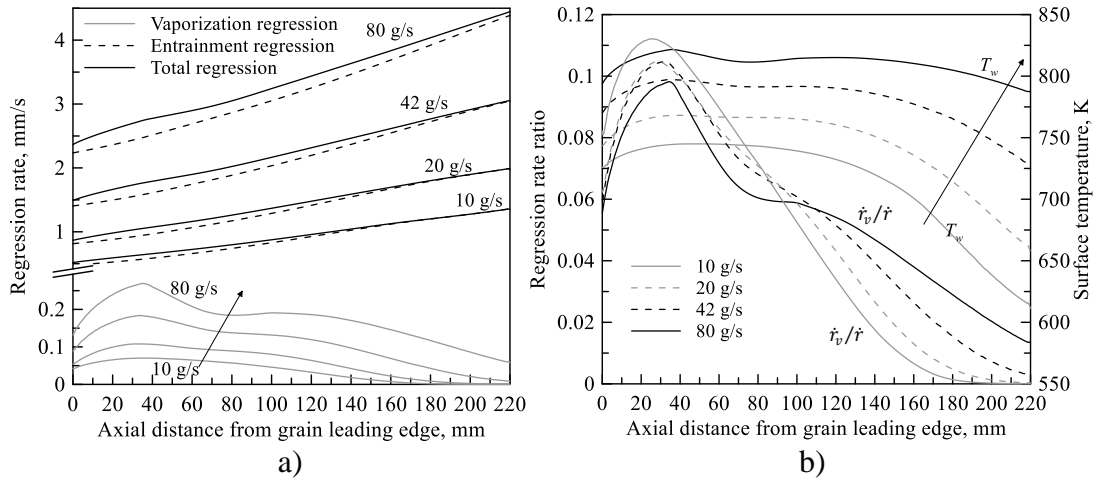


Figure 4.5 Axial distribution of fuel surface parameters: a) regression rate components, b) vaporization-to-total regression rate ratio and surface temperature.

Interestingly, despite the different axial profiles, the peak value achieved by the ratio \dot{r}_v/\dot{r} over the port length is nearly equal to 0.1 regardless of the mass flux, whereas the average ratio increases with the mass flux itself.

Eq. (4.1) can be analytically integrated over the port length to calculate the space averaged regression rate, \dot{r}_L , to give:

$$\dot{r}_L = 0.25 \frac{D}{L} \frac{G_{ox}}{\rho_s} \left[\left(1 - 0.8a\rho_s \frac{L}{D} G_{ox}^{0.2} \right)^{-5} - 1 \right] \quad (4.3)$$

A comparison between the results obtained with Eq. and the exact values derived from the CFD simulations is shown in Figure 4.6 (where one more case at 30 g/s oxygen mass flow rate is included); it is clear that Eq. (4.3) underestimates the regression rate, as expected because of the vaporization component drop in Eq. (3.28). The underestimation is, indeed, higher with larger mass flux as the latter entails larger vaporization; however, in the analysed conditions, it is lower than 5%.

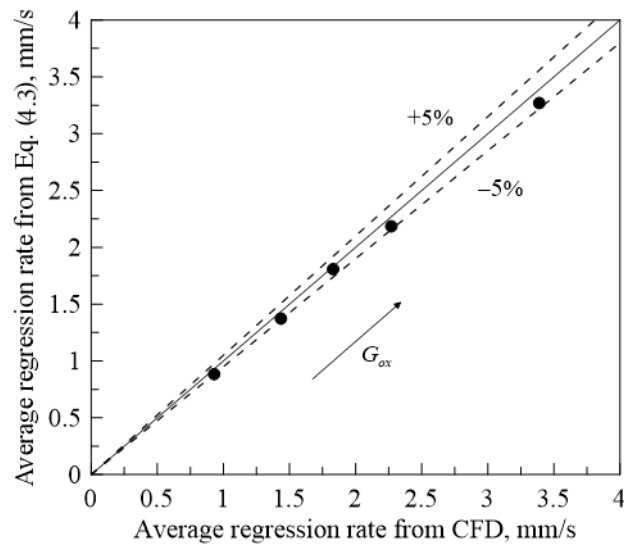


Figure 4.6 Space-average regression rate error.

4.1.2 Computational Grid Sensitivity and Validation

With reference to Test 4 shown in Table 4.1, a grid sensitivity analysis was carried out with three mesh refinement levels to determine the dependence of numerical results on the spatial discretization. A coarser and a finer mesh are constructed starting from the reference mesh: they are generated respectively doubling and halving the cell size in both the axial and the radial directions (in the clustering zone the size is set only for the first layer, while the size of the subsequent layer depends on the bunching law). Figure 4.7 shows a log-log plot of the numerical error versus the minimum grid size for the average values of the total regression rate and the grain surface temperature.

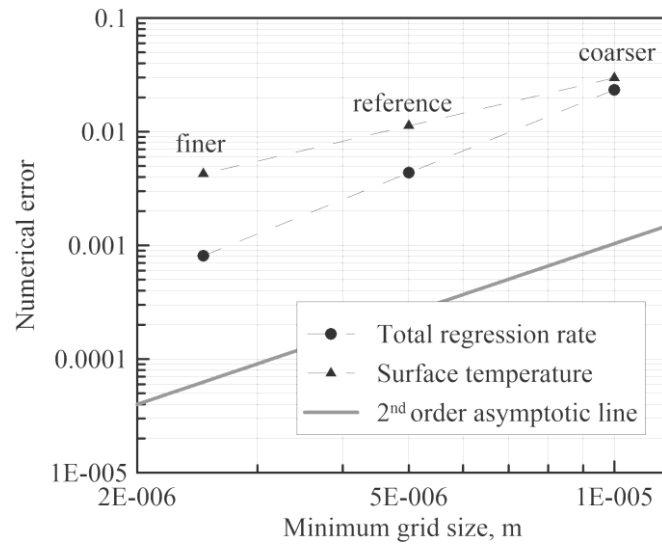


Figure 4.7 Numerical error versus grid size.

The numerical error is calculated as the relative difference between the value obtained in the simulations (which are resumed in Table 4.3) and the relevant Richardson's extrapolation. A maximum deviation of 2.5% with respect to the finer mesh is calculated for the surface temperature. The total regression-rate deviations are less than 2%. Therefore, a satisfactory approximation of the numerical results is believed to be obtained with the reference mesh.

Table 4.3. Grid sensitivity analysis results (Test 4).

Mesh refinement	Total regression rate, mm/s	Surface Temperature, K
Coarser	2.307	760
Reference	2.268	774.5
Finer	2.262	780

Numerical simulations were carried out in the conditions of oxygen mass flow rate and average port diameter of the firing tests in Table 4.1 with the constant value of the entrainment parameter discussed above; the results in terms of the calculated average regression rate are listed in Table 4.4 with the relative deviations from the experimental data. The calculated regression rates are biased to values all lower than the experimental ones, which can be adjusted by properly increasing the entrainment factor. However, the maximum error is 4.5%, which was believed acceptable in order to demonstrate the model capability.

Table 4.4 Computed regression rate deviations from experimental data.

Test ID	Calculated space-averaged regression rate, mm/s	Error relative to experimental data
3	2.04	-0.15%
4	2.27	-0.9%
5	2.30	-4.5%
6	2.62	-4.1%
7	2.85	-3.4%

By looking at the average port diameters in Table 4.1 and the corresponding regression-rate percent deviations in Table 4.4, a correlation between the port diameter and the magnitude of the deviation from the experimental data seems to be possible: with larger port diameter, the calculated regression rate tends to be increasingly lower than the measured one. This tendency was somewhat expected and is supposed to be produced by the effect of the recirculation region at the port inlet that grows with the port diameter. The employed entrainment model, indeed, neglects the skin friction variation and, thus, is not able to adequately capture the mass transfer phenomenon in the presence of recirculation. Recall that with 27-mm diameter, the recirculation is confined into the fore 10% of the port length.

Test points are plotted as a function of the oxygen mass flux in Figure 4.8 along with the data calculated at the constant port diameter of 27 mm presented above. Test data follow the same trend displayed by the total regression rate calculated at constant diameter, which yields a dependency on the oxygen mass flux in the form of a power with the exponent equal to about 0.6. By expanding Eq. (4.3) in series, the average regression rate can be approximated to $\dot{r}_L = aG_{ox}^{1.2}$, in which the factor a actually depends on the mass flux through the average gas density in the port, which increases with the latter, implying a regression-rate variation with the mass flux lower than what explicitly appears in Eq. (4.3). It is worth remarking that also the calculated regression rate vaporization component increases with a mass-flux power, but yielding 0.8 exponent. This larger exponent is equal to that predicted by the classical turbulent

boundary-layer diffusion limited regression rate model [16], and confirms that the surface vaporization is mostly dictated by the heat transfer to the wall.

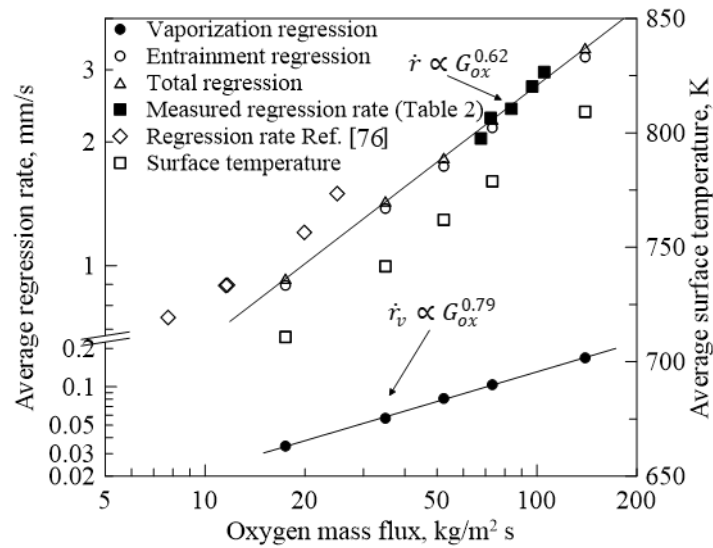


Figure 4.8 Average regression rates and surface temperature vs. oxygen mass flux.

On the same diagram five test points from the literature are overlapped [78]. They have been retrieved from ground firing a smaller hybrid rocket burning gaseous oxygen with a microcrystalline-wax based fuel with 100 mm grain length and 40 mm initial port diameter, under lower mass fluxes. The measured regression rates are larger than those measured in Naples by nearly 25%, but seem to show the same trend (equal slope on the mass flux basis). The reason can be inferred considering that tests in Ref. [78] were conducted at substantially lower chamber pressure (in the range 3 - 7.4 bar) for which wax is below the critical pressure regime, and the gas density in the port is also lower than that obtained in the current tests; according to Eq. (4.3), regression rate is, therefore, expected to be lower. To support this hypothesis, in all the tests (i.e. both current ones and those in Ref. [78]) regression rate has been calculated with Eq.(4.3) in which the gas density has been estimated from the measured propellant mixture ratio and pressure in thermochemical equilibrium conditions. Fuel surface temperature has been assumed equal to 700 K for tests in Ref. [78] based on the arguments in Ref. [94]. The entrainment factor (which essentially depends on the fuel properties) has been kept equal to that used in the CFD simulations presented here. Results are shown in Figure 4.9; the agreement between the estimated and measured regression rates is fair

in all the cases being within $\pm 10\%$, which gives a reasonable basis to the observation advanced above.

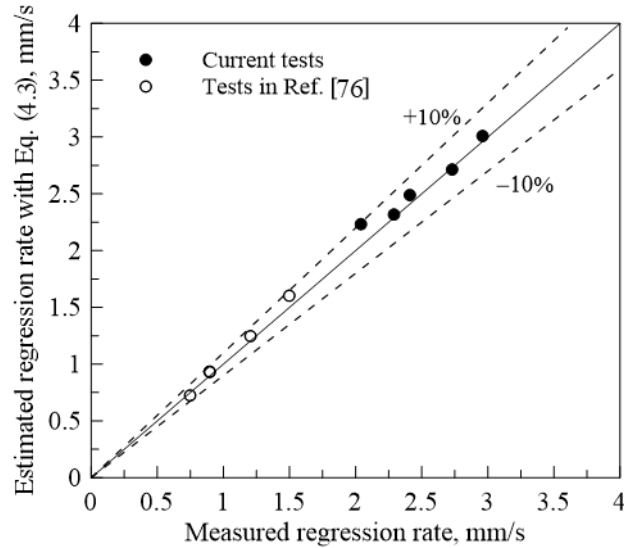


Figure 4.9 Average regression rate estimated with Eq. (4.3).

4.2 New GSI/New entrainment model

4.2.1 Experimental tests for new model assessment

For the validation and comparison of the numerical model coupled with the gas/surface interface treatment for liquefying fuels presented in this section a number of firing tests have been collected with the subscale hybrid rocket demonstrator burning paraffin-based fuel grains, made of a blending of a low-melting point paraffin wax and a microcrystalline wax, with gaseous oxygen axially injected in the grain single port.

In particular, five test cases are considered here, whose main parameters are summarised in Table 4.5. Tests performed with the smaller engine (Tests S) were carried out by varying the oxidizer mass flow rate and the time-space average port diameter obtained in the firing, with the aim of achieving a significant range of the oxidizer mass flux. Tests 1L and 2L are chosen for the larger motor configuration, because they are featured by the same oxidizer mass flux of the test 2S, but the

averaged regression rate is highest in the test with the largest average grain diameter. Note that test 2S and 3S coincide with test 4 and 7 of Table 4.1. The challenge is to develop a numerical model able to predict this trend and consequently, the effects of the recirculating zone.

Finally, Figure 4.10a and Figure 4.10b show the trend of the motor operating pressures and oxidizer mass flow rates over the burning time.

Table 4.5 Experimental data of firing test cases with paraffin-based fuel grains performed with the 200 N-class hybrid rocket.

Parameter	Test 1S	Test 2S	Test 3S	Test 1L	Test 2L
Time-averaged oxygen mass flow rate, g/s	25.0 ± 0.35	41.5 ± 1.35	60.4 ± 1.56	195 ± 3.91	243 ± 4.76
Time burning, s	5.8 ± 0.15	5.2 ± 0.25	4.1 ± 0.21	7.5 ± 0.18	9 ± 0.22
Time-space averaged regression rate, mm/s	1.81 ± 0.16	2.38 ± 0.17	2.96 ± 0.23	2.53 ± 0.19	2.99 ± 0.24
Initial oxidizer mass flux, kg/m ² s	141.47	237.67	342.36	155.18	193.37
Time-space averaged oxidizer mass flux, kg/m ² s	48.81 ± 1.54	70.45 ± 2.83	105.22 ± 3.5	72.35 ± 2.85	69.94 ± 2.81
Time-averaged overall mixture ratio	0.85 ± 0.12	1.02 ± 0.1	1.20 ± 0.11	1.29 ± 0.12	1.20 ± 0.10
Initial port diameter, mm	15	15	15	40	40
Grain length, mm	220	220	220	350	350
Time-space-averaged port diameter, mm	25.54 ± 0.3	27.1 ± 0.1	27.1 ± 0.1	58.58 ± 0.17	66.51 ± 0.19
Postburn space-averaged port diameter, mm	36.07	39.8	39.2	75.08	93.42
Fuel mass consumption, kg	0.171	0.212	0.206	1.138	1.823
Nozzle throat diameter, mm	9.8	10.6	10.6	21.2	21.2
Nozzle expansion ratio	2.87	2.45	2.45	4.04	4.04
Time-averaged aft-chamber pressure, atm	8.3	13.0	19.1	15.9	20.9

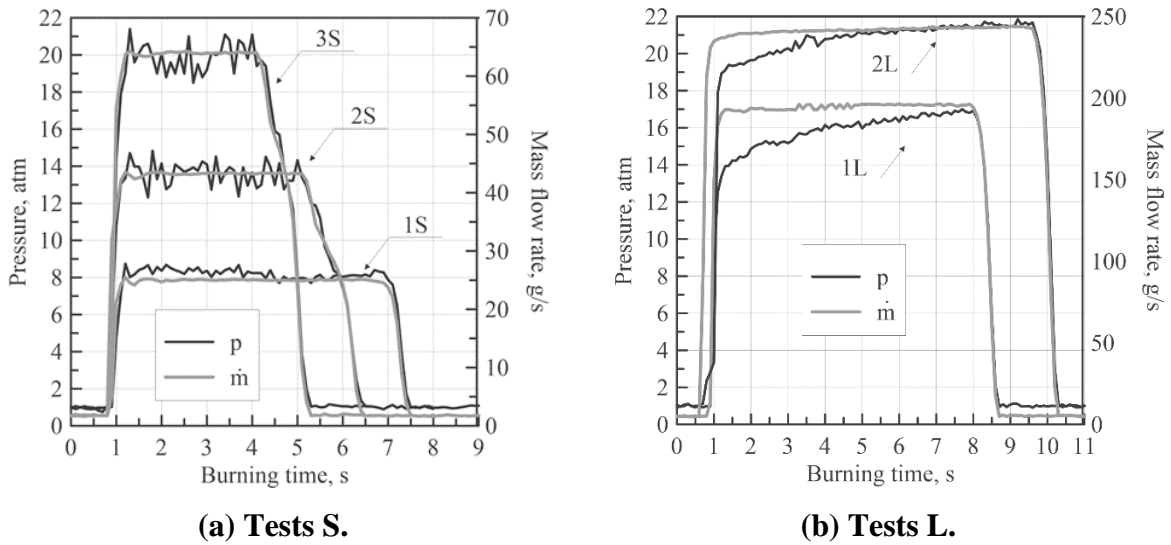


Figure 4.10 Operating pressure and thrust vs time.

4.2.2 Numerical Model Validation

In this section a comparison between the numerical results and the corresponding experimental data for the five test cases is presented. Table 4.6 resumes the obtained numerical averaged regression rates by both the models compared to the experimental values; in all the five cases the deviation is below 8%. Figure 4.11 shows the comparison of the regression rate profiles computed by the two models with the experimental one. The improvements introduced by the novel gas-surface interface and entrainment models can be qualitatively and quantitatively recognized in the pictures. The profiles computed by the new model perfectly follow the experimental trend for both class thrust motors excepting for the last experimental points of the Test 1S, which are characterized by an anomalous sudden growth of the regression rate due to some imperfections of the grain structure at the end of the grain length, that was not shown by the other two tests S.

In particular, the new numerical model has shown the capability to reproduce the internal ballistic of larger motor, in which the consumption mechanism is such different from that in the smaller scale (a full discussion is present in the next section). Whereas, the profiles computed by the old model show its inadequacy to predict the

regression rate in the tests L and large discrepancies with the experimental profiles for the tests S.

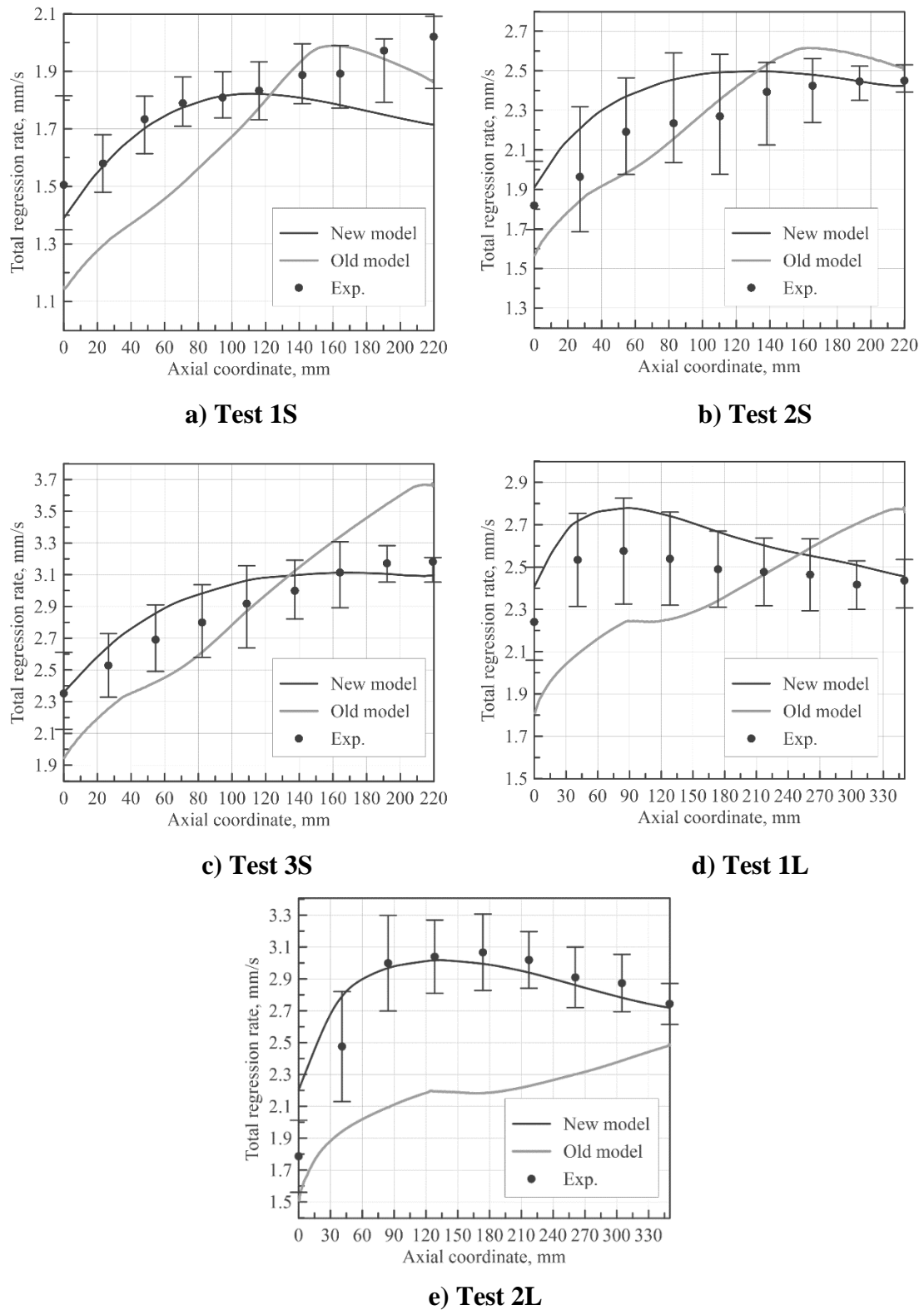


Figure 4.11 Comparison of the time-averaged regression rate profile obtained by

both the models with the experimental data.

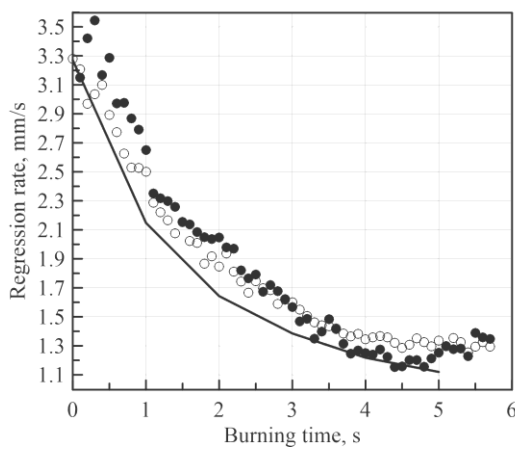
Table 4.6 Time-space-averaged regression rate computed by both the models and the experimental value with the corresponding deviations.

Test	Experimental (mm/s)	Old model (mm/s)	New model (mm/s)	Deviations old model, %	Deviations new model, %
1S	1.81	1.67	1.73	7.73	4.42
2S	2.38	2.26	2.39	5.04	0.41
3S	2.96	2.88	2.95	2.7	0.34
1L	2.53	2.37	2.63	6.3	3.8
2L	2.99	2.17	2.86	27.42	4.35

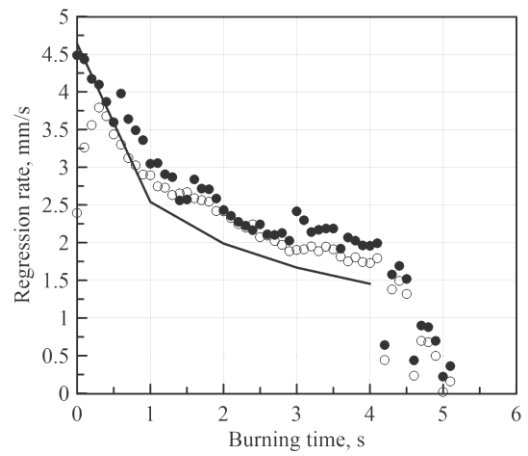
The regression rate reconstruction technique described in Section 2.3.2 has been also employed in order to prove the capability of the overall numerical model to predict not only the time-space averaged-regression rate but also the temporal evolution during the burning time.

Figure 4.12 shows the comparison of the computed regression rate and the results obtained by the complete and the simplified reconstruction technique, which provide the spatial average regression rate at each timestep during the burning time. The meaning of complete and simplified technique was described above in section 2.3.2. As shown, a good agreement can be observed in all the five tests except with the tests 1L and 2L, in which a continuous trend of the reconstructed regression rate can be detected only by the simplified method for the issues cited above and in Ref. [78]. The trend of the regression rate during the burning time is different in the two configurations. In the smaller motors, the regression rate of the tests S strongly decreases in the first timesteps due to the rapid enlargement of the port area. This is more evident in the test 3S, in which the fall is of 50% than that computed at the initial timestep. On the other hand, the regression rate drop of the tests L is less pronounced, because the consumption is sustained by the additional contribution of heat flux supplied by the recirculating bubble, whose effect becomes important for larger scale

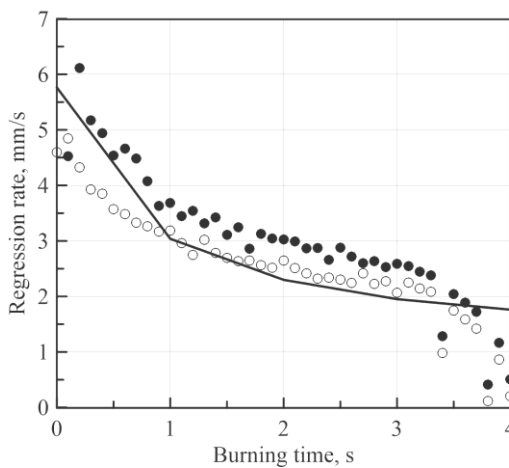
motor. Therefore, because the diameter does not change linearly with the time (in particular for the tests S), the practise of performing simulations at time-space-averaged constant diameter involves an additional error in the regression rate computation. As a proof, two further simulations were carried out at the average grain port diameter of the tests 2S and 2L, which resulted in a regression rate of 2.65mm/s and 2.90mm/s, respectively. Test 2S exhibited the highest deviation with respect the regression rate computed by the transient method, because the trend of the regression rate during the burning time is far to be linear.



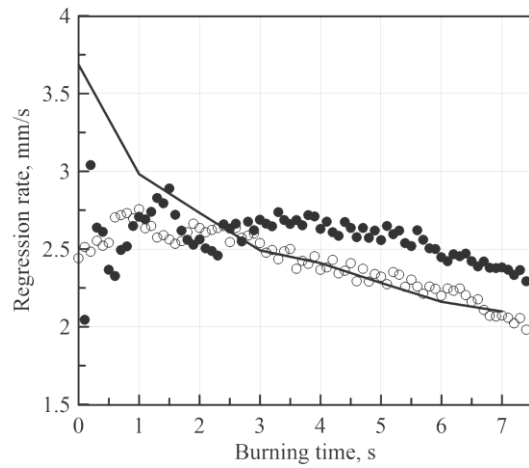
a) Test 1S



b) Test 2S



c) Test 3S



d) Test 1L

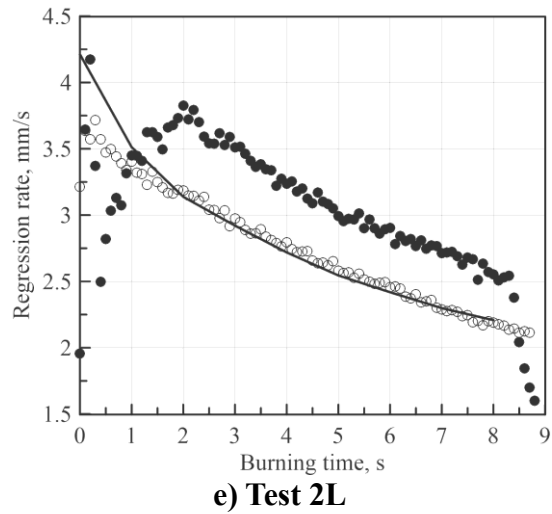


Figure 4.12 A comparison between the computed spatially averaged regression rate (black line) and the experimental one rebuilt by the complete (black dot) and the simplified (white dot) reconstruction technique.

As mentioned in section 2.3.2, the simplified reconstruction technique involves a simplification, whose impact on the solution accuracy is investigated here. The analysis considers test 2L. It has demonstrated the highest chamber pressure and thrust raise, which is attributed to an increasing mass flow rate due to enhancement of wall heat flux of the recirculating zone. Because the chamber pressure changes of $\pm 6.2\%$ with respect the average value of 20.9 bar, it can be assumed that the fuel mass flow rate shifts of the same percentage with a range of OF included between 1.27 and 1.13, to which corresponds a characteristic velocity of 1518 and 1418 m/s, respectively. A new regression rate reconstruction is performed by considering a linear variation of ηc_{th}^* during the burning time. Figure 4.13 shows the results compared with the curve obtained by assuming ηc_{th}^* constant. As shown, the curve is higher in the first second and lower in the last instants, but the differences are negligible. Therefore, the assumption of ηc_{th}^* constant during the firing test can be considered a good approximation.

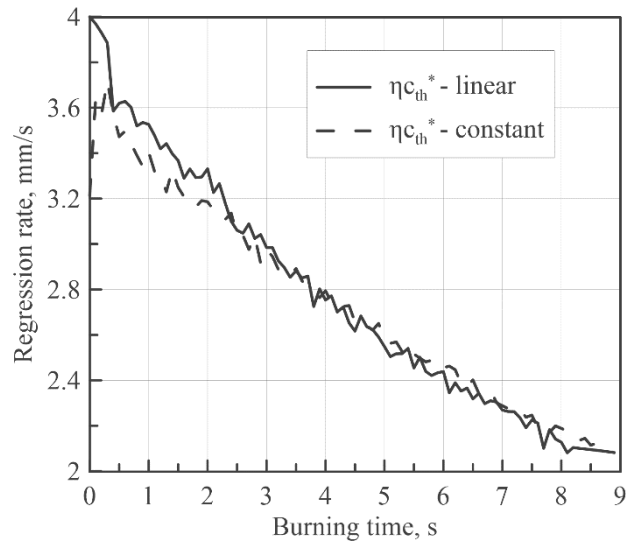


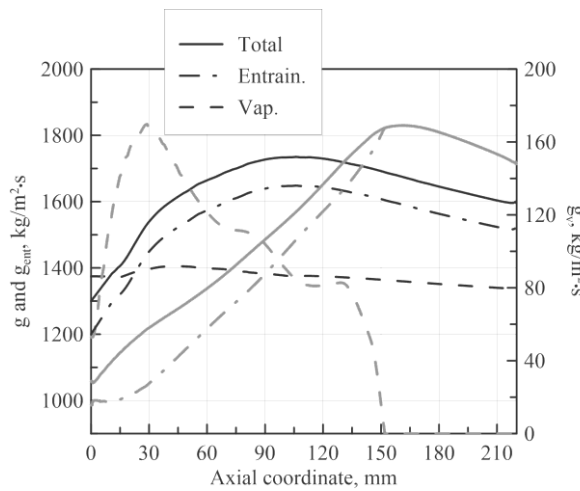
Figure 4.13 Comparison between the reconstructed regression rate by assuming constant and a linear variation of ηc_{th}^* .

4.2.3 Comparison with the old model

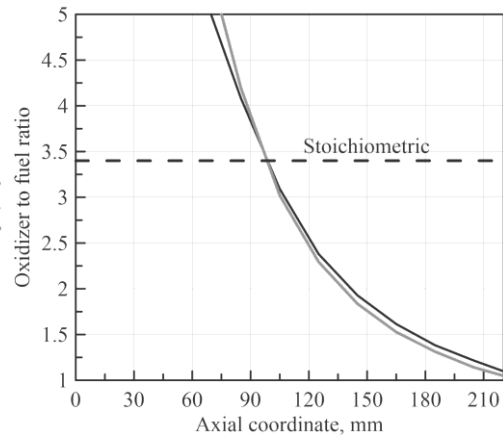
In this subsection, the improvements introduced by the new model are shown comparing the results of the Test 1S with that obtained by the old model. The numerical analyses carried out using the old model have been performed at the space- and time-averaged port diameter, while the transient procedure described in Section 3.5 was adopted to perform the analysis by the new model. In this case, the represented results in Figure 4.14 have been obtained by time-averaging the profiles of each timestep.

Figure 4.14a shows the comparison of the time-averaged regression rate flux component between the two models. As shown, the trend of the total regression rate flux in the old model continuously increases along the motor axis until $x=180$ mm following the behavior of the total mass flux, from which the entrainment component is strictly dependent. Downstream to that point, the vaporization is imposed equal to zero and the dependence on the mass flux is removed. In the last slices, the regression rate flux appears to be function of the corresponding difference between the temperature averaged along the radial coordinate in the chamber and the wall temperature, ΔT , which is displayed in Figure 4.14c.

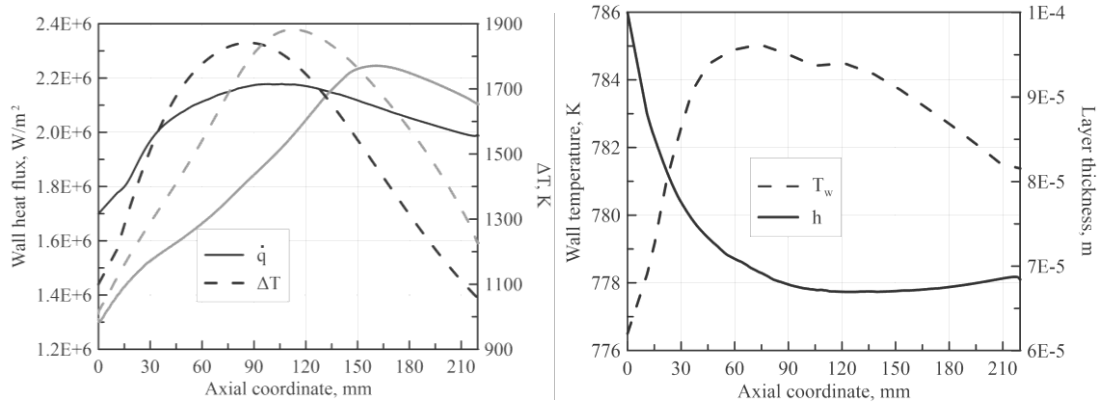
On the contrary, the trend of the total regression rate in the new model changes according to the wall heat flux, which can be outlined as the product of the heat transfer coefficient, h_t , and ΔT , defined as the difference between the local port average temperature and the corresponding wall temperature. Indeed, \dot{q} increases with the temperature reaching a maximum around 125 mm, where the stoichiometric conditions are obtained (see Figure 4.14b), while after it decreases less rapidly than ΔT because of the growth of h_t due to the adduction of fuel mass flow rate in the chamber. Figure 4.14d shows the computed wall temperature and melt layer thickness. The temperature slightly changes along the chamber axis in a range between 776.5K and 785K, which is 100K higher than that imposed in the old model, and it changes according to the wall heat flux. On the other hand, the melt layer thickness is inversely proportional to the total regression rate, which agrees with the analysis proposed in Ref. [24].



a) Components of the regression rate fluxes.



b) Section averaged oxidizer to fuel ratio.



c) Wall heat flux and ΔT ($=\bar{T}_{ch} - T_w$).

d) Wall temperature and thick melt layer.

Figure 4.14 A representation of the results of the new (black line) and old (grey line) gas/surface model coupled with the corresponding entrainment model.

4.2.4 Effect of the Engine Size

In this section, the main effect of the engine size on the consumption during the burning time is described. Figure 4.15 shows the port diameter advancement of tests 2S and 2L. The profiles follow the behaviour of the wall heat flux, which is strictly linked to the temperatures achieved in the chamber in the test 2S, while an augmentation occurs in the test 2L at the area concerned by the attachment of the gas flow on the grain after the recirculating zone, which shifts between 70 mm and 210 mm from the injector during the burning time. In this case the highest consumption is observed right in this range. As a proof, Figure 4.16 shows the computed wall heat flux on the grain surface and the average temperature along the motor axis of the two tests at the initial time. The wall heat flux rises up from 5.36 to 6.12 MW/m^2 in correspondence with the end of the recirculating zone in the test 2L, while this peak cannot be observed in test 2S, in which the bubble size is negligible. This can be also visualized in the contours represented in Figure 4.17, which highlights the difference in size of the bubble especially in the last time-step. It can be observed that an increasing size of the bubble yields to an increasing mixing of fuel and oxidizer in the

most first grain centimetres. Indeed, the mixture fraction displayed at the bottom of Figure 4.17 is approximately equal to 0 in the test 2S at $t=0s$, while it is near the stoichiometric in the test 2L.

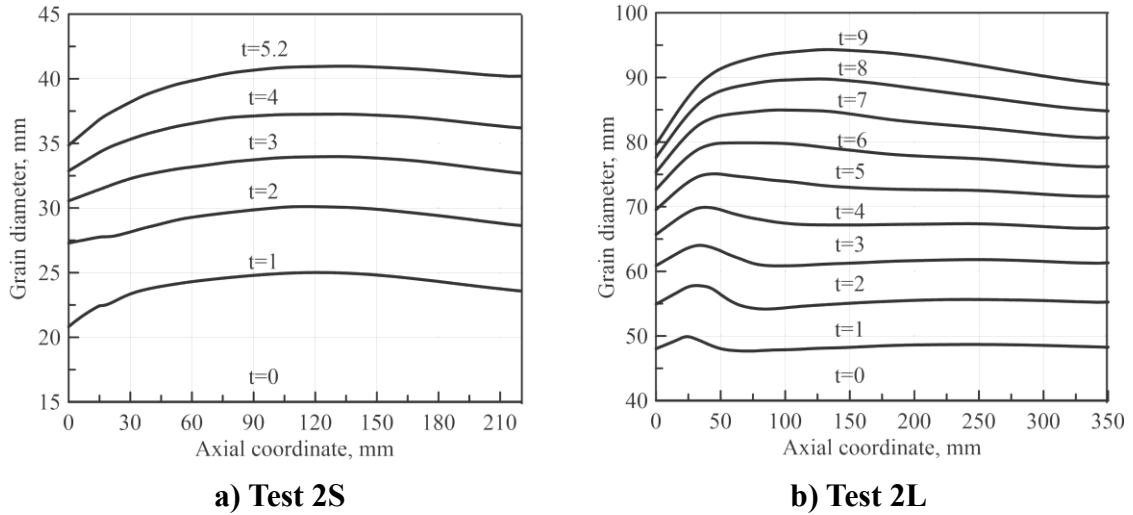


Figure 4.15 A representation of the grain consumption profile during the burning time.

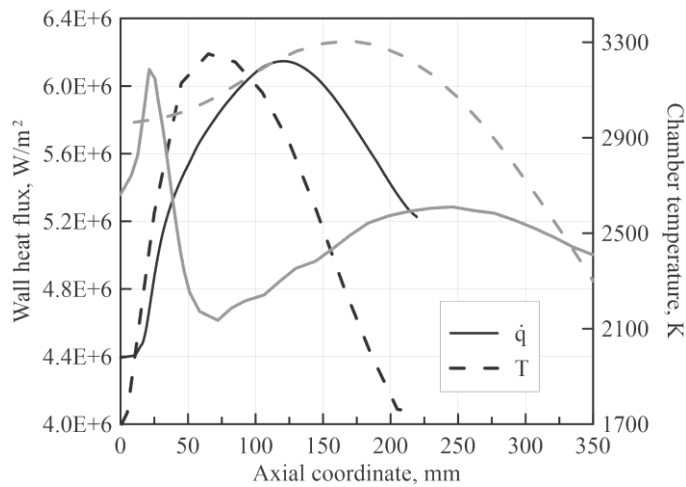
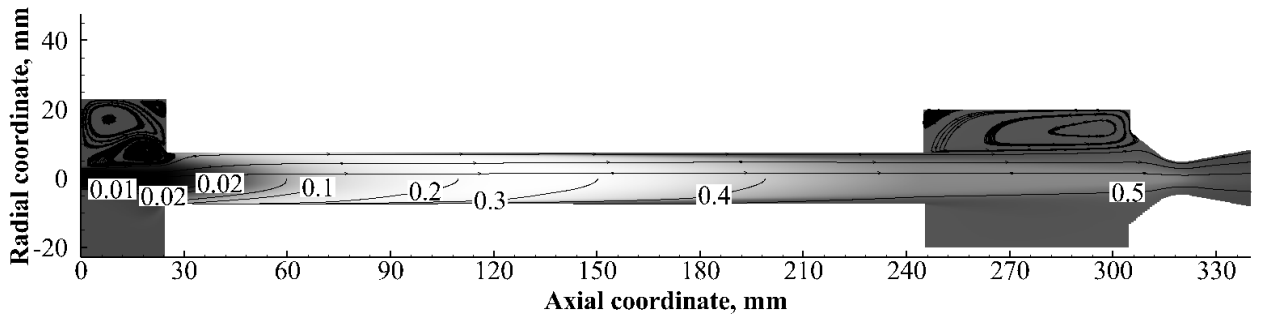
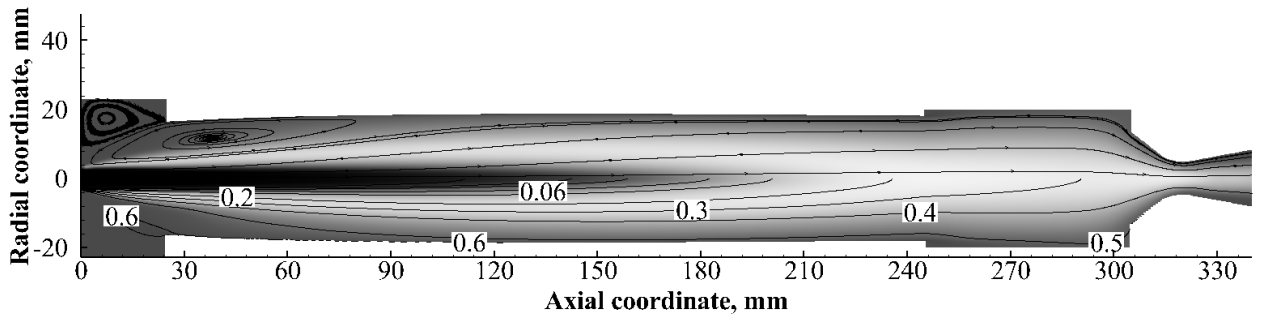


Figure 4.16 Comparison of the wall heat flux and the cross section-averaged temperature profile along the motor axis of the tests 2S (black line) and 2L (grey line) at the initial time-step.

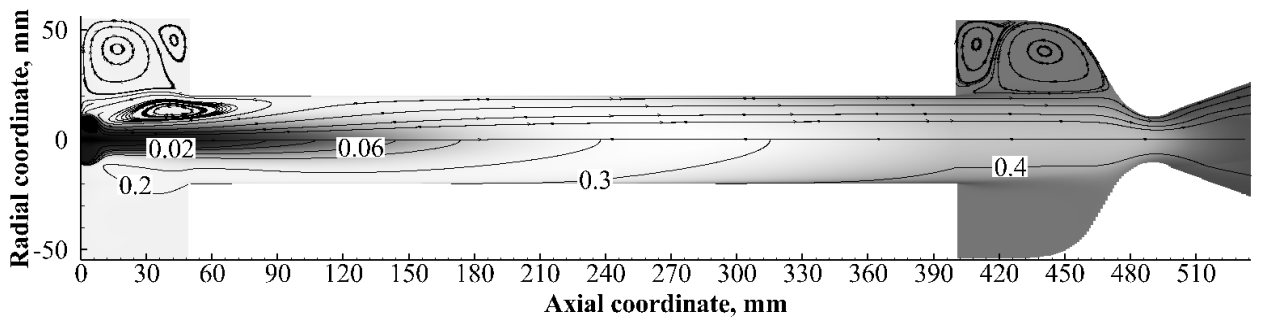
a) Test 2S, $t=0s$



b) Test 2S, $t=4s$



c) Test 2L, $t=0s$



d) Test 2L, $t=8s$

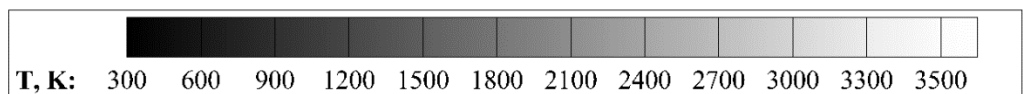
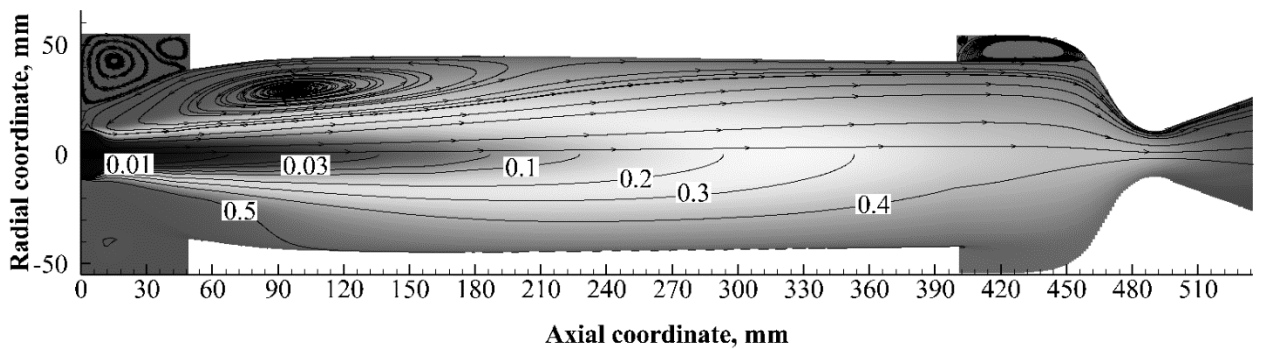


Figure 4.17 Temperature contour plot with overlapped streamlines (top half) and mixture fraction iso-lines (bottom half) of the test 2S and 2L at the initial and final time-step.

This suggests that the unique dependence of the regression rate by the oxidizer mass flux is not sufficient for the definition of a correlation in the motor of larger size where the effects of the recirculating bubble are not negligible; as anticipated in Section 2.3.1, a dependence linked to the motor dimensions, and in particular to the grain diameter, should be introduced.

Figure 4.18 represents the computed regression rates of the tests S as function of the averaged oxidizer mass flux at each time step. As shown, a possible correlation of the regression rate data obtained only with the smaller engine is that as power function of the oxidizer mass flux, expressed as:

$$\dot{r} = a G_{ox}^n \quad a = 0.132; \quad n = 0.648 \quad (4.4)$$

The following correlation was compared with that shown in Ref. [74], which was obtained by a series of experimental tests in a range of oxidizer mass flux between 50 and 100 kg/m²s. Indeed, the two trendlines agree right in this range and the deviation increases where experimental data are not available. Hence, Eq.(4.4) aims to be an extension to high G_{ox} of the correlation derived on experimental data.

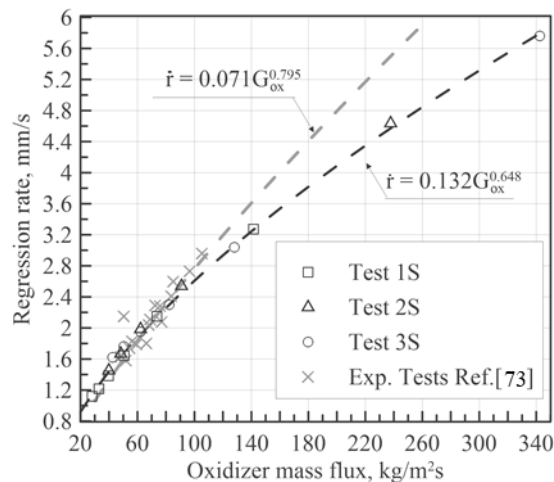


Figure 4.18 A representation of the regression rate as function of the oxidizer mass flux computed at each time-step in tests S and a comparison of the obtained trendline (black line) with that derived experimentally in Ref. [74]

(grey line).

On the other hand, the authors tried to find a suitable correlation of the kind $\dot{r} = a G_{ox}^n$, but the computed regression rates do not appear aligned along a unique trendline as shown in Figure 4.19a. This confirms what expressed above. The regression rate cannot refer only to the oxidizer mass flux in the tests in which the effect of the recirculating bubble is not negligible. A new correlation similar to Eq. was found:

$$\dot{r} = a G_{ox}^n A_r^m \quad a = 0.198; \quad n = 0.678; \quad m = 0.279 \quad (4.5)$$

Figure 4.19b depicts the good fitting of \dot{r}/A_r^m with the oxidizer mass flux by using Eq.(4.5), which is in line with the experimental findings shown in Section 2.3.1.

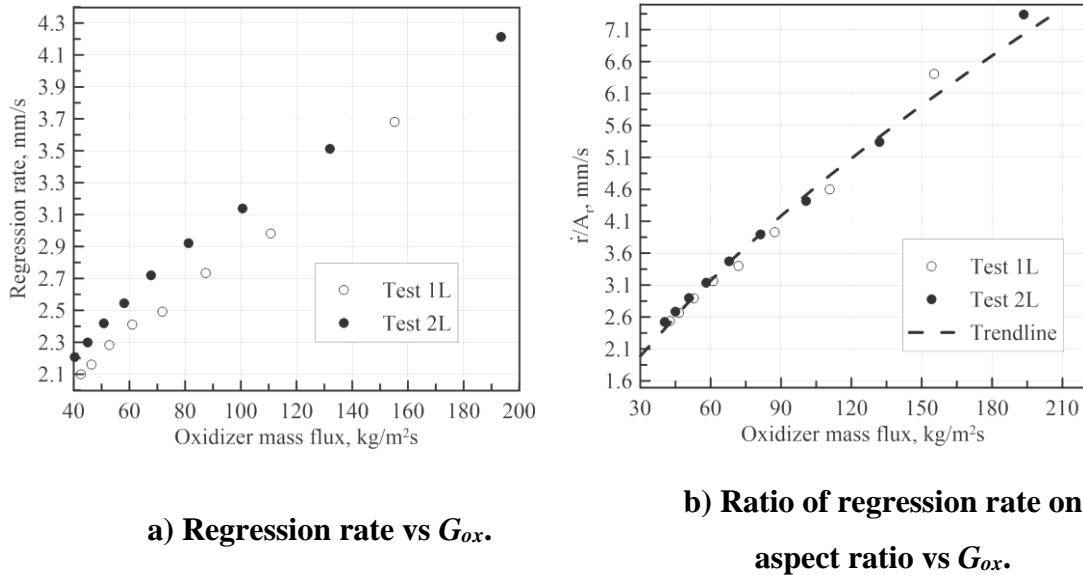


Figure 4.19 A representation of the regression rate as function of the oxidizer mass flux computed at each time-step in tests L.

4.2.5 Models Uncertainty Discussion

In this section, all the aspects concerning the models uncertainty are discussed. As mentioned before, the overall numerical model mainly consists of three different tools, which are the CFD, GSI and entrainment models. Regarding the CFD apparatus, the uncertainty related to the mesh-grid has been discussed in section 4.1.2. The uncertainty relative to the GSI model lies in the choice of the paraffin properties

constants, which are resumed in Table 3.3. However, the constants have been taken from the most trustworthy and accepted scientific work in the literature [81], therefore it is expected that the highest source of uncertainty is due to the entrainment modelling by experimental correlations. In particular, the old entrainment model described by Eq.(3.28) adequately works by the correct estimation of the constant, a_{ent} , which has been tuned in Ref. [43] and parametrically studied by varying it of $\pm 50\%$ with a corresponding regression rate variation of $\pm 10\%$. Finally, although the constants employed in Eq.(3.48) are the same of the reference paper [97], an uncertainty analysis has been carried out by varying the number by which the Reynolds number is divided. A higher sensitivity is expected, because the entrained fraction has an exponential dependence. However, a variation of $\pm 10\%$ leads to a variation of $\pm 10\%$ of the regression rate, which is retained acceptable.

CHAPTER 5. NUMERICAL MODEL FOR COMBUSTION INSTABILITY AND RESULTS

5.1 Longitudinal modes in variable cross section ducts and density

A suitable numerical model is required to recognize the exhibited frequencies detected in the tests shown in section 2.3.3. The problem of acoustic modes evaluation in a hybrid rocket engine can be schematized in a series of ducts with different cross sectional area and gas properties. Indeed, the solution of the acoustic field in a complex geometry as that shown in Figure 5.1 can be simplified in the solution of the waves' equation in each duct with appropriate boundary conditions at the interfaces (see Figure 5.2). All the ducts included between the choked Venturi and the nozzle are considered in the analysis. For the sake of simplicity, because the injector length is only 0.5% of the oxidizer feed pipe, it is neglected by the analysis.

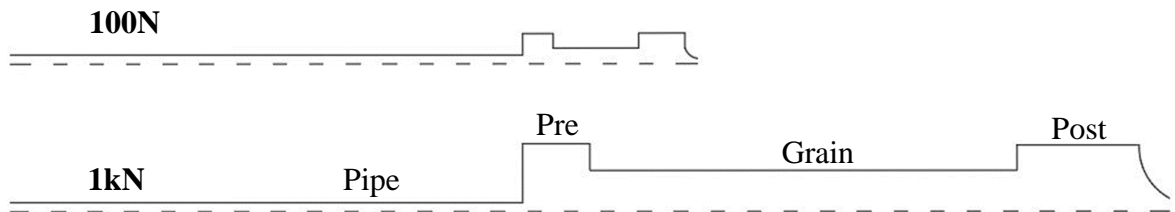


Figure 5.1 Schematic of the 100N and 1kN motors.

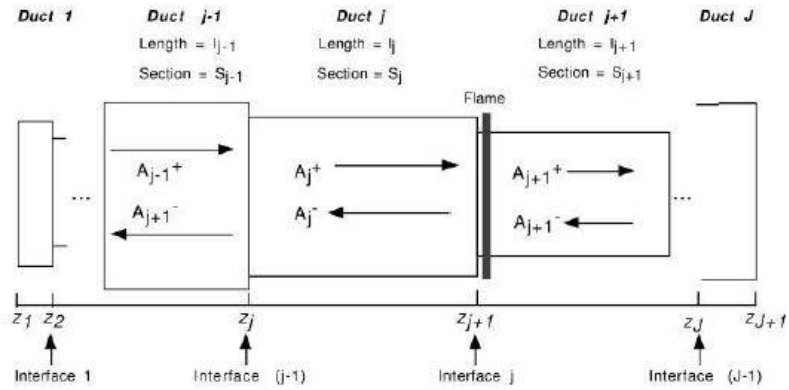


Figure 5.2 Cross sectional jumps with variations of the gas properties [101].

In this work, the method reported in Ref. [101] has been followed and briefly described here. A common strategy to obtain the linearized form of the momentum and energy equations in terms of pressure and velocity fluctuations is to express the dependent variables as the sum of steady and time dependent component:

$$u(x, t) = \bar{u}(x) + u'(x, t), \quad p = \bar{p}(x) + p'(x, t), \quad \rho(x, t) = \bar{\rho}(x) + \rho'(x, t) \quad (5.1)$$

Substituting Eq. (5.1) in Euler's equations and assuming that the fluctuations are small than the steady component, the acoustic equations into a series of ducts of length, l_j , and variable cross section, S_j are defined by:

$$\begin{aligned} \bar{\rho} \frac{\partial u'}{\partial t} + \frac{\partial p'}{\partial x} &= 0 \\ \frac{1}{\bar{\rho} \bar{c}^2} \frac{\partial p'}{\partial t} + \frac{1}{S} \frac{\partial (Su)'}{\partial x} &= 0 \end{aligned} \quad (5.2)$$

The analytical solution of Eq. (5.2) in a single duct with constant gas properties is given by:

$$\begin{aligned} p' &= \hat{p}(x) e^{-i\omega t} = A^+ e^{i(kx - \omega t)} + A^- e^{i(-kx - \omega t)} \\ u' &= \hat{u}(x) e^{-i\omega t} = \frac{1}{\bar{\rho} \bar{c}} (A^+ e^{i(kz - \omega t)} - A^- e^{i(-kz - \omega t)}) \\ A^+ &= A e^{i\vartheta}, \quad A^- = A e^{-i\vartheta} \end{aligned} \quad (5.3)$$

Where A and ϑ are the wave amplitude and phase, respectively. The spatial dependence is completely separated from the temporal one. Assuming known the

average flow-field, the problem reduces to finding the unknowns ω, A^+, A^- . The problem is closed by imposing suitable conditions at both the boundaries.

The analysis is further complicated if a series of variable cross section ducts with different gas densities and speed of sound are considered in the analysis. Referring to Figure 5.2, integrating Eq. (5.2) at the interface j from x_{j+1}^- to x_{j+1}^+ , we obtain the jump conditions:

$$\begin{aligned} [p']_{x_{j+1}^-}^{x_{j+1}^+} &= 0, & p'(x_j) &= p'(x_{j+1}) \\ [Su']_{x_{j+1}^-}^{x_{j+1}^+} &= 0, & S(x_j)u'(x_j) &= S(x_{j+1})u'(x_{j+1}) \end{aligned} \quad (5.4)$$

The second of Eq. (5.4) is somewhat surprising since one would expect the acoustic mass flow rate to be conserved and not the volume flow rate. This is due to the assumption of negligible convected terms compared to unsteady terms: the mean flow is neglected and the interface acts like a non-permeable membrane which transmits volume changes but not mass.

Substituting Eq. (5.3) in Eq. (5.4), the equation which links the wave amplitudes in section $j + 1$ to the amplitudes in section j is obtained:

$$\begin{pmatrix} A_{j+1}^+ \\ A_{j+1}^- \end{pmatrix} = T_j \begin{pmatrix} A_j^+ \\ A_j^- \end{pmatrix} \quad (5.5)$$

Where T_j is called transfer matrix and it is defined as:

$$T_j = \frac{1}{2} \begin{bmatrix} e^{ik_j l_j} (1 + \Gamma_j) & e^{-ik_j l_j} (1 - \Gamma_j) \\ e^{ik_j l_j} (1 - \Gamma_j) & e^{-ik_j l_j} (1 + \Gamma_j) \end{bmatrix} \quad (5.6)$$

$$\Gamma_j = \frac{\bar{\rho}_{j+1} \bar{c}_{j+1} S_j}{\bar{\rho}_j \bar{c}_j S_{j+1}} \quad (5.7)$$

Chaining all the transfer matrix from the duct 1 to the J , the global matrix, G , is given by:

$$\begin{pmatrix} A_J^+ \\ A_J^- \end{pmatrix} = G \begin{pmatrix} A_1^+ \\ A_1^- \end{pmatrix}, \quad G = T_1 T_2 \dots T_J \quad (5.8)$$

The problem is closed by imposing reflection coefficient, R , at both the boundaries:

$$\frac{A_1^+}{A_1^-} = R_1, \quad \frac{A_J^+}{A_J^-} = e^{2ik_J l_J} R_J, \quad (5.9)$$

Where $R = -1$ means $p' = 0$, which is appropriate for ducts terminating in large vessels, while $R = 1$ means $u' = 0$ suitable for a rigid wall. In our case, two choked orifices are physically present at the boundaries. A shock-wave takes place after the sonic Venturi, which makes difficult the definition of a physical boundary condition at the feed-head. Anyway, for the sake of simplicity, zero acoustic velocity is simply enforced at $x=0$. At the motor end, the admittance of the nozzle, Y_n , is assigned assuming that the short, choked nozzle approximation holds true, for which

$$Y_n = \frac{\bar{\rho}_n \bar{c}_n^2}{\gamma_n \bar{p}} \bar{M}_n \frac{\gamma_n - 1}{2} \quad (5.10)$$

where M_n is the Mach number at the nozzle inlet section. Then, the boundary reflection coefficient can be computed by:

$$R = \frac{1 + Y}{1 - Y} \quad (5.11)$$

Eq. (5.8) and Eq. (5.9) represents a linear system of J -equations with non-trivial solution only for a limited set of natural frequencies, which satisfy the following equation:

$$R_J = \frac{G_{11}R_1 + G_{12}}{G_{21}R_1 + G_{22}} e^{2ik_J l_J} \quad (5.12)$$

Since the problem is linear, only scaled wave amplitudes can be obtained. Finally, the following computational procedure is pursued:

1. Specify the left and the right reflection coefficient, R_1 and R_J .
2. Evaluate the transfer matrix of each duct and the global matrix.
3. Compute ω by solving Eq. (5.12).

4. Find the scaled wave amplitudes for each duct, A_j^+/A_1^+ and A_j^-/A_1^- .
5. Evaluate p' and u' along the spatial coordinate by Eq. (5.3).

5.1.1 Simplification of the double duct

The assumption of considering the engine as a chamber with constant cross-sectional area (see Figure 5.3) introduces a drastic simplification, which allows to recast Eq. (5.12) in:

$$\cos(k_1 l_1) \cos(k_2 l_2) + \Gamma_1 \sin(k_1 l_1) \sin(k_2 l_2) = 0 \quad (5.13)$$

In this particular case, Γ_1 is also called coupling parameter because the eigenmodes of the feed-line and the motor are decoupled for $\Gamma_1 \ll 1$; in fact, Eq.(5.13) reduces to $\cos(k_1 l_1) \cos(k_2 l_2) = 0$, which leads to two distinct solution families for the oxidizer tube and the chamber. Assuming the gas density proportional to the temperature and the speed of sound to the square root, the coupling parameter defined by Eq. (5.7) can be simplified in:

$$\Gamma_1 \cong \frac{S_1}{S_2} \left(\frac{T_2}{T_1} \right)^{\frac{1}{2}} \quad (5.14)$$

Therefore, the propellant combustion enhances the acoustic coupling between the supply line and the chamber, while a low coupling parameter can be obtained by increasing the pre-chamber inner diameter. Anticipating the next sections, this parameter encourages the exhibition of the acoustic chamber modes, which provide the combustion stability.

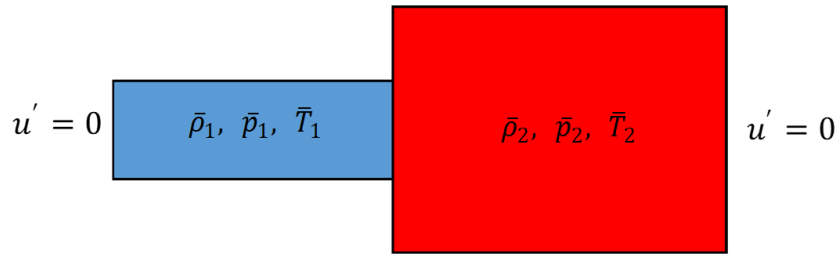


Figure 5.3 Double duct problem schematic.

5.1.2 Analytical mode results

The evaluation of the coupling degree between the pipe and the motor is mandatory to give a right interpretation of the numerical results. Figure 5.4 shows the coupling parameter, Γ_1 , in both configurations for several mixture ratios in pre-chamber. The coupling parameter of the 1kN motor is around four times lower than the 100N, which suggests that the combustion chamber is acoustically more isolated from the feed pipe. In addition, test L-P employs a showerhead injector, which is known to be an effective isolating system [51]. For this reason, it is expected that test L-P promotes the 1L chamber mode, while test S-P the 1L pipe mode.

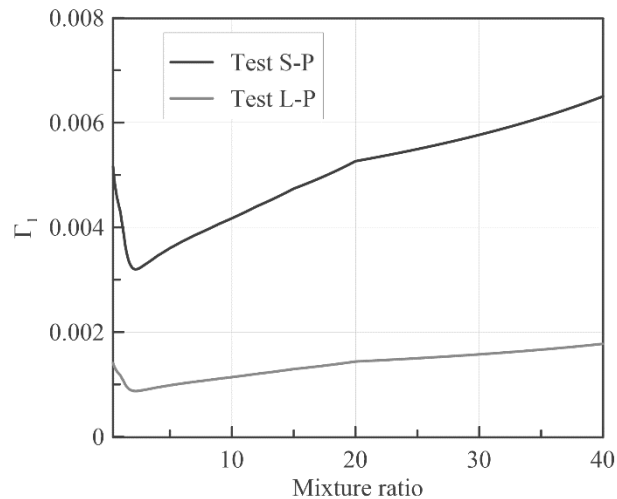


Figure 5.4 Coupling parameter vs prechamber mixture ratio.

The method described above is used for the computation of the modal frequency, ω_r , by considering different gas properties in each duct. The gas properties are known in the feed duct (oxygen at 300K) and the motor, in which it is assumed that the

properties corresponding to the overall OF are achieved throughout. The gas properties are resumed in Table 5.1.

Table 5.1 Gas properties 100N and 1kN motor.

Configuratio n	Element	Static temperature, K	Densit y, kg/m ³	Gas constant, J/kg K	Sonic velocity, m/s	Specific heat ratio, –
100N	Feed-line	300	11.54	259.8	330.4	1.4
	Motor	2685	0.68	463.9	1231	1.22
1kN	Feed-line	300	34.64	259.8	330.4	1.4
	Motor	1750	2.18	544.5	1115	1.31

Table 5.2 displays a good agreement between the computed frequencies and the experimental ones. Note that a complex acoustic system as that shown in Figure 5.1 is characterized by infinite acoustic modes, which can be associated with the feed pipe, the motor or a mix and each mode can promote or discourage combustion instability. For this reason, the root finding of Eq.(5.12) has to be driven by suitable initial guess to obtain significant results, which could be, for instance, the exhibited experimental frequencies.

Table 5.2 Experimental vs numerical frequencies.

	Experimental	Numerical
Test S-P	280	222
	560	598
Test L-P	755	825
	1377	1377

Table 5.3 lists the computed numerical frequencies of the first acoustic mode of the feed pipe, the small and large motor by considering each element independently. Comparing these frequencies to that shown in Table 5.2, it can be noticed that the frequency at 825 Hz is associated with the 1L motor mode, while all the other frequencies are related to the feed pipe modes.

Table 5.3 Acoustic frequencies of the feed pipe, 100N and 1kN motors.

Mode	Feed pipe, Hz	Motor S-P, Hz	Motor L-P, Hz
1	386	3060	825

This is further supported by Figure 5.5, which depicts the acoustic modes of the frequencies listed in Table 5.2. A marked pressure antinode takes place at the injection interface in the mode at 825 Hz, in which the first chamber mode can be easily recognized. The presence of the motor is not relevant in all the other frequencies.

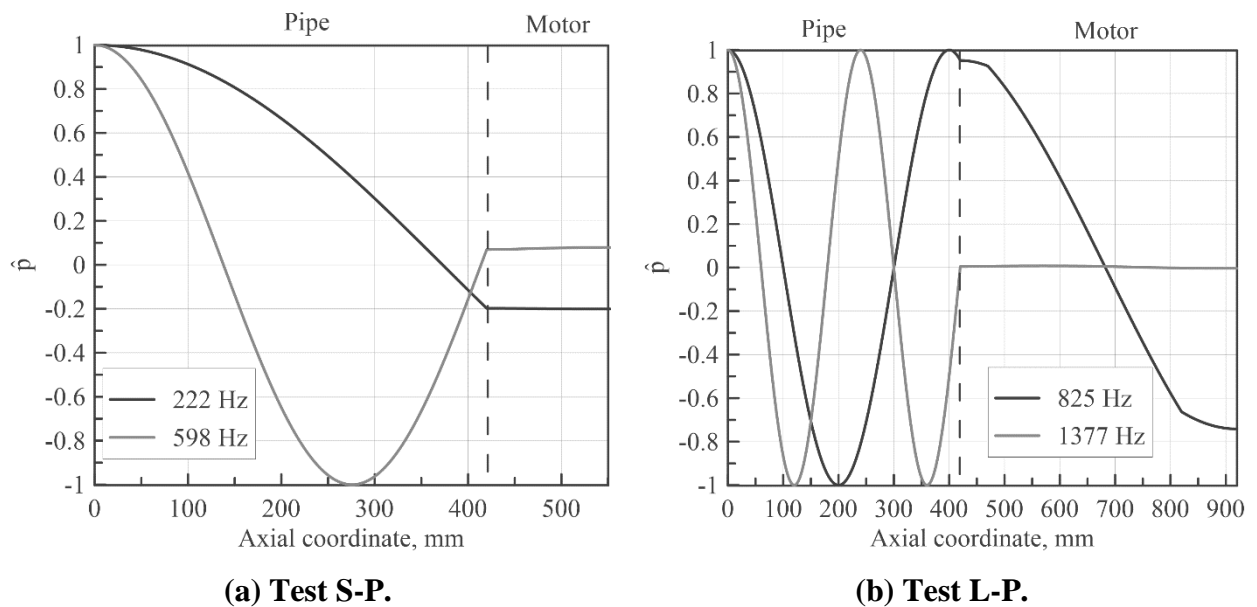


Figure 5.5 Spatial pressure fluctuations along the axial coordinate.

The deviations between the numerical and experimental frequencies in the 100N motor can be related to the uncertainty on the left boundary condition, R_1 . Indeed, after the choked Venturi a shockwave takes place to adapt the supersonic flow to the downstream conditions. This physical condition is far from a simple boundary wall ($R_1=1$), in which zero velocity fluctuation is imposed. It is expected that this mostly affects the evaluation of the acoustic frequencies in the test S-P, where the tube mode is predominant. Indeed, Figure 5.6 shows that a reflection coefficient equal to 0.7

matches the experimental frequency in the smaller motor, while no relevant effects are shown on the first acoustic mode of the 1kN motor.

On the other hand, the mixture ratio variation along the motor of course affects the frequency computation in the larger motor, in which the chamber modes are significant. Numerical simulations of the 1kN motor performed in Ref. [66] have shown that a large recirculating zone takes place in the pre-chamber driving backward a significant amount of fuel. The mixture ratio increases continuously from the pre-chamber reaching the overall OF in post-chamber. A parametric study on the effect of the mixture ratio variations on the acoustic frequencies has been carried out. Once imposed the OF in pre-chamber and the overall OF in post-chamber, speed of sound and density are assigned at the motor ends; for the sake of simplicity, the average speed of sound is computed as $\sqrt{(c_{pre}^2 + c_{post}^2)/2}$, while, the density is obtained as arithmetical average $(\rho_{pre} + \rho_{post})/2$. Figure 5.6 represents the frequency associated with the first longitudinal mode (1L) versus the OF_{pre} in both the tests. As expected, the 1L frequency remains approximately constant at 222 Hz, while it changes from 867 to 635 Hz in the 1kN motor; in particular, an OF_{pre} equal to 12 provides a good agreement between the numerical and experimental frequency. This value has been assigned in pre-chamber in the following analysis.

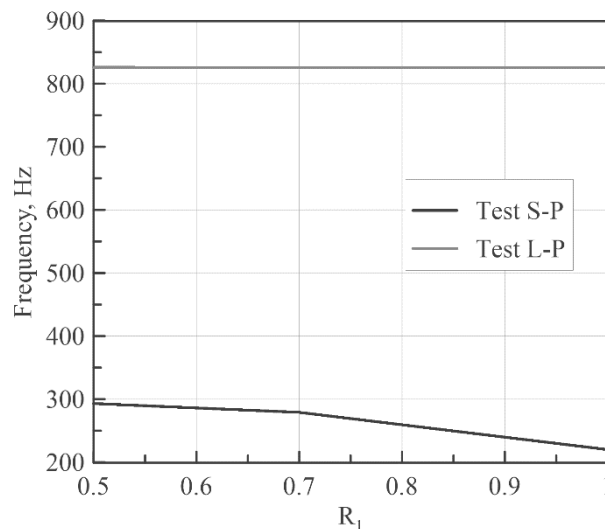


Figure 5.6 First mode vs. R₁.

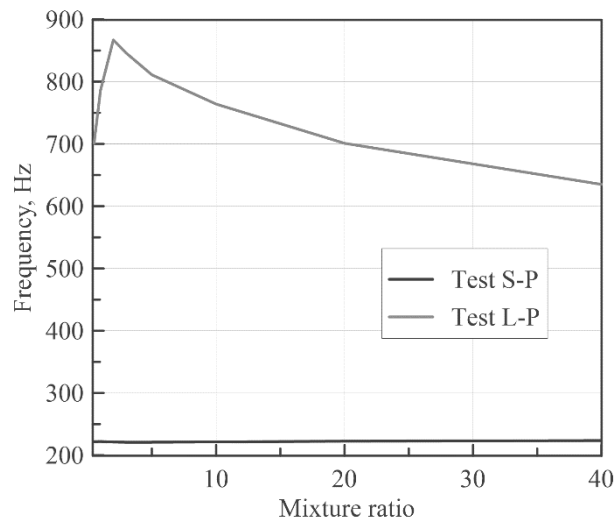


Figure 5.7 First mode vs. mixture ratio.

5.2 A comprehensive one-dimensional model for acoustic stability analysis

As shown in the previous section, acoustic modes have been promoted during the firing tests, which yields to the need of modeling the acoustic field to predict adequately the occurring combustion instability by including a delay to the fuel mass flow rate addition. This is also highlighted by the analysis carried out in Appendix B, in which a 0D transient model was developed for an isolated feed system with a simple filling/emptying dynamic for the combustion chamber and the feed pipe. After having derived the transfer function between the chamber pressure and the oxidizer mass flow rate imposed by the choked Venturi, no positive poles have been found by setting the operating condition of the test S-P suggesting that the acoustic field plays an important role in triggering combustion instability.

The governing equations for the one-dimensional longitudinal waves are obtained starting from the conservation equations of mass, momentum, and energy generally written for a cylindrical chamber with mass injection from the walls. The same approach can be applied as well to describe the acoustic fluctuations in the prechamber, aft-mixing chamber and the feed pipe by specializing the several terms appearing in the derived equations.

The overall combustion process is assumed to occur only in the fuel grain port (i.e. the effect of combustion of unburned vaporized fuel and oxidizer in the postchamber is taken into account as if arising in the grain port), and it is modeled with the heating of the mixture resulting from the mixing of the main gas stream with the mass entering from the side wall with larger energy. A perfect gas ($p = \rho \mathcal{R}T$) with variable molecular weight and specific heats along the grain, but constant with time, is assumed.

A procedure equal to the one in Ref. [58] is followed; the energy equation is here critically revised and the tricky assumption of a mean specific heat [59] is released; furthermore, it is formulated in terms of total enthalpy, instead of internal energy, generalizing the treatment in Ref. [102] to the case of unsteady motion.

Consider the flow in the fuel port between two sections an infinitesimal distance dx apart (Figure 5.8). Port section is assumed constant.

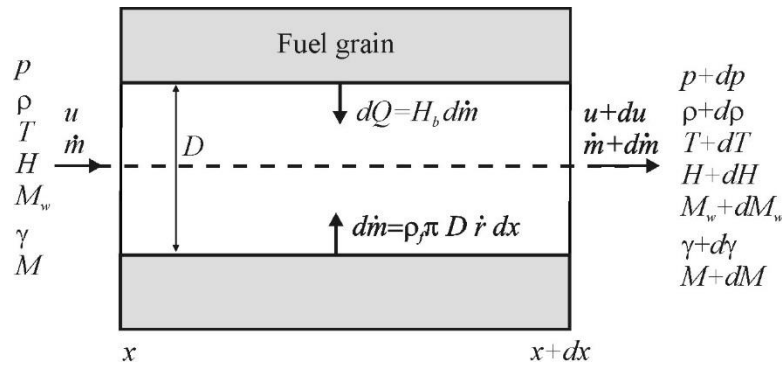


Figure 5.8 Flow schematic and control volume.

In this element of port length, fuel is injected into the main stream with the mass flow rate of $d\dot{m} = \rho_f \dot{r} \pi D dx$, where \dot{r} is the regression rate that is assumed constant all over the grain axis, so that the fuel mass flow rate per unit length, $\dot{m}_{fx} = d\dot{m}/dx$, is constant as well. Energy dQ is added to the main stream through the injection of fuel pyrolysis products and their combustion with the oxidizer: $dQ = H_b d\dot{m}$, where $H_b = h_b + u_f^2/2$ is the specific total enthalpy of the pyrolysis products, sum of the specific sensible enthalpy, h_b , here also referred to as fuel heating value, and the specific kinetic energy, $u_f^2/2$. Note that, for the continuity at the fuel surface, $u_f =$

$\rho_f \dot{r} / \rho$. As the regression rate is about 1 mm/s, and h_b is on the order of 10^7 J/kg, the ratio $u_f^2 / 2h_b$ results on the order of 10^{-8} and one can consider $H_b \cong h_b$. Wall friction is ignored because it can be neglected with respect to the driving factor related to the mass injection and gas heating [102]; however, concentrated total pressure losses in the sudden contraction at the grain inlet and at the sudden expansion between the grain exit and the postchamber are considered.

Because the gas density is much lower than the solid fuel density ($1 - \rho / \rho_f \cong 1$) the effects of the port diameter time-variation are negligible, thus the following equations of mass, momentum and energy balances, respectively, are obtained:

$$\frac{\partial \rho}{\partial t} + \frac{\partial \rho u}{\partial x} = \frac{\dot{m}_{fx}}{A} \quad (5.15)$$

$$\rho \frac{\partial u}{\partial t} + \rho u \frac{\partial u}{\partial x} + \frac{\partial p}{\partial x} = -u \frac{\dot{m}_{fx}}{A} \quad (5.16)$$

$$\rho \frac{\partial H}{\partial t} + \rho u \frac{\partial H}{\partial x} = \frac{\partial p}{\partial t} + \frac{\dot{m}_{fx}}{A} (H_b - H) \quad (5.17)$$

In Eq.(5.17) $H = h + u^2/2$ is the total enthalpy of the mixture (main stream plus added mass stream), and it is assumed that the injected gas from the wall mixes completely with the main stream and both exit from the control volume with the same velocity and same enthalpy per unit mass [103].

Constant enthalpy of the injected gas along the grain length is also assumed. Hence, at the steady state, the energy equation reduces to an ordinary differential equation that can be analytically integrated, between the grain inlet and the generic section, to yield:

$$H(x) = H_b - (H_b - H_1) \frac{\dot{m}_{ox}}{\dot{m}(x)} \quad (5.18)$$

where H_1 is the total enthalpy of the gas at the grain inlet section (see Figure 5.9), which expresses the fact that, for the injection of gas from the wall with the enthalpy $H_b > H_1$, the total enthalpy monotonically increases down the port.

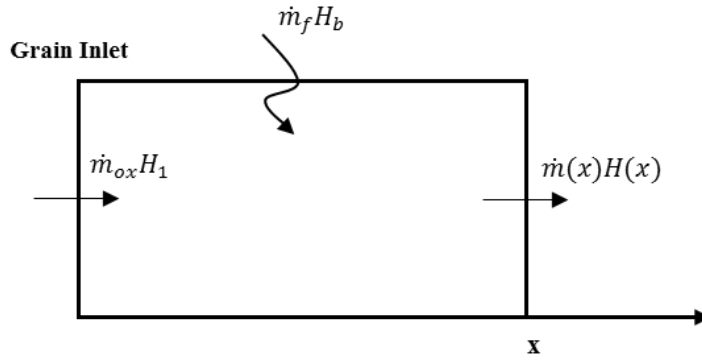


Figure 5.9 Sketch of a control volume inside the grain port.

Eq. (5.17) is elaborated to show specific enthalpy, pressure and density. By substituting the velocity time derivative from the momentum into the energy equation, one obtains:

$$\rho \frac{Dh}{Dt} - \frac{Dp}{Dt} = \frac{\dot{m}_{fx}}{A} (H_b - H + u^2) \quad (5.19)$$

where the symbol D indicates the substantial derivative that is used for the sake of compactness. For the perfect gas assumption, and the hypothesis that the two streams mix with each other and achieve the same sensible enthalpy per unit mass, the mixture enthalpy total differential is calculated as:

$$dh = c_p dT = c_p d\left(\frac{p}{\rho \mathcal{R}}\right) = c_p T \left(\frac{dp}{p} - \frac{d\rho}{\rho} - \frac{d\mathcal{R}}{\mathcal{R}}\right) \quad (5.20)$$

which, plugged into Eq. (5.19), yields

$$\frac{Dp}{Dt} - \frac{\gamma p}{\rho} \frac{D\rho}{Dt} = (\gamma - 1) \frac{\dot{m}_{fx}}{A} (H_b - H + u^2) + \gamma \frac{pu}{\mathcal{R}} \frac{d\mathcal{R}}{dx} \quad (5.21)$$

in which $\gamma = c_p/c_v$ is the specific heat ratio; the specific heat at constant pressure is evaluated as $c_p = \mathcal{R} + c_v = [\gamma/(\gamma - 1)]\mathcal{R}$, and the total derivative sign has been used for the gas constant for it is independent of time. Extrapolating the density derivative from the continuity equation (Eq. (5.15)), the following form of the energy equation is derived [57]:

$$\frac{\partial p}{\partial t} + u \frac{\partial p}{\partial x} + \gamma p \frac{\partial u}{\partial x} = (\gamma - 1) \frac{\dot{m}_{fx}}{A} \left(H_b - h + \frac{u^2}{2} + \frac{\gamma}{\gamma - 1} \frac{p}{\rho} \right) + \gamma \frac{up}{\mathcal{R}} \frac{d\mathcal{R}}{dx} \quad (5.22)$$

Expressing each of the dependent variables and the fuel mass flow rate as the sum of steady and time dependent (see Eq. (5.19)) and substituting these expressions into the conservation equations, Eq. (5.15), Eq. (5.16) and Eq. (5.22), yield to two systems of equations: one for the average quantities (here indicated with the overbar), and the other for pressure and velocity fluctuations (indicated with prime). The assumption of extremely low fluctuations leads to the independence of the mean flow from the acoustic field; whereas, the acoustic is affected by the mean flow. For this reason, it is mandatory the computation of the mean flow before the solution of the acoustic field.

5.2.1 The mean flow

The general form of the governing equations for the average flow quantities is:

$$\begin{aligned} \bar{\rho} \frac{d\bar{u}}{dx} + \bar{u} \frac{d\bar{\rho}}{dx} &= \frac{\bar{m}_{fx}}{A} \\ \bar{\rho} \bar{u} \frac{d\bar{u}}{dx} + \frac{d\bar{p}}{dx} &= -\bar{u} \frac{\bar{m}_{fx}}{A} \\ \bar{u} \frac{d\bar{p}}{dx} + \gamma \bar{p} \frac{d\bar{u}}{dx} &= (\gamma - 1) \frac{\bar{m}_{fx}}{A} \left(H_b - \bar{H} + \bar{u}^2 + \frac{\gamma}{\gamma - 1} \frac{\bar{p}}{\bar{\rho}} \right) + \gamma \frac{\bar{p}\bar{u}}{R} \frac{dR}{dx} \end{aligned} \quad (5.23)$$

where the three unknowns are pressure, density and velocity. Eq.(5.23) have to be solved from the choked Venturi to the nozzle throat. They are extremely simplified in the feed-line, the prechamber and the postchamber, in which the right hand side (RHS) is imposed equal to zero; whereas, the complete form has to be taken into account to solve the mean flow along the grain. The total enthalpy, \bar{H} , is only function of the mass flow rate ratio $\dot{m}_{ox}/\dot{m}(x)$ and it is computed by Eq.(5.18). For the solution of the average quantities, once the oxidizer mass flow rate, the regression rate and the port diameter are assigned, the overall motor mixture ratio, OF , is defined, which is assumed to be achieved in aft-chamber. The average OF in pre-chamber depends on

flow-field generated by the injection arrangement, which is actually tricky to estimate. Anyway, as shown in the results, the choice of the OF in pre-chamber has a negligible effect on the 100N motor than the 1kN, for which a tuning on experimental data is required. Chemical equilibrium is assumed and the gas mixture properties are determined with the CEA code at the average pressure in pre and post chamber; thus, gas temperature, molecular weight and the specific heat ratio are known at grain ends.

Special functional forms are adopted to describe the variation of the speed of sound, molecular weight and of the specific heat ratio along the combustion chamber axis. Squared speed of sound is assumed linear with the axial coordinate, that is

$$\theta = \theta_0 + \theta_x x \quad (5.24)$$

where $q = \bar{a}^2 = \gamma \bar{p}/\bar{\rho}$ (here the isentropic coefficient has been supposed coincident with the ratio of specific heats), $\theta_x = \frac{d\theta}{dx} = (\theta_n - \theta_0)/L$ is the slope coefficient and L represents the grain length. Whereas, for both the specific heat ratio and molecular weight power functions are assumed

$$\begin{aligned} \gamma &= \gamma_0 \left(1 + \frac{\theta_x}{\theta_0} x\right)^{\alpha_\gamma} \\ M_w &= M_{w0} \left(1 + \frac{\theta_x}{\theta_0} x\right)^{\alpha_w} \end{aligned} \quad (5.25)$$

in which $\alpha_w = \ln(M_{wn}/M_{w0})/\ln(\theta_n/\theta_0)$ and $\alpha_\gamma = \ln(\gamma_n/\gamma_0)/\ln(\theta_n/\theta_0)$. Note that, for the temperature increase and molecular weight decrease occurring in the combustion process, θ_x is positive, and both α_γ and α_w are negative. The value of H_b is determined a posteriori to reach the expected temperature at the grain exit.

The following jump conditions are used to solve the interfaces inside the motor:

$$\begin{aligned} \bar{m}(x_j) &= \bar{\rho}(x_{j+})\bar{u}(x_{j+})A_{j+} = \bar{\rho}(x_{j-})\bar{u}(x_{j-})A_{j-} \\ \bar{p}(x_{j+}) &= \bar{p}(x_{j-}) + \frac{\bar{m}(x_j)}{2} \left(\frac{\bar{u}(x_{j-})}{A_{j-}} - \frac{\bar{u}(x_{j+})}{A_{j+}} \right) \end{aligned} \quad (5.26)$$

The first represents the continuity of the mass flow rate, while the second of the total pressure. The subscript $j+$ refers to the quantity just downstream of the section j , whereas $j-$ to the quantity upstream of the same section. Indicating with AR_j the area ratio at the discontinuity j ($AR_j = A_{j+}/A_{j-}$), at the sharp-edged contraction between the prechamber and the grain inlet the total pressure drop is given by $\Delta\bar{P}_2 =$

$\frac{1}{2}\bar{\rho}_2\bar{u}_2^2(1/\mu - 1)^2(1/AR_2^2)$, where μ is the contraction coefficient ($\mu = 0.63 + 0.37 AR_2^3$) [104], and the one at the exit from the grain is $\Delta\bar{P}_3 = \frac{1}{2}\bar{\rho}_3\bar{u}_3^2(1 - 1/AR_3)^2$ [105]. For the resolution of the injector interface, the continuity of the mass flow rate is maintained, while the experimental pressure drop is imposed so that $\bar{p}(x_2) = \bar{p}(x_1) - \Delta\bar{P}_1$.

5.2.2 Acoustic field equations

The acoustic field equations can be easily derived by substituting Eq.(5.1) in Eq.(5.15) to Eq.(5.17) and subtracting Eq.(5.23) (the mean flow). The following momentum and energy fluctuation equations are obtained:

$$\begin{aligned}
 \bar{\rho} \frac{\partial u'}{\partial t} + \frac{\partial p'}{\partial x} + \rho' \bar{u} \frac{d\bar{u}}{dx} + \bar{\rho} \frac{\partial}{\partial x} (\bar{u}u') + \frac{\bar{m}'_{fx}}{A} u' + \frac{\dot{m}'_{fx}}{A} \bar{u} &= 0 \\
 \frac{\partial p'}{\partial t} + \bar{u} \frac{\partial p'}{\partial x} + \gamma \bar{p} \frac{\partial u'}{\partial x} + u' \frac{d\bar{p}}{dx} + \gamma p' \frac{d\bar{u}}{dx} - (\gamma - 1) \frac{\bar{m}'_{fx}}{A} \bar{u}u' & \quad (5.2) \\
 = (\gamma - 1) \frac{\dot{m}'_{fx}}{A} \left(H_b - \bar{H} + \bar{u}^2 + \frac{\gamma}{\gamma - 1} \frac{\bar{p}}{\bar{\rho}} \right) + \gamma \frac{\bar{u}p' + \bar{p}u'}{\mathcal{R}} \frac{d\mathcal{R}}{dx} & \quad 7)
 \end{aligned}$$

In Eq. (5.27), use of the relationship $h' = h - \bar{h} = c_p(T - \bar{T}) = \frac{\gamma}{\gamma - 1} \bar{p}/\bar{\rho} (p'/\bar{p} - \rho'/\bar{\rho})$ has been made. The number of acoustic equations is reduced to two, because the density fluctuation is related to the isentropic pressure fluctuation by $\rho' = p'/\bar{c}^2$. The same separation of variables applied at Eq.(5.3) is used for the fuel mass flow rate per unit length:

$$\dot{m}'_{fx}(x, t) = \hat{m}'_{fx} e^{-i\omega t} \quad (5.28)$$

With the aim of study the system stability varying the fuel delay, a delay, τ , is imposed to the added fuel mass flow rate:

$$\dot{m}'_{fx}(x, t - \tau_v) = \hat{m}'_{fx} e^{-i\omega(t - \tau)} \quad (5.29)$$

By substituting this relationship in Eq. (5.29), the following equations for the variables $\hat{p}(x)$ and $\hat{u}(x)$ are obtained:

$$\begin{aligned}
 \bar{\rho}\bar{u}\frac{d\hat{u}}{dx} + \frac{d\hat{p}}{dx} + \left(\bar{\rho}\frac{d\bar{u}}{dx} + \frac{\bar{m}_{fx}}{A} + i\Omega\bar{\rho}\right)\hat{u} + \frac{\bar{u}}{\bar{a}^2}\frac{d\bar{u}}{dx}\hat{p} &= -\bar{u}\frac{\hat{m}_{fx}e^{i\omega\tau}}{A} \\
 \gamma\bar{p}\frac{d\hat{u}}{dx} + \bar{u}\frac{d\hat{p}}{dx} + \left(\frac{d\bar{p}}{dx} - \frac{\gamma-1}{A}\bar{m}_{fx}\bar{u} - \bar{p}\frac{\gamma}{\mathcal{R}}\frac{d\mathcal{R}}{dx}\right)\hat{u} & \\
 + \left(\gamma\frac{d\bar{u}}{dx} + i\Omega - \bar{u}\frac{\gamma}{\mathcal{R}}\frac{d\mathcal{R}}{dx}\right)\hat{p} & \\
 = (\gamma-1)\frac{\hat{m}_{fx}e^{i\omega\tau}}{A}\left(H_b - \bar{H} + \bar{u}^2 + \frac{\gamma}{\gamma-1}\frac{\bar{p}}{\bar{\rho}}\right) &
 \end{aligned} \tag{5.30}$$

A linearization of \dot{m}_{fx} is required to obtain \hat{m}_{fx} , because of the exponential dependence of the regression rate on the oxidizer mass flux ($\dot{r} = aG_{ox}^n$, $a=0.132$, $n=0.65$ from Ref. [66]). Therefore, the fuel mass flow rate per unit length can be expressed as:

$$\dot{m}_{fx} = \bar{m}_{fx}(\bar{G}_{ox}) + \left.\frac{d\dot{m}_{fx}}{dG_{ox}}\right|_{\bar{G}_{ox}} G_{ox}' \tag{5.31}$$

In Eq. (5.31), the mean \dot{m}_{fx} has been divided from the corresponding fluctuation, which is linked to G_{ox}' . The fluctuation of the oxidizer mass flux can be expressed as function of the local velocity and density fluctuations:

$$G_{ox}' = \bar{\rho}u' + \rho'\bar{u} \tag{5.32}$$

Therefore, the spatial fluctuation of the fuel mass flow rate per unit length is given by:

$$\hat{m}_{fx} = \left.\frac{d\dot{m}_{fx}}{dG_{ox}}\right|_{\bar{G}_{ox}} \hat{G}_{ox} = \bar{m}_{fx}\frac{n}{\bar{G}_{ox}}\left(\bar{\rho}\hat{u} + \frac{\hat{p}\bar{u}}{\bar{c}^2}\right) \tag{5.33}$$

In Eq.(5.33) average quantities appear; thus, once the latter have been assigned, the determination of the longitudinal modes characteristics proceeds in two stages: first the solution of the average field is sought, from which all the average quantities and their space derivatives appearing in Eq.(5.30) are known; after that, one can step into

the solution of Eq.(5.30) itself. For the sake of simplicity, at the j -th cross-section discontinuities the simplified jump conditions represented by Eq.(5.4) have been employed. Two boundary conditions are required for the problem closure. At the tube head, zero acoustic velocity is enforced, while Eq.(5.10) is imposed at the nozzle throat.

The values of the modal frequency, that is $\text{Re}(\omega)$, and the growth constant of each mode, that is $\text{Im}(\omega)$, as well as the modes' shape can be found by solving the corresponding boundary value problem. Note that, as the equations are linear, the magnitude of the acoustic pressure at the motor head end does not affect the results and it can be assigned arbitrarily.

5.2.3 Mean flow results

As an example of the average solution results, static temperature, static pressure, gas velocity and the main gas properties are shown in Figure 5.10 versus the distance from the motor head end. Calculations have been carried out with paraffin burned with oxygen in the test S-P and L-P operating conditions.

Note that at the injection head, to account for the transport of hot gas from the fuel port back to the pre-chamber, which causes an increase of temperature with respect to the incoming oxygen, an equivalent mixture ratio, $OF_{\text{pre}} = 12$, has been assigned which provides a good match between numerical and experimental acoustic frequency in the larger motor.

Integration of Eq. (5.23) has been carried out with the fourth-order Runge-Kutta adaptive-step method; in the above listed conditions, using the Newton-Raphson technique, the calculated fuel heating value is $H_b = 7.01 \times 10^6$ J/kg in the test S-P, while 1.89×10^6 J/kg in the test L-P.

As shown in Figure 5.10, the pressure is approximately constant along x in the test S-P, because the conical axial injector involves a negligible pressure drop. On the other hand, a pressure drop of around 6.4 atm is displayed in the test L-P in which a showerhead injector is employed. All the thermodynamic quantities are continuous in the motor and discontinuous at the injection, where the mixture properties steeply change due to fuels/oxidizer mixing in pre-chamber. The velocity jumps at each cross

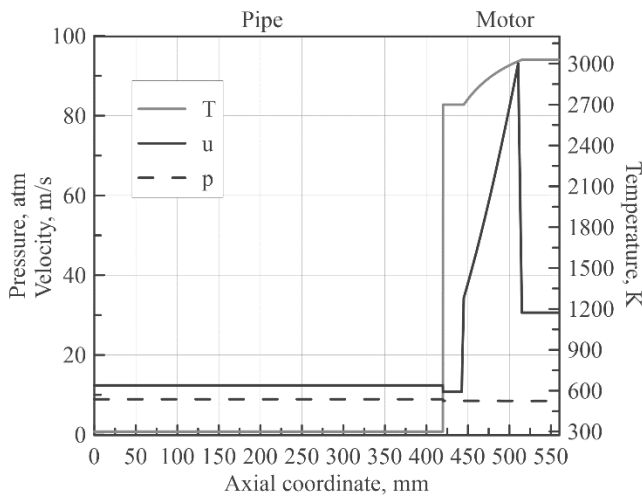
section discontinuity for the one-dimensional nature of the model and it increases along the grain because of the fuel mass flow rate adduction from the grain wall. The fuel port outlet Mach number is calculated to be 0.024 for the test S-P and 0.019 for the test L-P, which leads to a right reflection coefficient approximately equal to 1.

Assuming that the liquid paraffin droplets move along the motor with the gas velocity, the residence time can be computed by:

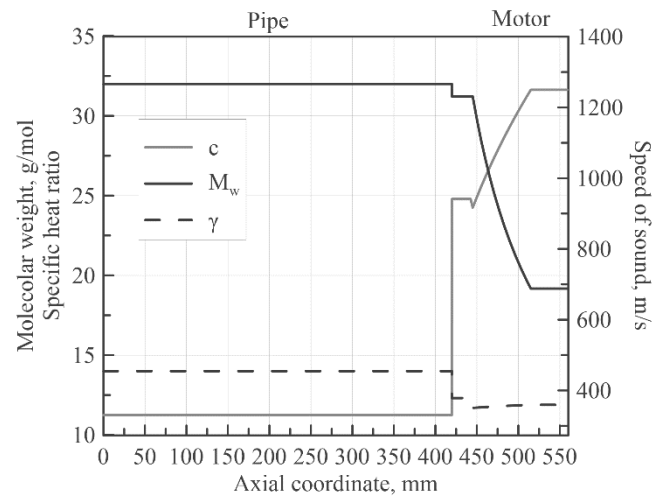
$$t_r = \int_{x_{in,grain}}^{x_{fin,post}} \frac{1}{u(x)} dx \quad (5.34)$$

Where $x_{in,grain}$ and $x_{fin,post}$ correspond to the initial and final axial coordinate of the fuel grain and post-chamber, respectively. The residence time has been estimated equal to 0.00269s for test S-P and 0.0157s for test L-P.

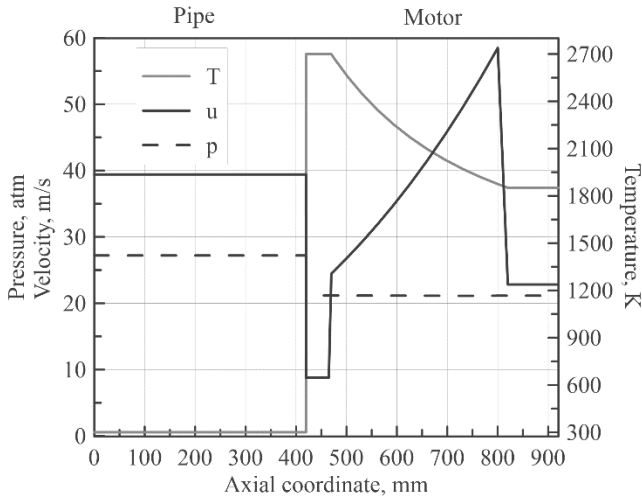
The obtained results are involved in the resolution of the acoustic field, which, as shown previously, is affected by the average flow-field.



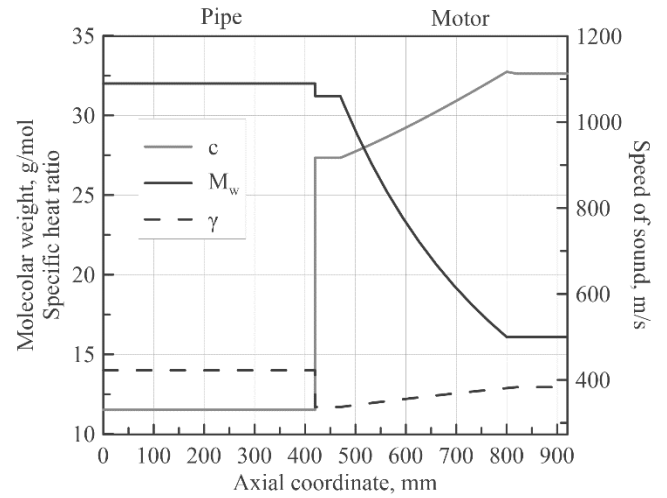
(a) Test S-P: pressure, velocity and temperature.



(b) Test S-P: specific heat, molecular weight and speed of sound.



(c) Test L-P: pressure, velocity and temperature.



(d) Test L-P: specific heat, molecular weight and speed of sound.

Figure 5.10 Mean flow results along axial coordinate.

5.2.4 Stability results

In this section, the stability results are shown to support experimental findings shown in Section 2.3.3. Note that the mathematical convention considered in the equations requires that the system instability is defined by the positive sign of the imaginary part of ω , which is also called growth rate. All the quantities have been represented as function of the delay time adimensionalized by the residence, $\bar{\tau} = \tau/\tau_r$. For $\bar{\tau}$ greater than 1, the results are meaningless, because the liquid droplets leave the motor unburnt. Figure 5.11 shows the computed growth rates and frequencies calculated by solving Eq.(5.30) at the operating conditions of test S-P and L-P. Figure 5.11a shows the 1L frequencies of both tests. The frequencies are near to those obtained by using the analytical model, which means that the fuel adduction and the relative delays do not influence the system frequencies. Figure 5.11b depicts the growth rates, ω_i , corresponding to the modal frequencies exhibited in the tests. All the modes associated with the pipe show positive and negative growth rates by varying the fuel mass flow rate delay. This means that the system encourages combustion instability for infinite values of τ . Note that for $\tau = 0s$, all modes are stable, which means that a flash release of fuel mass flow rate ensures combustion instability, which is in line with test S-H. On the other hand, the mode associated with the 1kN

combustion chamber at 750 Hz is absolutely stable. This is consistent with the experimental observations and with that mentioned before: the acoustic decoupling achieved in the 1kN motor due to the high pre-chamber to pipe cross section ratio and the injection system promotes the emerging of the chamber acoustic modes, which are stable as shown in Figure 5.11b. On the other hand, the acoustic coupling between feed line and combustion chamber in the 100N motor involves the exhibition of the pipe modes, which encourage combustion instability. Because the RHS of Eq.(5.30) consists of sinusoidal functions, all the results oscillate around an average value.

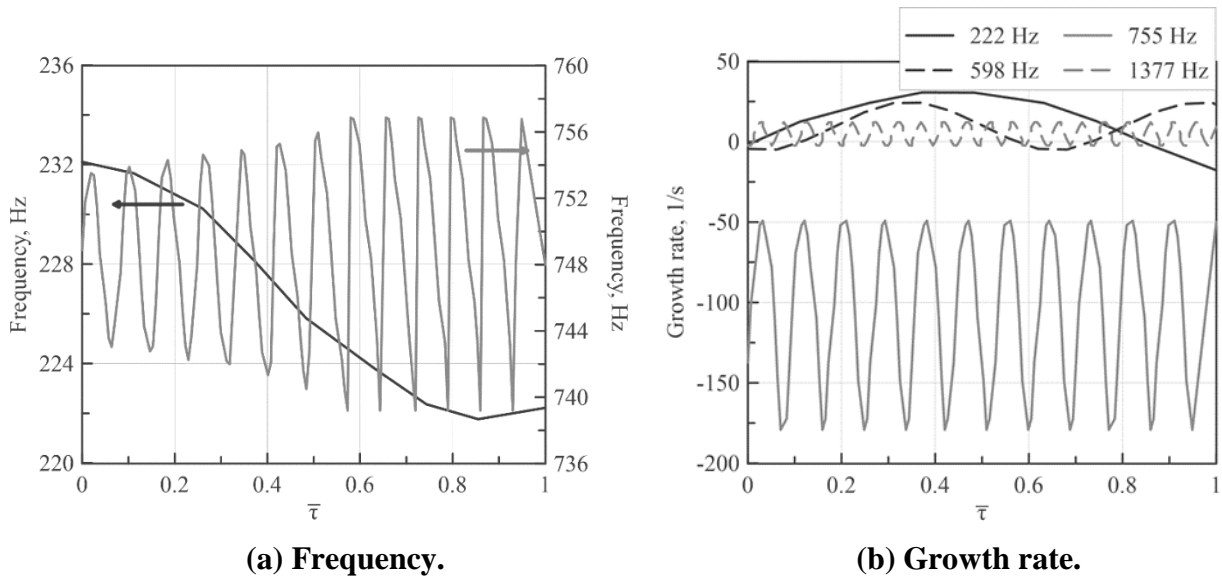
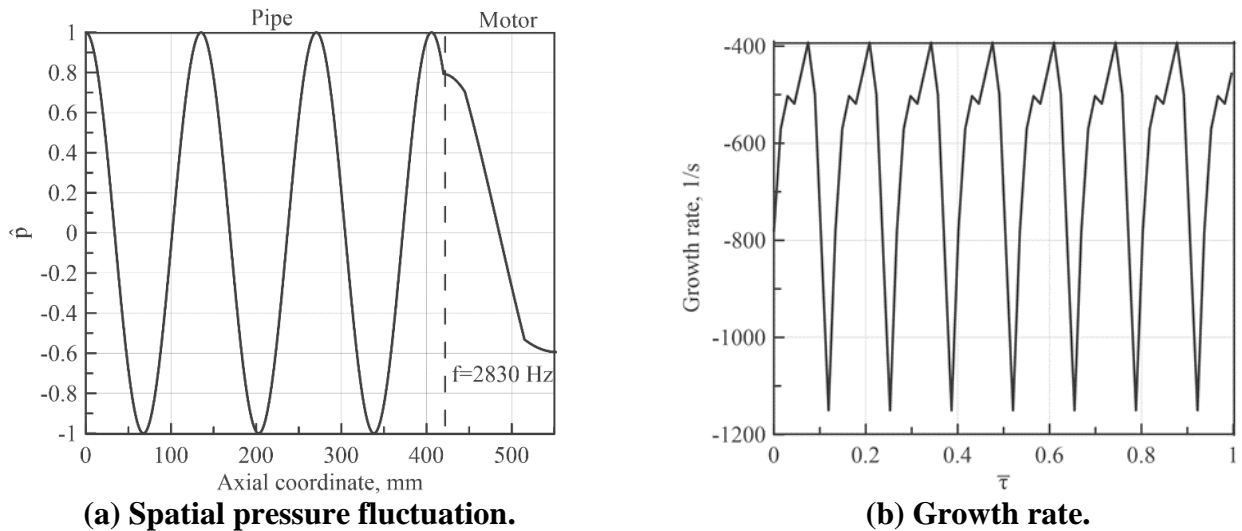


Figure 5.11 Stability results vs adimensionalized mass flow rate delay (Test S-P black line, test L-P grey line).

To value the influence of the cold pipe in the acoustic system, a new stability analysis has been performed with the 100N configuration starting from an initial frequency value near to the 1L chamber mode. The obtained mode frequency is around

2830 Hz, whose mode is represented in Figure 5.12a. The corresponding acoustic mode is stable as displayed in Figure 5.12b.



(a) Spatial pressure fluctuation.

(b) Growth rate.

Figure 5.12 1L 100N chamber mode stability results.

Finally, a parametric study has been performed in order to understand the effect of the grain length on the system stability. As shown in Figure 5.13, the increasing of the grain length from 70mm to 220mm involves a larger stability region. Indeed, the percentage of the stable time-lags increases from 18% to 47% in the longer configuration.

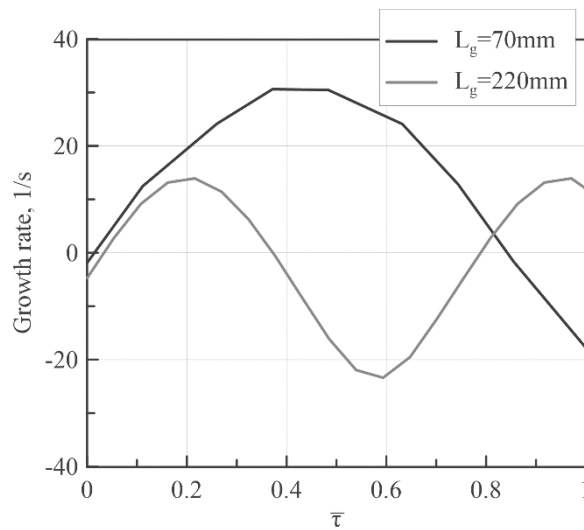


Figure 5.13 Grain length parametric study.

CONCLUSIONS

The present dissertation dealt with two of the major issue in hybrid rocket propulsion technology development: first the definition of proper numerical models for the engine internal ballistics simulation, with the capability to predict the fuel consumption behaviour, and second a comprehensive study of combustion instability occurring when burning liquefying fuels.

For the first task, a CFD approach to the simulation of internal ballistics of hybrid rocket engines has been presented. The RANS equations, with two additional transport equations for the average mixture fraction and its variance combined to the probability density function combustion model and thermochemical equilibrium were solved. With respect to previous developments carried out at University of Naples, two new sub-model suitable to describe the interaction between the gaseous flow and the grain surface for the prediction of the fuel regression rate were defined and implemented. The new gas/surface interaction model stems from the formulation of a fuel in-depth pyrolysis model coupled with the resolution of the thermo-fluid-dynamic field in the rocket combustion chamber, which allows for the characterization of the unstable liquid layer formed on top of the fuel surface. The new entrainment model was defined in order to take into account the key dependences of the entrainment, which can be resumed in the definition of a suitable liquid Reynolds number. A number of experimental test cases, consisting in the combustion of gaseous oxygen with different fuel grains in laboratory scale hybrid rockets, were numerically reproduced in order to assess the validation of the numerical models. A good agreement between the calculated regression rate and the measured data is obtained and compared with the previous model. The new numerical model has been assessed on the small and large motor configuration during the burning time by suitable reconstruction techniques. The new numerical model has shown the capability to capture the effect of the recirculating zone. Indeed, the error computed by the new model is limited to the 4% for both the motor configurations, while it increases up to 27% for the larger configuration by using the old model.

For the second task, dedicated experimental tests have been performed to investigate the mechanism triggering combustion instability in liquefying fuels. The campaign suggested that paraffin fuels introduce an additional delay to the motor dynamic which can couple with the acoustic system. The exhibited frequencies have been studied by a simplified analytical model for acoustic systems characterized by ducts with different cross sectional area and gas properties with zero velocity gas flow. The model has proved the capability to rebuild the experimental frequencies, which are characteristic of the acoustic system. In particular, when the smaller engine is employed, the feed pipe acoustic modes included between the choked Venturi and the injection plate dominates on the combustion chamber. Indeed, the geometrical configuration of the pre-chamber and the injection system do not provide an effective acoustic isolation of the combustion chamber from the feed line as in the larger motor, in which the chamber acoustic modes are promoted. Then, a stability analysis was carried out by varying the fuel mass flow rate time-lag. The results show that the characteristic modes of the feed pipe encourage the combustion instability, while the motor modes are unconditionally stable. Therefore, the acoustic coupling of the combustion chamber from the feed line can be discouraged by increasing the geometrical area jump at the corresponding interface. Finally, for time-lag equal to 0, the acoustic stability recurs, which is in line with the test burning HDPE, where basically the fuel mass flow rate is promptly released.

APPENDIX A: SIMPLIFIED SOLUTION OF THE LIQUID LAYER EQUATIONS

A simplified solution to the liquid layer equations is addressed in this Appendix. In the limit of infinite activation energy, melting and liquid-phase reactions are confined in a thin layer beneath the regressing surface so that material is lost only from the surface region; this simplification leads to a so-called ablation model [92] for which the liquid mass fraction is constant throughout the liquid layer and it is discontinuous at the surface. Assuming that the fuel thermophysical properties both in the liquid and solid state are constant with temperature, the first of Eqs. (3.40) reduces to the following equation for temperature, whereas the second is trivial and states that the liquid mass fraction is identically equal to 1:

$$\frac{d^2T}{d\xi^2} + \frac{1}{\delta_l} \frac{dT}{d\xi} = 0 \quad (\text{A1})$$

in which $\delta_l = \alpha_l \rho_l / \rho_s \dot{r}$ is the liquid-layer characteristic thermal thickness. The solution of this equation is:

$$T(\xi) = C_1 + C_2 e^{-\frac{\xi}{\delta_l}} = 0 \quad (\text{A2})$$

The two constants of integration C_1 and C_2 can be determined through the following boundary conditions:

$$\xi = 0 \quad \dot{q}_w = -\lambda_l \left(\frac{dT}{d\xi} \right)_w + \rho_s \dot{r}_v \Delta h_p \quad (\text{A3})$$

$$\xi = h \quad T = T_m \quad (\text{A4})$$

The first boundary condition is set at the regressing surface, and imposes that the heat exchanged to the wall is equal to the heat lost by conduction into the fuel and the heat required for the liquid pyrolysis; in fact, with the assumption that the latter process is concentrated at the surface, the relevant energy term, removed from the inner of the liquid layer, has to be accounted for in the wall energy balance. Upon substitution, the two constants are eliminated, and Eq. (A2) reads

$$T(\xi) = T_m + \frac{\delta_l}{\lambda_l} (\dot{q}_w - \rho_s \dot{r}_v \Delta h_p) \left(e^{-\frac{\xi}{\delta_l}} - e^{-\frac{h}{\delta_l}} \right) \quad (\text{A5})$$

in which the liquid layer thickness h is not known, and can be calculated through the energy balance at the solid/liquid interface:

$$-\lambda_l \left(\frac{\partial T}{\partial \xi} \right)_{\xi=h} = \frac{\lambda_s}{\delta_s} (T_m - T_a) + \rho_s L_m \dot{r} \quad (\text{A6})$$

from which one obtains:

$$e^{-\frac{h}{\delta_l}} = \frac{\frac{\lambda_s}{\delta_s} (T_m - T_a) + \rho_s L_m \dot{r}}{\dot{q}_w - \rho_s \dot{r}_v \Delta h_p} \quad (\text{A7})$$

By rearranging Eq. (A5) by means of Eq. (A7), the expression for the heat flux to the wall in Eq.(3.27) is eventually recovered; furthermore, using Eq. (3.27), it is immediate to show that the following relationship for the thickness of the liquid layer holds:

$$e^{-\frac{h}{\delta_l}} = \frac{c_s (T_m - T_a) + L_m}{c_l (T_w - T_m) + c_s (T_m - T_a) + L_m} \quad (\text{A8})$$

Note that, as discussed in the text, this equation predicts that, as $\dot{r} \rightarrow 0$ (i.e. $\delta_l \rightarrow \infty$), the term on the right-hand side being a finite quantity, h tends to infinity. Moreover, in case $h = 0$, there is no vaporization, and Eq. (A8) accordingly implies that the surface temperature is equal to the melting temperature.

With the substitution of Eq. (A7) into Eq. (A5), and resorting, for the sake of brevity, to the positions: $\varphi = e^{-\frac{h}{\delta_l}}$, $\Delta T = T_w - T_m$, $\varepsilon = \xi/\delta_l$, the temperature profile assumes the linear form:

$$T(\varepsilon) = T_w \left(1 - \frac{\Delta T}{T_w} \frac{1 - e^{-\varepsilon}}{1 - \varphi} \right) \cong T_w \left(1 - \frac{\Delta T}{T_w} \frac{\varepsilon}{1 - \varphi} \right) \quad (\text{A9})$$

in which the exponential expansion up to the first-order term around $\epsilon \ll 1$ has been used. Hence, the activation energy factor E_a/RT can be approximated as follows:

$$\frac{E_a}{RT} = \frac{E_a}{RT_w} \frac{1}{1 - \frac{\Delta T}{T_w} \frac{\epsilon}{1 - \varphi}} \cong \frac{E_a}{RT_w} \left(1 + \frac{\Delta T}{T_w} \frac{\epsilon}{1 - \varphi} \right) \quad (\text{A10})$$

and the integral in Eq.(3.34) can be analytically calculated considering that $Y = 1$:

$$\rho_s \dot{r}_v = \int_0^h \rho_l B_p e^{-E_a/RT} Y d\xi = \rho_l B_p e^{-\frac{E_a}{RT_w} \delta_l} \int_0^{\frac{h}{\delta_l}} e^{-\frac{E_a \Delta T}{RT_w T_w} \frac{\epsilon}{1 - \varphi}} d\epsilon \quad (\text{A11})$$

whereby, as $e^{-\frac{E_a \Delta T}{RT_w T_w} \frac{h/\delta_l}{1 - \varphi}} \cong e^{-\frac{E_a \Delta T}{RT_w T_w}} \ll 1$, by means of Eq. (A1288), one finally obtains the following approximate expression for the vaporization component of regression rate:

$$\dot{r}_v = \delta_l B_p \frac{e^{-\frac{E_a}{RT_w}} \cdot c_l T_w}{\frac{E_a}{RT_w} [c_l (T_w - T_m) + c_s (T_m - T_a) + L_m]} \quad (\text{A12})$$

If $h = h_{max}$, regression rate is entirely due to vaporization, and Eq. (A12) becomes:

$$\dot{r}_v = \dot{r} = \sqrt{\alpha_l \frac{\rho_l}{\rho_s} B_p \frac{c_l T_w}{\frac{E_a}{RT_w} [c_l (T_w - T_m) + c_s (T_m - T_a) + L_m]}} e^{-\frac{E_a}{2RT_w}} \quad (\text{A13})$$

Note that, in case of a classical polymer, which does not melt on the surface while undergoes pyrolysis, this equation reduces to:

$$\dot{r} = \sqrt{\frac{\alpha_s B_p}{\frac{E_a}{RT_w} \left[1 - \frac{T_a}{T_w} + \frac{\Delta h_p}{c_s T_w} \right]}} e^{-\frac{E_a}{2RT_w}} \quad (\text{A14})$$

which is practically coincident with the result of the complete calculations given by Lengelle [106].

Eq. (A13) predicts that the vaporization regression rate obtained at the maximum liquid layer thickness varies with temperature essentially following a negative

exponential: $\dot{r}_v \propto e^{-\frac{E_a}{2RT_w}}$; in fact, the data in Figure 3.4a have been redrawn in Figure A 1 as a function of the parameter $E_a/2RT_w$ in logarithmic scale. The numerical data points are best fit with an exponential coefficient of -0.962 and a constant pre-exponential factor yielding a squared correlation index of 0.999 , thus demonstrating the validity of Eq. (A13) in which the temperature dependence of the pre-exponential factor is dropped.

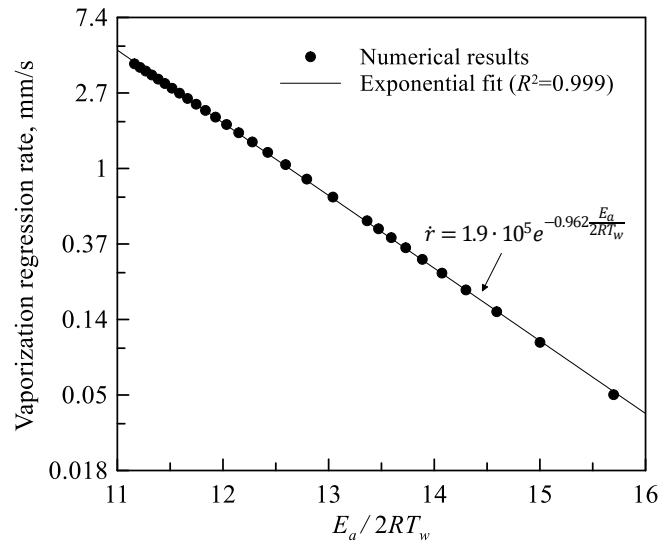


Figure A 1 Vaporization regression rate as a function of surface temperature.

APPENDIX B: ZERO DIMENSIONAL ACOUSTIC MODEL

It can be recognized that the dynamic system mainly consists of three elements, which are feed-pipe, injector and combustion chamber. Because the injector length is extremely short, the dynamic can be neglected. Therefore, at the steady-state the injected mass flow rate is given by:

$$\dot{m}_{inj} = c_d A_{inj} \sqrt{2 \frac{p_p}{R_{ox} T_{ox}} (p_p - p_c)} \quad (B1)$$

Note that gaseous oxidizer is injected, hence the density in the feed system is given by the ideal gas law. The transient models of the pipe and combustion chamber are respectively described by:

$$\frac{V_p}{(RT)_{ox}} \frac{dp_p}{dt} = \dot{m}_{ox} - \dot{m}_{inj} \quad (B2)$$

$$\frac{V_c}{(RT)_{ave}} \frac{dp_c}{dt} = \dot{m}_{inj} + \dot{m}_f - \dot{m}_n \quad (B3)$$

Where \dot{m}_{ox} is the oxidizer mass flow rate imposed by the choked Venturi and \dot{m}_n is the exhausted mass flow rate by the nozzle defined as $\dot{m}_n = p_c A_t / (\eta c^*_{th})$, where η is the combustion efficiency. A combustion delay, τ , has been imposed to the fuel mass flow rate, \dot{m}_f , which can be written as:

$$\dot{m}_f = \rho_f a \left(\frac{4\dot{m}_{inj}(t - \tau)}{\pi D^2} \right)^n \pi D L \quad (B4)$$

Following the linearization and normalization of these dynamic equations for the pipe and chamber can be reduced to the following form:

$$R_p \frac{d\varphi_p}{d\hat{t}} = \frac{2 + \beta}{2} \Phi_{ox} - \frac{2 + \beta}{2\beta} (2\varphi_p - \varphi_c) + \frac{\varphi_p}{\beta} \quad (B5)$$

$$\frac{d\varphi_c}{d\hat{t}} = \theta_0 \left(\frac{2\varphi_p - \varphi_c}{\beta} - \frac{2}{\beta} \frac{\varphi_c}{2 + \beta} \right) \Big|_t + \theta_1 \left(\frac{2\varphi_p - \varphi_c}{\beta} - \frac{2}{\beta} \frac{\varphi_c}{2 + \beta} \right) \Big|_{t-\tau} - \varphi_c \quad (B6)$$

$$\varphi_c = \frac{p_c'}{\bar{p}_c}, \quad \varphi_p = \frac{p_p'}{\bar{p}_c}, \quad \Phi_{ox} = \frac{\dot{m}'_{ox}}{\bar{m}_{ox}}, \quad \beta = \frac{2(\bar{p}_p - \bar{p}_c)}{\bar{p}_c}, \quad (B7)$$

$$\theta_0 = \frac{OF}{OF + 1}, \quad \theta_1 = \frac{n}{OF + 1}$$

In which R_p is the ratio between the empty/filling characteristic time of the pipe, τ_p , and the combustion chamber, τ_c , which are defined as:

$$\tau_p = \frac{2V_p}{c_d A_{inj} \sqrt{R_{ox} T_{ox} \beta (2 + \beta)}} \quad (B8)$$

$$\tau_c = \frac{L^* \eta c^*_{th}}{R_c T_c} \quad (B9)$$

Where L^* is the chamber characteristic length, which is defined as V_c/A_t . The physical models for all key components have been established and the associated dynamic equations have been linearized and normalized. The linear Ordinary Differential Equations (ODE) given by Eq.(B5) and Eq.(B6) govern the overall response of a hybrid system including the dynamics of the feed system. Here our objective is to obtain a transfer function between the output parameter of interest (chamber pressure) and the relevant input parameter (oxidizer flow rate at pipe entrance). Note that once it is derived, the transfer function can be used to determine all critical system behavior including stability. The Laplace transformation technique is the natural method for the task in hand. The set of ODE's that represent the system dynamics reduces to the following set of algebraic equations in the Laplace space:

$$s\Pi_p = \left(\frac{2\Pi_c - 2\Pi_p + M_{ox}\beta^2 + \beta\Pi_c - 2\beta\Pi_c + 2M_{ox}\beta}{2\beta} \right) \frac{1}{R_p} \quad (B10)$$

$$(s + 1)\Pi_c = -\theta_0 \left(\frac{\Pi_c - 2\Pi_p}{\beta} + \frac{2}{\beta} \frac{\Pi_c}{2 + \beta} \right) - \theta_1 \left(\frac{\Pi_c - 2\Pi_p}{\beta} + \frac{2}{\beta} \frac{\Pi_c}{2 + \beta} \right) e^{-\tau s} \quad (B11)$$

Here s is the non-dimensional Laplace transform variable. We introduce the following Laplace transformation variables for the state variables:

$$\Pi_c \equiv L[\varphi_c], \quad \Pi_p \equiv L[\varphi_p], \quad M_{ox} \equiv L[\Phi_{ox}] \quad (B12)$$

Then, the transfer matrix, $T(s)$, can be computed as:

$$T(s) = \frac{\Pi_c}{M_{ox}} = \frac{(\theta_0 + \theta_1 e^{-\tau s})(\beta + 2)^2}{D(s)} \quad (\text{B13})$$

$$D(s) = \theta_0 + 3\beta + 2s + \beta^2 s + \beta^2 + \theta_1 e^{-\tau s} + 3\beta s + 4\theta_0 R_p s + \beta^2 R_p s^2 + 2\beta R_p s + 2\beta R_p s^2 + \beta^2 R_p s + 4\beta R_p s e^{-\tau s} + \theta_0 \beta R_p s + \theta_1 \beta R_p s e^{-\tau s} + 2 \quad (\text{B14})$$

In particular, positive poles (which are roots of $D(s)$ function) are shown by unstable systems, while negative poles by stable systems. No positive poles have been found by solving Eq.(B14) for the Test S-P. A complete numerical model is required for the system stability prediction, which also includes the pipe and chamber acoustics.

ACKNOWLEDGMENTS

The experimental activities and the firing tests carried out at the Aerospace Propulsion Laboratory located in the military airport “F. Baracca” of Grazzanise (CE) have been possible thanks to the cooperation agreement between the University of Naples “Federico II” and the Italian Air Force. Many activities reported above have been carried out thanks to the program HYPROB funded by the Italian National Aerospace Research Program (PRORA) and committed to the Italian Aerospace Research Centre (CIRA).

Firstly, I would like to express my gratitude to my supervisor Prof. Raffaele Savino for the support in my PhD activities, for giving me the chance to work on space propulsion: my work, my hobby and my passion.

I would like to thank Dr Carmine Carmicino, who is for me a good friend, who has always encouraged me to work hard and transferred me most of his background just for the pleasure of working together, increasing the quality of my research with his enviable passion and willingness to continuous improvement.

A special thank goes to Stefano, with whom I shared all my positive and negative experiences. I hope for a successful and happy future for both.

Thank you so much to Prof. Harunori Nagata and Dr. Landon Kamps, who welcomed and appreciated me from the first time. Awesome years are waiting for us.

I wish also to thank professors Angelo Liseno, Claudio Curcio and Amedeo Capozzoli, who taught me a lot.

Many thanks to my military friends Carlo, Salvatore and Mario for all the coffees, air conditioning and smiles they gave to me. Many thanks also to Mr Antonio Alfano, for his availability and infinite patience in all the manufacturing works I needed for my activities.

Last but not the least, I would like to thank my parents, my brother, all my family for their priceless, never-ending support, and all my friends for all the fun, the cheerful moments, the precious advice and encouragement they always gave to me. A particular

Acknowledgments

mention for Paola, who always supported me during these years, respected and believed in all my passion in my work. The next step is coming.

BIBLIOGRAPHY

- [1] D. Altman and R. Humble, "Hybrid Rocket Propulsion Systems," in *Space Propulsion Analysis and Design*, 1st ed., R. Humble, G. Henry and W. Larson, Eds., New York, McGraw-Hill, 1995, pp. 365-370.
- [2] D. Altman and A. Holzman, "Overview and History of Hybrid Rocket Propulsion," in *Fundamentals of Hybrid Rocket Combustion and Propulsion*, vol. 218, K. Kuo and M. Chiaverini, Eds., Progress in Astronautics and Aeronautics, AIAA, 2007, pp. 1-36.
- [3] C. Oikine, "New Perspectives for Hybrid Propulsion," in *42nd AIAA/ASME/SAE/ASEE Joint Propulsion Conference & Exhibit*, Sacramento, California, 2006.
- [4] J. Ronningen and J. Husdal, "Nammo Hybrid Rocket Propulsion TRL Improvement Program," in *48th AIAA/ASME/SAE/ASEE Joint Propulsion Conference & Exhibit*, Atlanta, Georgia, 2012.
- [5] L. Casalino and D. Pastrone, "Optimal Design of Hybrid Rocket Motors for a Microgravity Platform," *Journal of Propulsion and Power*, vol. 24, no. 3, pp. 491-498, 2008.
- [6] A. Chandler, B. Cantwell, G. Hubbard and A. Karabeyoglu, "A Two-Stage, Single Port Hybrid Propulsion System for a Mars Ascent Vehicle," in *46th AIAA/ASME/SAE/ASEE Joint Propulsion Conference & Exhibit*, Nashville, TN, 2010.
- [7] L. Casalino, F. Letizia and D. Pastrone, "Optimization of Hybrid Upper Stage Motor with Coupled Evolutionary/Indirect Procedure," *Journal of Propulsion and Power*, vol. 30, no. 5, pp. 1390-1398, 2014.
- [8] B. Cantwell, A. Karabeyoglu and D. Altman, "Recent Advances in Hybrid Propulsion," *International Journal of Energetic Materials and Chemical Propulsion*, vol. 9, no. 4, pp. 305-326, 2010.

- [9] G. Crouch, "The market for space tourism: early indications," *Journal of Travel Research*, vol. 40, no. 2, pp. 213-219, 2001.
- [10] D. Webber, "Space tourism: its history, future and importance," *Acta Astronautica*, vol. 92, pp. 138-143, 2013.
- [11] The Tauri Group, "Suborbital reusable vehicles: a 10-year forecast of market demand," Federal Aviation Administration (FAA) - Office of Commercial Space Transportation and Space, Washington, DC, 2012.
- [12] A. Snow, E. Buchen and J. Olds, "Global launch vehicle market assessment - A study of launch services for nano/microsatellites in 2013," SpaceWorks, Atlanta, GA, 1999.
- [13] S. Burke and E. Schumann, "Diffusion flames," *Industrial and Engineering Chemistry*, vol. 20, no. 10, pp. 998-1004, 1928.
- [14] L. J. Green, "Introductory considerations on hybrid rocket combustion," *Progress in Astronautics and Rocketry*, vol. 15, pp. 451-484, 1964.
- [15] T. Houser and M. Peck, "Research in hybrid combustion," *Progress in Astronautics and Rocketry*, vol. 15, pp. 559-581, 1964.
- [16] G. Marxman and M. Gilbert, "Turbulent boundary layer combustion in the hybrid rocket," *Symposium (International) on Combustion*, vol. 9, no. 1, pp. 371-383, 1963.
- [17] G. Marxmann, "Combustion in the turbulent boundary layer on a vaporizing surface," *Symposium (International) on Combustion*, vol. 10, no. 1, pp. 1337-1349, 1965.
- [18] C. Carmicino and A. Russo Sorge, "Role of injection in hybrid rockets regression rate behavior," *Journal of Propulsion and Power*, vol. 21, no. 4, pp. 606-612, 2005.
- [19] C. Carmicino and A. Russo Sorge, "Influence of a conical axial injector on hybrid rocket performance," *Journal of Propulsion and Power*, vol. 22, no. 5, pp. 984-995, 2006.

- [20] M. Motoe and T. Shimada, "Numerical simulation of combustive flows in a swirling-oxidizer-flow-type hybrid rocket," in *52nd Aerospace Sciences Meeting*, National Harbor, Maryland, 2014.
- [21] C. Kumar and A. Kumar, "A numerical study on the regression rate of hybrid rocket motors using a combination of enhancement techniques," in *48th AIAA/ASME/SAE/ASEE Joint Propulsion Conference & Exhibit*, Atlanta, Georgia, 2012.
- [22] C. Carmicino and A. Russo Sorge, "Experimental investigation into the effect of solid-fuel additives on hybrid rocket performance," *Journal of Propulsion and Power*, vol. 31, no. 2, pp. 699-713, 2015.
- [23] M. Karabeyoglu, B. Cantwell and D. Altman, "Development and testing of paraffin-based hybrid rocket fuels," in *37th Joint Propulsion Conference and Exhibit*, Salt Lake City, Utah, 2001.
- [24] M. Karabeyoglu, D. Altman and B. Cantwell, "Combustion of liquefying hybrid propellants: Part 1, general theory," *Journal of Propulsion and Power*, vol. 18, no. 3, pp. 610-620, 2002.
- [25] A. Mazzetti, L. Merotto and G. Pinarello, "Paraffin-based hybrid rocket engines applications: a review and a market perspective," *Acta Astronautica*, vol. 126, pp. 286-297, September-October 2016.
- [26] M. A. Karabeyoglu and B. J. Cantwell, "Combustion of liquefying hybrid propellants: part 2, stability of liquid films," *Journal of Propulsion and Power*, vol. 18, no. 3, pp. 621-630, 2002.
- [27] A. Petrarolo, M. Kobald and S. Schleichriem, "Understanding Kelvin-Helmholtz instability in paraffin-based hybrid rocket fuels," *Experiments in Fluids*, pp. 59-62, 2018.
- [28] A. A. Chandler, E. T. Jens, B. J. Cantwell and G. S. Hubbard, "Visualization of the liquid layer combustion of paraffin fuel for hybrid rocket applications," in *48th AIAA/ASME/SAE/ASEE Joint Propulsion Conference & Exhibit*, Atlanta, Georgia, 2012.

- [29] B. Cantwell, A. Karabeyoglu and D. Altman, "Recent advances in hybrid propulsion," *International Journal of Energetic Materials and Chemical Propulsion*, vol. 9, no. 4, pp. 305-326, 2010.
- [30] M. Kobald, C. Schmierer, H. Ciezki, S. Schlechtriem, E. Toson and L. De Luca, "Viscosity and regression rate of liquefying hybrid rocket fuels," *Journal of Propulsion and Power*, vol. 33, no. 5, pp. 1245-1251, 2017.
- [31] Y. Chen, T. Chou, B. Gu, J. Wu, B. Wu, Y. Lian and L. Yang, "Multiphysics simulations of rocket engine combustion," *Computers & Fluids*, vol. 45, no. 1, pp. 29-36, 2011.
- [32] A. Coronetti and W. Sirignano, "Numerical analysis of hybrid rocket combustion," *Journal of Propulsion and Power*, vol. 29, no. 2, pp. 371-384, 2013.
- [33] M. Lazzarin, F. Barato, A. Bettella and D. Pavarin, "Computational fluid dynamics simulation of regression rate in hybrid rockets," *Journal of Propulsion and Power*, vol. 29, no. 6, pp. 1445-1452, 2013.
- [34] D. Bianchi and F. Nasuti, "Numerical analysis of nozzle material thermochemical erosion in hybrid rocket engines," *Journal of Propulsion and Power*, vol. 29, no. 3, pp. 547-558, 2013.
- [35] G. Leccese, D. Bianchi and F. Nasuti, "Simulation of hybrid rocket flowfields including modeling of fuel pyrolysis and thermal radiation," in *5th Space Propulsion Conference*, Rome, Italy, 2016.
- [36] V. Sankaran, "Computational fluid dynamic modeling of hybrid rocket flowfields," in *Fundamentals of hybrid rocket combustion and propulsion*, vol. 218, K. Kuo and M. Chiaverini, Eds., Progress in Astronautics and Aeronautics, AIAA, 2007, pp. 323-349.
- [37] D. Bianchi, F. Nasuti and C. Carmicino, "Hybrid rockets with axial injector: port diameter effect on fuel regression rate," *Journal of Propulsion and Power*, vol. 32, no. 4, pp. 984-996, 2016.
- [38] D. Bianchi, B. Betti, F. Nasuti and C. Carmicino, "Simulation of gaseous oxygen/hydroxyl-terminated polybutadiene hybrid rocket

- flowfields and comparison with experiments,” *Journal of Propulsion and Power*, vol. 31, no. 3, pp. 919-929, 2015.
- [39] M. Lazzarin, M. Faenza, F. Barato, N. Bellomo, A. Bettella and D. Pavarin, “Computational fluid dynamics simulation of hybrid rockets of different scales,” *Journal of Propulsion and Power*, vol. 31, no. 5, pp. 1458-1469, 2015.
- [40] G. Ranuzzi, D. Cardillo and M. Invigorito, “Numerical investigation of a N₂O-Paraffin hybrid rocket engine combusting flowfield,” in *6th European Conference for Aeronautics and Space Sciences (EUCASS)*, Krakow, Poland, 2015.
- [41] J. Y. Lestrade, J. Anthoine and G. Lavergne, “Liquefying fuel regression rate modeling in hybrid propulsion,” *Aerospace Science and Technology*, vol. 42, pp. 80-87, 2015.
- [42] G. Leccese, D. Bianchi, F. Nasuti, K. Stober, N. Pavan and B. Cantwell, “Simulations of paraffin-based hybrid rocket engines and comparison with experiments,” in *53rd AIAA/SAE/ASEE Joint Propulsion Conference*, Atlanta, Georgia, 2017.
- [43] G. Di Martino, S. Mungiguerra, C. Carmicino and R. Savino, “Computational Fluid-dynamic Modeling of the Internal Ballistics of Paraffin-fueled Hybrid Rocket,” *Journal of Propulsion and Power*, vol. 35, pp. 224-235, 2019.
- [44] G. Di Martino, C. Carmicino and R. Savino, “Transient Computational Thermofluid-Dynamic Simulation,” *Journal of Propulsion and Power*, vol. 33, pp. 1395-1409, December 2017.
- [45] F. E. C. Culick, “Combustion Instabilities in Propulsion Systems, Unsteady Motions in Combustion Chambers for Propulsion Systems,” in *Unsteady Combustion*, Dordrecht, Springer, pp. 173-241.
- [46] J. C. Oefelein and V. Yang, “Comprehensive Review of Liquid-Propellant Combustion Instabilities in F-1 Engines,” *Journal of Propulsion and Power*, vol. 9, no. 5, p. 657–677, 1993.

- [47] M. Rucker, "Modeling of Nonacoustic Combustion Instability in Simulations of Hybrid Motor Tests," NASA, Alabama, 2000.
- [48] M. A. Karabeyouglu, S. De Zilwa, B. Cantwell and G. Zilliac, "Modeling of Hybrid Rocket Low Frequency Instabilities," *Journal of Propulsion and Power*, vol. 21, no. 6, pp. 1107-1116, 2005.
- [49] B. Greiner and R. A. Frederick, "Experimental Investigation of Labscale Hybrid Instability," in *30th Joint Propulsion Conference and Exhibit*, Indianapolis, 1994.
- [50] T. Knowles, D. Kearney and R. Roberts, "Overview of 10 Inch Diameter HTPB Hybrid Motor Testing with Liquid Oxygen at Stennis Space Center," in *41st AIAA/ASME/SAE/ASEE Joint Propulsion Conference & Exhibit*, Tucson, 2005.
- [51] M. A. Karabeyouglu, J. Stevens and C. B., "Investigation of Feed System Coupled Low Frequency Combustion Instabilities in Hybrid Rockets," in *43th Joint Propulsion Conference and Exhibit*, Cincinnati, 2007.
- [52] K. C. Shadow and E. Gutmark, "Combustion Instability Related to Vortex Shedding in Dump Combustors and their Passive Control," *Progress in Energy and Combustion Science*, vol. 18, no. 2, pp. 117-132, 1992.
- [53] K. Matveev and F. Culick, "A model for Combustion Instability Involving Vortex Shedding," *Combustion Science and Technology*, vol. 175, no. 6, pp. 1059-1083, 2003.
- [54] D. Pastrone, L. Casalino and C. Carmicino, "Analysis of Acoustics and Vortex Shedding Interactions in Hybrid Rocket Motors," *Journal of Propulsion and Power*, vol. 30, no. 6, pp. 1613-1619, 2014.
- [55] C. Carmicino, "Acoustics, Vortex Shedding, and Low-Frequency Dynamics Interaction in an Unstable Hybrid Rocket," *Journal of Propulsion and Power*, vol. 25, no. 6, p. 1322-1335, 2009.

- [56] J. Lee, A. E. De Morais Bertoldi, A. Andrianov, R. A. Borges, C. A. G. Veras, S. Battistini, M. T. and P. Hendrick, “Role of Precombustion Chamber Design in Feed-System Coupled Instabilities of Hybrid Rockets,” *Journal of Propulsion and Power*, vol. 36, no. 6, p. 796–805, 2020.
- [57] C. Carmicino and G. D. Di Martino, “Analytical modeling of the one-dimensional acoustic field in hybrid rocket combustion chamber,” *Journal of Sound and Vibration*, vol. 437, no. 22, pp. 180-197, 2018.
- [58] D. Pastrone, L. Casalino, M. R. Sentinella and C. Carmicino, “Acoustic Analysis of Hybrid Rocket Combustion Chambers,” *Journal of Propulsion and Power*, vol. 26, no. 3, pp. 415-420, 2010.
- [59] C. Carmicino and D. Pastrone, “An Analytical Model to Predict Longitudinal Acoustic Modes Frequency of Hybrid Rockets Combustion Chamber,” in *53rd AIAA/SAE/ASEE Joint Propulsion Conference*, Atlanta, 2017.
- [60] S. De Zilwa, M. A. Karabeyoglu and G. Zilliac, “Combustion Oscillations in High Regression Rate Hybrid Rockets,” in *30th Joint Propulsion Conference and Exhibit*, Indianapolis, 2003.
- [61] A. Chandler, E. Jens, B. J. Cantwell and G. S. Hubbard, “Visualization of the Liquid Layer Combustion of Paraffin Fuel for Hybrid Rocket Applications,” in *48th AIAA/ASME/SAE/ASEE Joint Propulsion Conference & Exhibit*, Atlanta, 2012.
- [62] E. T. Jens, A. C. Karp, V. A. Miller, H. G. S. and B. J. Cantwell, “Experimental Visualization of Hybrid Combustion: Results at Elevated Pressures,” *Journal of Propulsion and Power*, vol. 36, no. 1, pp. 1-14, 2020.
- [63] A. Petrarolo and M. Kobald, “Evaluation Techniques for Optical Analysis of Hybrid Rocket Propulsion,” *Journal of Fluid Science and Technology*, vol. 11, no. 4, pp. 1-20, 2016.
- [64] G. Di Martino, G. Gallo, S. Mungiguerra, C. Carmicino, R. Savino, D. Cardillo and F. Battista, “Recent Advancements in Experimental and

- Numerical Characterization of Paraffin-based Fuels for Hybrid Rocket Application,” in *AIAA Propulsion and Energy 2019*, Indianapolis, 2019.
- [65] C. Carmicino, G. Gallo and R. Savino, “Self-consistent surface-temperature boundary condition for liquefying-fuel-based hybrid rockets internal-ballistics simulation,” *International Journal of Heat and Mass Transfer*, vol. 169, p. 120928, 2021.
- [66] G. Gallo, S. Mungiguerra and R. Savino, “New Entrainment Model for Modelling the Regression Rate in Hybrid Rocket Engines,” *Journal of Propulsion and Power*, 2021, Articles in Advance.
- [67] G. Gallo, C. Carmicino, S. Mungiguerra, G. D. Di Martino and R. Savino, “An Improvement of the Gas-surface Interaction and Entrainment Models for Paraffin-based Fuels in Hybrid Rocket Engines,” in *AIAA Propulsion and Energy 2020 Forum*, VIRTUAL EVENT, 2020.
- [68] C. Carmicino, F. Scaramuzzino and A. Russo Sorge, “Trade-off between paraffin-based and aluminium-loaded HTPB fuels to improve performance of hybrid rocket fed with N₂O,” *Aerospace Science and Technology*, vol. 37, pp. 81-92, August 2014.
- [69] A. Russo Sorge, C. Carmicino and A. Nocito, “Design of a lab-scale cooled two-dimensional plug nozzle for experimental tests,” in *38th AIAA/ASME/SAE/ASEE Joint Propulsion Conference & Exhibit*, Indianapolis, Indiana, 2002.
- [70] G. Gallo, G. D. Di Martino, G. Festa and R. Savino, “Experimental Investigation of N₂O Decomposition with Pd/Al₂O₃ Cylindrical Pellets Catalyst,” *Journal of Spacecraft and Rockets*, vol. 57, no. 3, pp. 1-8, 2020.
- [71] G. D. Di Martino, G. Gallo, S. Mungiguerra, G. Festa and R. Savino, “Design and testing of a monopropellant thruster based on N₂O decomposition in Pd/Al₂O₃ pellets catalytic bed,” *Acta Astronautica*, vol. 180, no. 4, pp. 460-469, 2020.
- [72] R. Savino, G. Festa, A. Cecere, L. Pienti and D. Sciti, “Experimental set up for characterization of carbide-based materials in propulsion

- environment,” *Journal of the European Ceramic Society*, vol. 35, no. 6, pp. 1715-1723, 2015.
- [73] L. Galfetti, F. Nasuti, D. Pastrone and A. Russo, “An Italian network to improve hybrid rocket performance: strategy and results,” *Acta Astronautica*, vol. 96, pp. 246-260, March-April 2014.
- [74] G. Di Martino, S. Mungiguerra, C. Carmicino, R. Savino, D. Cardillo, F. Battista, M. Invigorito and G. Elia, “200-N laboratory scale hybrid rocket testing for paraffin fuel performance characterization,” *Journal of Propulsion and Power*, 2018.
- [75] G. N. Abramovich, “General Properties of Turbulent Jets,” in *The Theory of Turbulent Jets*, Cambridge, MIT Press., 1963, pp. 3-46.
- [76] M. V. Herbert, D. L. Martlew and R. A. Pinker, “The Design-Point Performance of Model Internal-Expansion Propelling Nozzles with Area Ratios up to 4,” Ministry of Technology, Aeronautical Research Reports and Memoranda , London, 1963.
- [77] S. Gordon and B. McBride, “Computer program of complex chemical equilibrium compositions and applications,” Nasa Reference Publication 1311, 1994.
- [78] J. Messineo, K. Kitagawa, C. Carmicino and T. Shimada, “Reconstructed Ballistic Data Versus Wax Regression Rate Intrusive Measurement in a Hybrid Rocket,” *Journal of Spacecraft and Rockets*, vol. 56, no. 6, pp. 1295-1308, 2020.
- [79] H. Nagata, H. Nakayama, M. Watanabe, M. Wakita and T. Totani, “Accuracy and Applicable Range of a Reconstruction Technique for Hybrid Rockets,” *Advances in Aircraft and Spacecraft Science*, vol. 1, no. 3, pp. 273-289, 2014.
- [80] Y. Saito, L. Kamps, K. Komizu, D. Bianchi, F. Nasuti and H. Nagata, “The Accuracy of Reconstruction Techniques for Determining Hybrid Rocket Fuel Regression Rate,” in *In Proceedings of 2018 Joint Propulsion Conference*, Cincinnati, 2018.

- [81] J. J. Marano and G. D. Holder, "General Equation for Correlating the Thermophysical Properties of n-Paraffins, n-Olefins, and Other Homologous Series. 2. Asymptotic Behavior Correlations for PVT Properties," *Industrial & Engineering Chemistry Research*, vol. 36, no. 5, pp. 1895-1907, 1995.
- [82] A. Chorin, "Numerical solution of the Navier-Stokes equations," *Mathematics of Computation*, vol. 22, no. 104, pp. 745-762, 1968.
- [83] T. Cebeci, *Analysis of Turbulent Flows*, Kidlington, Oxfordshire: Elsevier Ltd, 2004.
- [84] F. Menter, "Two-equation Eddy-viscosity turbulence models for engineering applications," *AIAA Journal*, vol. 32, no. 8, pp. 1598-1605, 1994.
- [85] D. Wilcox, "Turbulence Energy Equation Models," in *Turbulence Modeling for CFD*, La Canada, California, DCW Industries, 1998, pp. 73-170.
- [86] C. Wooldridge, G. Marxman and R. Kier, "Investigation of combustion instability in hybrid rockets," NASA contract NAS 1-7310, 1969.
- [87] Y. Sivathanu and G. Faeth, "Generalized state relationship for scalar properties in non-premixed hydrocarbon/air flames," *Combustion and Flame*, vol. 82, no. 2, pp. 211-230, 1990.
- [88] W. Jones and J. Whitelaw, "Calculation methods for reacting turbulent flows: a review," *Combustion and Flame*, vol. 48, pp. 1-26, 1982.
- [89] M. Hazewinkel, "Beta-distribution," in *Encyclopedia of Mathematics*, Springer, 2001.
- [90] P. Roache, *Verification and validation in computational science and engineering*, Albuquerque, New Mexico: Hermosa Publishers, 1998.
- [91] D. Bianchi, F. Nasuti and D. and Delfini, "Modeling of Gas-Surface Interface for Paraffin-Based Hybrid Rocket Fuels in Computational Fluid Dynamics Simulations," *Progress in Propulsion Physics*, vol. 11, pp. 3-24, 2019.

- [92] J. Staggs, "A Theoretical Investigation into Modelling Thermal Degradation of Solids Incorporating Finite-Rate Kinetics," *Combustion Science and Technology*, vol. 123, pp. 261-285, 1997.
- [93] J. J. Marano and G. Holder, "A General Equation for Correlating the Thermophysical Properties of n-Paraffins, n-Olefins, and Other Homologous Series. 3. Asymptotic Behavior Correlations for Thermal and Transport Properties," *Industrial & Engineering Chemistry Research*, vol. 36, no. 6, pp. 2399-2408, 97.
- [94] A. Karabeyoglu, B. Cantwell and J. Stevens, "Evaluation of homologous series of normal-alkanes as hybrid rocket fuels," in *41st AIAA/ASME/SAE/ASEE Joint Propulsion Conference & Exhibit*, Tucson, Arizona, 2005.
- [95] P. Sawant, M. Ishii and M. Mori, "Droplet Entrainment Correlation in Vertical Upward Co-current Annular Two-phase Flow," *Nuclear Engineering and Design*, vol. 232, no. 6, p. 1342–1352, 2008.
- [96] P. Sawant, M. Ishii and M. Mori, "Prediction of Amount of Entrained Droplets in Vertical Annular Two-phase Flow," *International Journal of Heat and Fluid Flow*, vol. 30, p. 715–728, 2009.
- [97] A. Al Sarkhi, C. Sarica and B. Qureshi, "Modeling of Droplet Entrainment in Co-current Annular Two-phase Flow: A New Approach," *International Journal of Multiphase Flow*, vol. 39, pp. 21-28, 2012.
- [98] J. R. Thome and A. Cioncolini, "Fundamentals and Methods," in *Encyclopedia of Two-Phase Heat Transfer and Flow*, 2015.
- [99] M. Karabeyogly, B. Cantwell and G. Zilliac, "Development of scalable space-time averaged regression rate expressions for hybrid rockets," *Journal of Propulsion and Power*, vol. 23, no. 4, pp. 737-747, 2007.
- [100] G. Abramovich, *The Theory of Turbulent Jets*, Cambridge, MA: Massachusetts Inst. of Technology Press, 1963.
- [101] T. Poinot and D. Veynante, *Theoretical and Numerical Combustion*, R. T. Edwards Inc, 2005.

- [102] C. Carmicino and D. Pastrone, “Novel Comprehensive Technique for Hybrid Rocket Experimental Ballistic Data Reconstruction,” *Journal of Propulsion and Power*, vol. 34, no. 1, p. 133–145, 2018.
- [103] M. Zucrow and J. Hoffman, *Gas Dynamics*, New York: John Wiley and Sons, 1977.
- [104] H. Oertel, *Prandtl's Essentials of Fluid Mechanics*, New York: Springer, 2004.
- [105] E. M. Greitzer, C. S. Tan and M. B. Graf, *Internal Flow - Concepts and Applications*, Cambridge: Cambridge University Press, 2004.
- [106] G. Lengellé, “Solid-Fuel Pyrolysis Phenomena and Regression Rate, Part 1: Mechanisms,” in *Fundamentals of hybrid rocket combustion and propulsion*, vol. 218, K. Kuo and M. Chiaverini, Eds., Progress in Astronautics and Aeronautics, AIAA, 2007, pp. 127-163.